2006

Multispectral iris recognition analysis: Techniques and evaluation

Christopher K. Boyce
West Virginia University

Multispectral Iris Recognition Analysis: Techniques and Evaluation

by

Christopher K. Boyce

Thesis submitted to the
College of Engineering and Mineral Resources
at West Virginia University
in partial fulfillment of the requirements
for the degree of

Master of Science
in
Electrical Engineering

Lawrence Hornak, Ph.D., Chair
Arun A. Ross, Ph.D., Co-chair
Xin Li, Ph.D.

Lane Department of Computer Science and Electrical Engineering

Morgantown, West Virginia
2006

Keywords: Iris, Iris Recognition, Multispectral, Iris Segmentation, Spoofing, Iris Anatomy, Iris Feature Extraction

Abstract

Multispectral Iris Recognition Analysis: Techniques and Evaluation

by

Christopher K. Boyce
Master of Science in Electrical Engineering

West Virginia University

Lawrence Hornak, Ph.D., Chair
Arun Ross, Ph.D. (Co-chair)

This thesis explores the benefits of using multispectral iris information acquired using a narrow-band multispectral imaging system. Commercial iris recognition systems typically sense the iridal reflection pertaining to the near-infrared (IR) range of the electromagnetic spectrum. While near-infrared imaging does give a very reasonable image of the iris texture, it only exploits a narrow band of spectral information. By incorporating other wavelength ranges (infrared, red, green, blue) in iris recognition systems, the reflectance and absorbance properties of the iris tissue can be exploited to enhance recognition performance. Furthermore, the impact of eye color on iris matching performance can be determined. In this work, a multispectral iris image acquisition system was assembled in order to procure data from human subjects. Multispectral images pertaining to 70 different eyes (35 subjects) were acquired using this setup. Three different iris localization algorithms were developed in order to isolate the iris information from the acquired images. While the first technique relied on the evidence presented by a single spectral channel (viz., near-infrared), the other two techniques exploited the information represented in multiple channels. Experimental results confirm the benefits of utilizing multiple channel information for iris segmentation. Next, an image enhancement technique using the CIE L*a*b* histogram equalization method was designed to improve the quality of the multispectral images. Further, a novel encoding method based on normalized pixel intensities was developed to represent the segmented iris images. The proposed encoding algorithm, when used in conjunction with the traditional texture-based scheme, was observed to result in very good matching performance. The work also explored the matching interoperability of iris images across multiple channels. This thesis clearly asserts the benefits of multispectral iris processing, and provides a foundation for further research in this topic.

Acknowledgments

I must express my gratitude to all the individuals who helped make my education a success. Without their support I would not have come so far.

I appreciate the opportunity provide to me to have two great mentors and guides through my graduate studies. I am very grateful for the guidance provided to me by my committee chairs Dr. Ross and Dr. Hornak. It has been an honor to have two outstanding advisors. Without their guidance and motivation I would have not reached this phase of my life. Dr. Ross has shown me that with determination and hard work anything is achievable. While Dr. Hornak gave me the encouragement I needed to pursue my graduate studies.

I am also very grateful to Dr. Xin Li, my committee member, for his guidance, useful suggestions and classes that I have learned so much from. I would also like to take the opportunity to thank all my lab mates through the years: Rajiv, Phani, Nikhil, Rohan, Rohin, Simona, Mat, Shigefumi, Sujan, Kiran, Sarvesh, Samir, and Jidnya. Without your help and friendship I would have never made it through my studies.

Lastly I would like to thank my family for their love and support. I would like to especially thank my loving wife Nicole. She stood by me through the endless nights of work. She is my crutch in life. Without her support I would have not come this far.

Contents

List of Figures

List of Tables

Chapter 1

Introduction

1.1 Biometrics

Biometrics is the science and technology of measuring and statistically analyzing biological data [1, 2]. Biometrics pertains to the use of automated methods for uniquely recognizing humans based upon one or more intrinsic biological or behavioral traits. Any human physiological or behavioral characteristic could be a biometric provided it has the following desirable properties: universality, uniqueness, permanence, and collectability [3]. Physical biological biometrics are the most widely used biometric traits and include unique physical traits of the human body such as fingerprint, iris, face, hand geometry, palm print, retina, vein structure, etc. Behavioral biometrics include characteristics such as signature, keystroke dynamics, gait, etc. A biometric system is an application that is used to authenticate, identify or verify, an individual's identity based on processing the individual's unique biometric trait. The system uses biometric identifiers to establish the identity of an individual based on pattern recognition techniques [4]. Biometric applications are intended to determine identity based on "who you are" (fingerprint or iris pattern) rather than "what you possess or know" (ID card or password). This thesis focuses on the iris as the biometric identifier to authenticate an individual.

1.2 Iris Recognition

The human eye is the only internal organ of the human body that is visible to the outside, being located behind the transparent cornea, and is therefore easily imaged. The iris has a

vastly detailed texture that is postulated to be stable throughout an individual's life span [5]. Its epigenetic formation, being independent of the genetic genotype, depends mainly on the initial embryonic conditions. The iris' detailed morphogenesis depends on initial conditions in the embryonic mesoderm from which it develops [6]. Thus, the iris texture is chaotic and unique to every individual. Due to its chaotic nature and contactless acquisition, the iris is considered to be one of the most accurate and reliable biometric traits for the purpose of verification and identification of individuals ([7, 8, 9, 10, 11, 12, 13, 14, 15, 16, 17, 18, 19]). Commercial iris recognition systems operate predominately in the near-infrared (IR) range of the electromagnetic spectrum. Figure 1.1 shows the optical spectrums of some commercially available infrared iris recognition systems. Each system's spectrum was traced on an Advantest optical spectrum analyzer. The spectrums indicate that current systems are using wavelengths that peak around 850nm (Panasonic and Oki), with a narrow band pass. However, some system traverse into the range of 750nm (LG) and use multiple wavelength illumination to image the iris. The infrared light is invisible to the human eye and the intricate textural pattern represented in different colored irides is revealed under the near-IR range illumination. The texture of the iris in the IR illumination has been traditionally used as a biometric indicator [6].

Authentication in commercial systems is comprised of taking a digital photograph of the iris in IR illumination and extracting an iris feature set summarizing the textural content of the iris. In order to perform feature matching the iris feature set must first be extracted and enrolled into a database. The enrolled feature set is known as a template. During authentication, the extracted feature set is then matched with the templates in the database in order to determine or validate an individual's identity.

The iris recognition algorithm can be divided into functions of acquisition, extraction, representation and comparison of the patterns present on the surface of the iris as seen in Figure 1.2. The processing system can further be broken down into modules for iris segmentation, normalization (unwrapping), enhancement (in some cases), feature extraction (encoding) and feature matching.

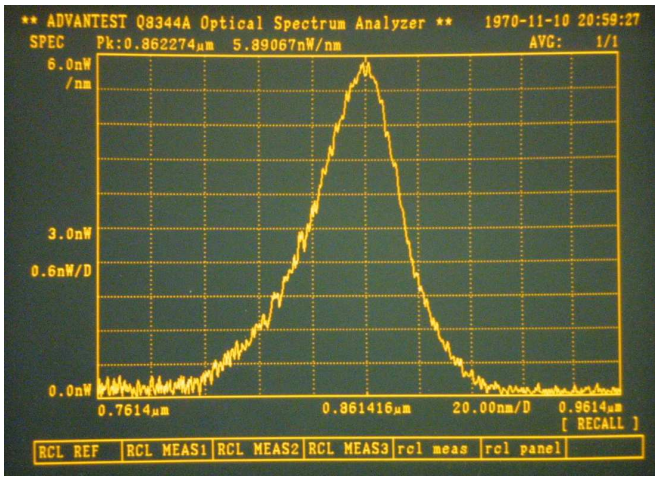

Panasonic Authenticam

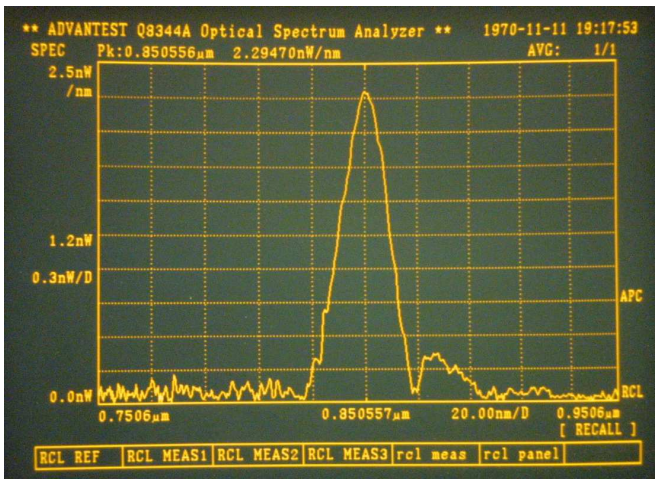

Oki Irispass

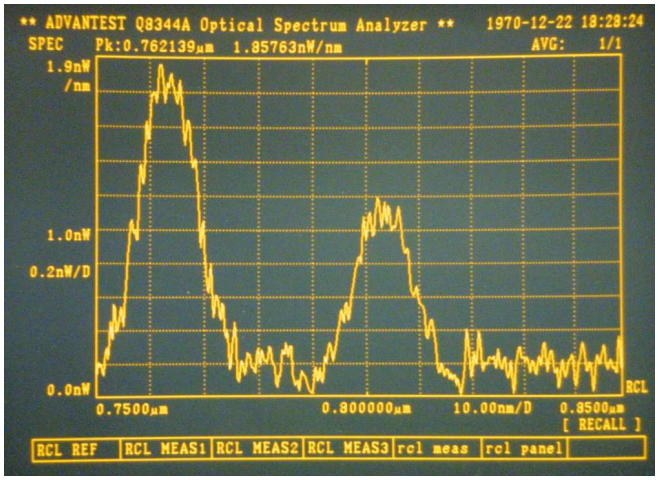

LG IrisAccess

Figure 1.1: Optical spectrum of commercial iris recognition systems.

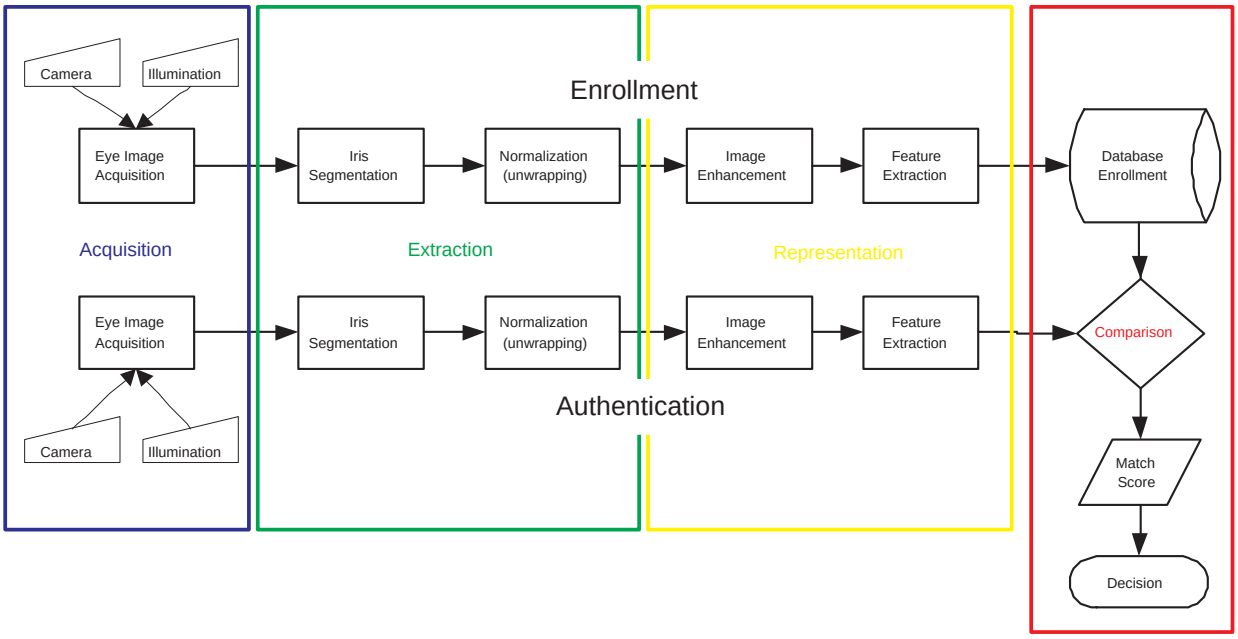

Figure 1.2: Flowchart depicting the various stages of an iris recognition system.

1.3 Iris Anatomy and Physiology

To better appreciate the significance of multispectral iris analysis the textural intricacies of the iris anatomy must be identified in detail. The purpose of this section is to emphasize individual iris components that may exhibit different reflectance characteristics thereby justifying a multispectral analysis.

1.3.1 Iris

The iris is the most anterior portion of the eye behind the cornea being placed in the eye's frontal plane [20]. It is a thin, contractile, pigmented diaphragm, which is perforated near its center by a circular aperture, usually slightly off centered, called the pupil. The iris attaches to the ciliary body at the ciliary margin or iris root and surrounding the pupil is the pupillary margin of the iris. The average diameter of the iris is approximately 12mm, with an average thickness of about .5mm, that is thickest at the collarette and thinning radially away from the pupil. The low truncated cone shape of the iris is formed from the anterior surface of the lens pressing lightly against the posterior iris causing it to bulge.

Looking at a cross sectional view of the iris, it divides the space between the cornea and the

lens into two chambers, anterior and posterior, and is bathed in aqueous humor on both sides. Aqueous humor (a clear water fluid), flowing mainly through the pupil and portions of the iris, circulates between these two chambers.

The iris' main function is to regulate the amount of light entering the eye and impinging on the retina. It does this through dilation and constriction of the pupil. In low light conditions, the dilator pupillae muscle is triggered through parasympathetic nerve activity and dilates the iris to allow in more light. The dilation process is also termed as mydriasis. In bright or intensive light conditions, the constrictor pupillae muscle is triggered through parasympathetic nerve activity which constricts the pupil. The constriction process is termed as miosis. The actual contribution of the iris to the control of light is marginal. The retina is only sensitive to six log units of light, whereas the iris only represents a ten-fold change in the amount of light (1 log unit).

1.3.2 Anterior Iris Structures

The anterior portion of the iris is the foremost visible portion of the eye. Therefore, it is

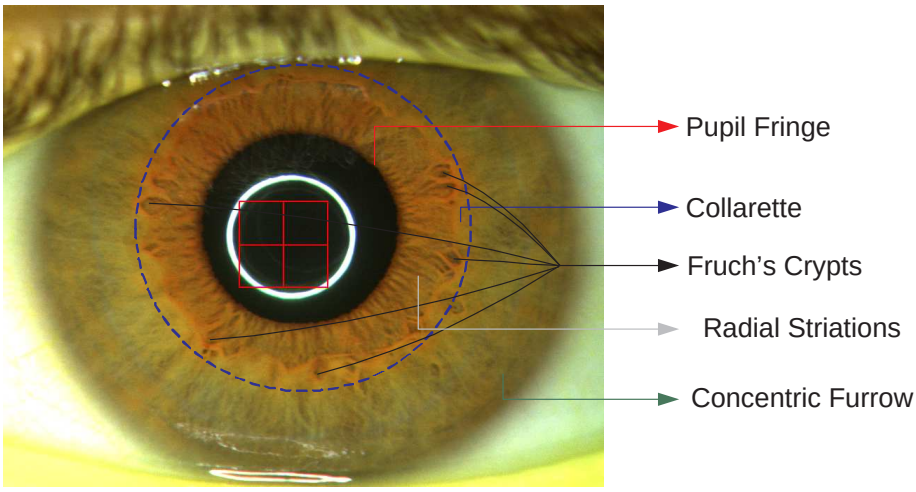

Figure 1.3: Anterior anatomy of a light brown colored iris. The white ring located in the pupil is the iris light illumination reflection from the moist cornea.

easily imaged and is the focus of most iris recognition systems. The anterior surface of the iris is separated into two zones: the pupillary zone and the ciliary zone. These two zones are separate by a circular zigzag ridgeline that is the thickest part of the iris known as the collarette, which is not well defined in irides with chaotic iris structure. The collarette is typically around 2mm from the pupillary margin (dependent on the individual) and the region lying closest to the pupil

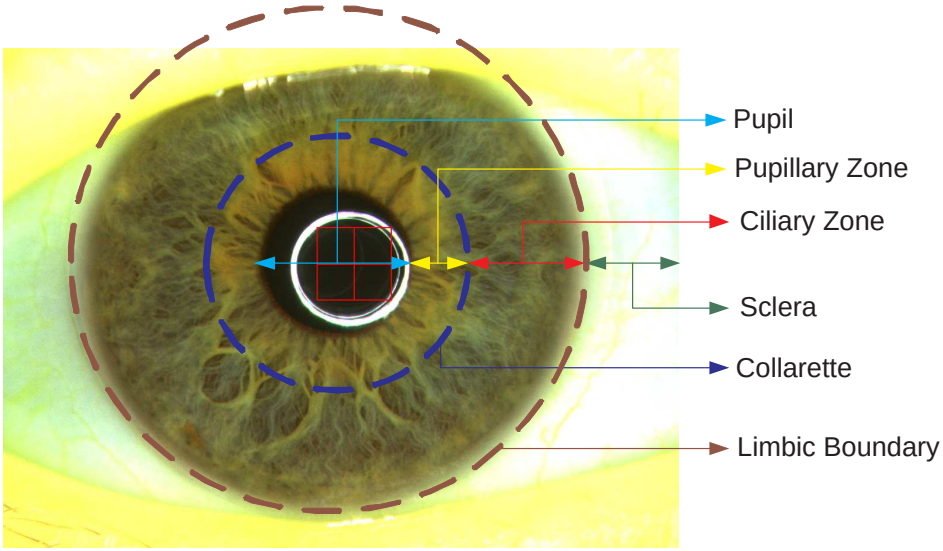

Figure 1.4: Sectional anterior anatomy traversing radially across a green/hazil colored iris.

is the pupillary zone. The area on the radial outer portion of the iris beyond the collarette and inside of the sclera is the ciliary zone. The two regions of the surface of the iris often differ in color, and many pit like oval structures appear mainly in the zone around the collarette and the outer edge of the iris. These structures are called crypts (Fruch's crypts) and they permit fluids to quickly enter and exit the iris during dilation and contraction of the pupil.

The anterior surface has a velvety appearance showing a series of radial streaks that are caused by trabeculae or bands of connective tissue that enclose the crypts. These radial steaks straighten when the pupil is constricted and turn wavy when the pupil is dilated. Near the outer part of the ciliary zone concentric lines can be seen. These lines become deeper as the pupil dilates and are called contraction furrows. These lines, caused by the folding of the iris as the pupil dilates, are similar to the folds in the hand and are easily seen in dark pigmented irises while almost invisible in the structure of lighter colored irides. At the pupillary margin, the heavily pigmented epithelium extends around the edge of the pupil. The radial folds of the epithelium give the pupillary margin a sort of beaded or pearl appearance. This region is termed the pupillary fringe or ruff and can only be seen in high resolution images of the iris due to its small size.

1.3.3 Iris Composition

Taking a cross section of the iris it consists of two layers: the anterior stroma layer and the posterior epithelial layers.

The stroma, which makes up the anterior visible portion of the iris, is composed of highly vascular connective tissue containing collagen fibers, fibroblasts, melanocytes, nerve fiber, smooth muscle, myoepithelial cells, radial vessels, and matrix [21].

In the most anterior region of the stroma there is a compact dense arrangement of fibroblasts, melanocytes, and collagen fibers. The collagen fibers are loosely arranged with a diameter of the collagen fibrils at about 60nm, with a periodicity of 50 to 60nm. The fibroblasts have numerous branching processes that eventually blend with the trabeculae meshwork. Melanocytes also show branching processes, and the cytoplasm within them contain varying numbers of melanosomes. Other cells such as mast cells, macrophages, and lymphocytes also make up portions of the stroma.

Two muscles implement the dilation and constriction functions of the iris. These two muscles are the sphincter pupillae and the dilator pupillae. The sphincter pupillae is located in the pupillary zone and it forms a smooth ring of muscle fibers around the pupil. The smooth muscle cell bundles are separated by connective tissue that contains blood vessels and sensory nerves. The dilator pupillae muscle is a thin layer of myoepithelium that extends from the iris root radially inward to the sphincter pupillae. The posterior layer of the iris is composed of two pigmented epithelial layers, anterior and posterior. The anterior layer lies in contact with the stroma and is associated with the muscular process of the dilator pupillae. The layer contains relatively few melanin granules.

The posterior layer cells are larger than the anterior layer and cubical in shape. They are stacked together in a compact and orderly arrangement and are heavily composed of melanin granules giving them a darker appearance.

1.3.4 Iris Pigmentation

The iris can vary in color from light blue to dark brown [22]. This variation can be (a) across the population, (b) between the left and right eyes of an individual, or (c) in different regions of the iris in the same eye. Impinging light on the iris gives the appearance of color. The iris is a protection device for the vision process. Longer wavelength light readily penetrates the iris and is

absorbed. However, some shorter wavelengths (blue light), are reflected back and scattered by the iris stroma. This gives irides with low pigmentation a blue appearance due to the reflection and scattering. It is suspected that iris color may not remain constant throughout life [23], unlike the iris structure. Iris color can be affected by a variety of ocular disorders such as Horner's syndrome and Fuchs' heterochromic iridocyclitis that results in a decrease in iris pigmentation. However, drugs such as latanoprost, have been found to lead to an increase in iris pigmentation. The main contributors to the color are the cellular density in the extracellular matrix (vascular connective tissue containing collagen fibers, fibroblasts, melanocytes, nerve fiber, smooth muscle, myoepithelial cells, radial vessels, and matrix) of the iris stroma, the pigment contained in the iris stroma and the pigment contained in the iris pigment epithelium (IPE) layer. Studies indicate that the amount and distribution of melanin in the IPE is similar in irides of different color [24]. The IPE is also the posterior portion of the iris, being covered by the stroma. Therefore, it is less representative of the iris color than the stroma. So, the color of the iris is predominantly defined by the cellular matrix and the pigmentation of the stroma.

Pigment synthesizing cells called melanocytes produce iris color. Melanocytes store their melanin in specialized organelles called melanosomes. Melanosomes can vary in number and size, but melanocytes typically number the same across individuals. Melanosomes produce different levels of pigmentation (referred to as melanin), which is thought to be the main contributing factor in producing different colored eyes. Heavy melanin synthesis corresponds to a dark brown iris, where as light melanin synthesis corresponds to a light blue eye. The melanin can also be distributed into certain portions of the eye such as the pupillary zone and the ciliary zone giving rise to a two-toned iris. Sometimes in certain locations of the iris, freckles known as nevi (singular nevus) shown in Figure 1.5, can occur. These nevi appear as a heavily pigmented area of the iris. If the melanocytes in the iris are completely devoid of pigmentation, then the hemoglobin of the underlying blood vessels are revealed and the iris appears as a reddish color.

Melanin's main biological role is human photoprotection. Melanin is not only present in the iris of the eye but is also present in the skin, hair, the pigment layer of the retina, and other internal biological structures. There are two main types of melanin that are produced in the body, eumelanin that are black to dark brown in color, and pheomelanin that are reddish brown. The IPE contains the greatest portion of melanin. Different iris colors, blue through brown, contain comparably the same amount of eumelanin in the IPE. It has also been shown

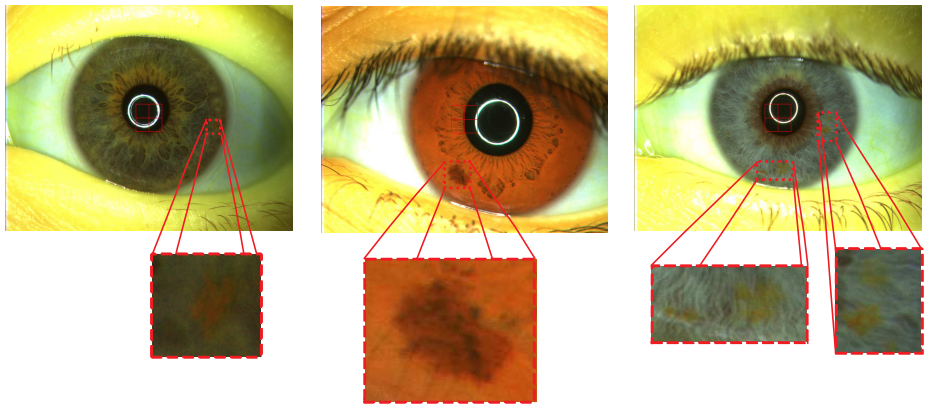

Figure 1.5: Heavily pigmented freckles (nevi) localized on different colored irides.

that varying levels of pheomelanin is more prevalent in brown irides when compared to blue [25]. However, pheomelanin makes up a very small portion of the total melanin content.

1.4 Multispectral Iris

Commercial iris recognition systems operate predominately in the near-Infrared (IR) range of the electromagnetic spectrum. Systems utilize this region because it is an invisible portion of spectrum when viewed with the sensitive human eye [26], and is thus less intrusive to the subject. Due to the biological diversity of the composition of the iris, different portions of the electromagnetic spectrum may better represent certain physical characteristics of the epigenetic iris pattern. This thesis explores the possibility of eliciting iridal information from the visible and IR ranges of the reflected light. The transmission, absorption, and reflection vary within biological iris composition classes. This thesis concentrates on the imagery of visible (400nm-700nm) and the near IR (700nm-1000nm) ranges of iridal light reflection. An assessment involving various eye colors across these ranges is performed. In particular, the role of information represented in individual spectral channels/wavelengths (i.e., IR, Red, Green, and Blue) on the matching performance of iris recognition is studied. The feasibility of decomposing the structural components of an iris based on the response of individual channels is also explored.

1.4.1 Multispectral Imaging

A multispectral image consists of multiple wavelengths or wavelength bands of the electromagnetic spectrum captured over the same object, independent of the other wavelengths. It is typically represented as a matrix of pixels for each 2-Dimensional channel (eg. Red, Green, Blue, etc.) that are concatenated or stacked on top of each other in the 3rd dimension. These multispectral images are typically a narrow band over certain wavelengths ranging around 50nm in bandpass. Some examples of multispectral remote sensors such as the Landsat Thematic Mapper and SPOT XS produce images with a few relatively broad wavelength bands [27]. Hyperspectral remote sensors, on the other hand, collect image data simultaneously in dozens or hundreds of narrow adjacent spectral bands. Both hyperspectral and multispectral imagery have been used in remote sensing applications. Multispectral imagery is used in aerial photography for military applications or to identify certain plant species, and for biometric feature analysis (e.g., face [20] [28] [29], finger [30] [31] [32]).

Through the use of multispectral imagery an iris can be broken down into its own unique reflection pattern according to its phenotypical traits. For example, the melanin content and the cellular composition in the iris determine what wavelength of light is reflected back, thus giving the appearance of a brown, blue, or green colored iris. Through the use of multispectral imagery, the peak reflection (due mostly to the melanin) and other varying reflection phenotypical iris traits can be conveyed.

1.4.2 Multispectral Image Acquisition

To capture the different wavelengths being reflected from an iris, the following arrangement using Redlake's MS3100 multispectral camera was employed. The camera incorporates three charge coupled devices (CCD) and three band-pass prisms behind the lens to simultaneously capture four different wavelength bands (Figure 1.6). The IR and red (R) sensors of the multispectral camera are two separate Sony ICX205AL sensors whose spectral response ranges from 400nm to 1000nm with a peak response at 550nm. The Green (G) and the Blue (B) channels are recorded on the same Sony RGBICX205 sensor. This sensor is a RGB sensor with a blue response from 400nm to 550nm (peaking at 460nm) and a green response from 400nm to 650nm (peaking at 550nm). Each channel is white-balanced to ensure a maximum intensity of 255 by using the white panel of a color checker chart. It must be pointed out that the resolutions of

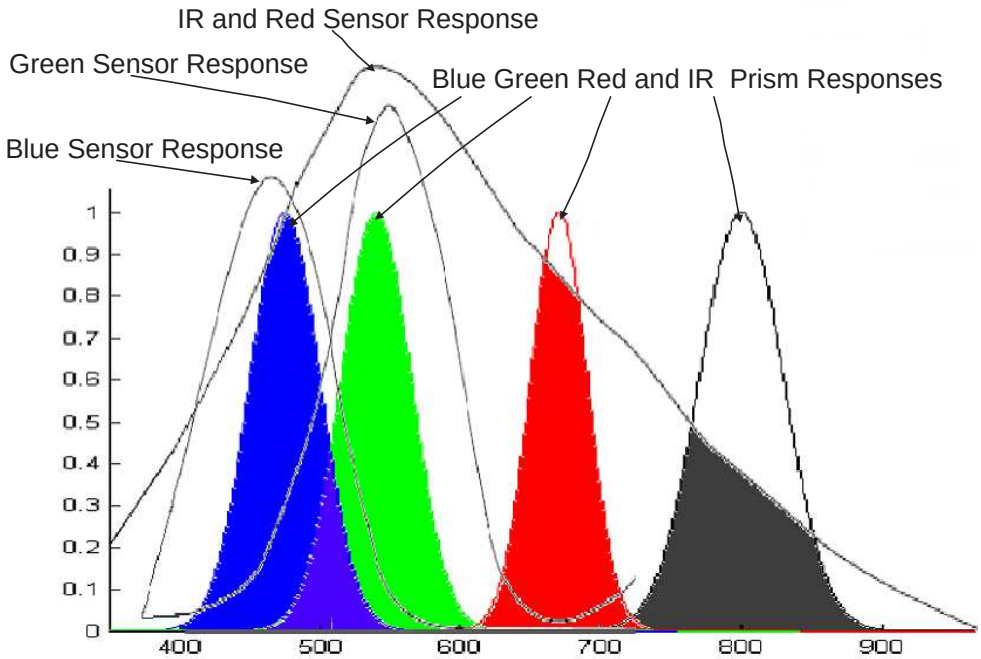

Figure 1.6: The normalized transmittance of the band-pass prisms and sensor spectral response of the acquisition device. Filled portions of the graph indicate the actual combined response of the sensors and prisms.

Channel	**Sensor**	**Image Size (pixels)**
IR	Sony ICX205AL	1040x1392
R	Sony ICX205AL	1040x1392
G	Sony RGBICX205	260x348
B	Sony RGBICX205	260x348

Table 1.1: Channel sensor type and resolution.

the images in the multiple spectral channels are not all the same. The channel, sensor type, and resolution can be seen in Table 1.1. The IR and Red sensors output an image of size 1300x1040. This represents an average of 56,000 pixels inside the segmented iris. The G and the B images are recorded on a RGB Bayer pattern sensor and are one-fourth the resolution of the other images. The G and the B images are extracted and scaled to have the same resolution as the IR and R images using linear interpolation of the nearest neighbors [33]. The primary advantage of using a camera that has three CCD sensors/prisms and a single lens is that the resulting images are all spatially registered. Therefore, no explicit image registration or alignment across multiple channels is necessary when processing the images.

This arrangement acquires spectral information as follows: (a) red light at a center wavelength of 670nm and a band pass of 40nm, (b) green with a center wavelength of 540nm and a band pass of 50nm, (c) blue with a center wavelength of 475nm and a band pass of 50nm, and (d) near-IR with a center wavelength of 800nm and a band pass of 60nm as shown in Figure 1.6.

To image the iris accurately and in a convenient fashion the multispectral camera was mounted onto an ophthalmologist's slit-lamp mount (Figure 5.1). The mount consisted of a chin rest, to position the head, and a mobile camera-mount arm that could be easily manipulated to finely focus on the iris. A broadband light source was employed to illuminate the iris of the eye. The

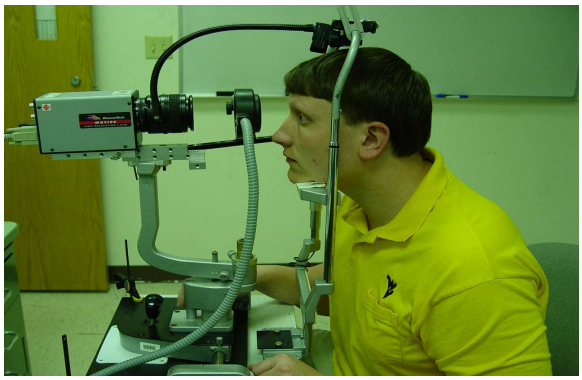

Figure 1.7: The multispectral iris image acquisition arrangement.

spectral output of the light source ranged from 350nm to 1700nm. The light source's optical power spectrum in the cameras region of detection can be seen in Figure 1.8. The illumination was projected on the eye using a fiber optic light-guide with a ring light attached at the illumination end. This projects a circular uniform illumination across the eye. However, it does produce a large ring reflection on the moist cornea of the eye, as opposed to a small point source reflection from LEDs commonly seen in most iris imaging systems.

1.4.3 Multispectral Data

The optical arrangement described in the previous section was used to acquire 70 eye images from the left and right eyes of 35 subjects (5 samples per subject). The subject pool used in this preliminary analysis consisted of individuals having different eye colors as seen in Table 1.2. The database includes irides ranging in color from greyish blue, greenish hazel, to dark brown. The '/' indicated in the color column of the table suggests that the iris has a two-toned appearance

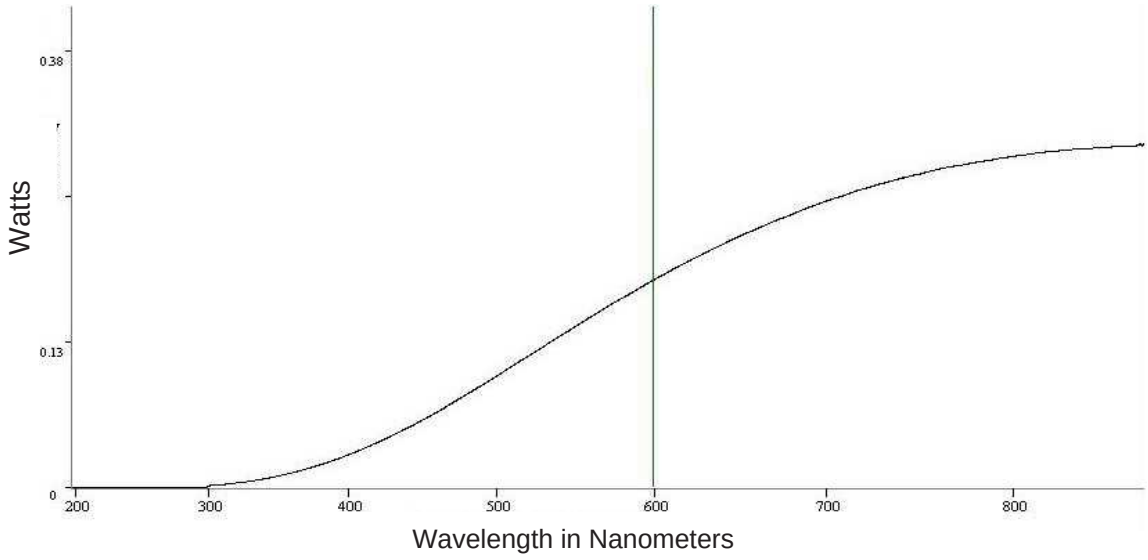

Figure 1.8: Optical power spectrum of the broadband light source.

radially. The data set also contains distinguishing features such as freckles, moles, and various colored spots and streaks. Only subjects 9, 10, 13, 17, and 35 of the set have irides with little or no melanin pigmentation and 15 out of the 35 subjects have some form of multicolored iris. Thus, the data set is very diverse with respect to the color contained in the irides.

The color of each iris was determined by visual inspection since it is difficult to automatically elicit the eye color from the images given the rapid variations in texture chromaticity within the high-resolution image. Figures 1.9, 1.10, and 1.11 show the intensity of iridal reflection across the four channels for different eye colors. Note that the CIR (color infrared) images are obtained by dropping the blue channel and including the IR channel (these are false color images). The graphical plots in these figures indicate the variation in pixel intensity across the four channels as one moves radially outward from the boundary of the pupil/iris toward the boundary of the iris/sclera.

1.5 Contributions of this thesis

The work done in this thesis addresses the use of multispectral imaging in order to capture, segment, extract features, and detect liveness of a human iris. The major contributions of this thesis are enumerated below.

User Number	**Eye Color**
Subject 1	Dark Brown
Subject 2	Dark Brown
Subject 3	Dark Brown
Subject 4	Light Brown/Green-Hazel
Subject 5	Light Brown
Subject 6	Brown/Grey-Brown
Subject 7	Light Brown
Subject 8	Dark Brown
Subject 9	Blue(Grey Streaks)
Subject 10	Blue(Grey Streaks)
Subject 11	Light Brown/Blue(Brown Spots)
Subject 12	Light Brown/Green-Hazel
Subject 13	Greenish Grey
Subject 14	Dark Brown
Subject 15	Brown
Subject 16	Dark Brown
Subject 17	Blue Grey
Subject 18	Light Brown
Subject 19	Brown/Grey(Brown Spots)
Subject 20	Light Brown
Subject 21	Brown
Subject 22	Light Brown/Grey
Subject 23	Light Brown
Subject 24	Dark Brown
Subject 25	Brown/Grey
Subject 26	Dark Brown
Subject 27	Brown
Subject 28	Light Brown/Green-Hazel
Subject 29	Brown
Subject 30	Brown
Subject 31	Light Brown
Subject 32	Yellow/Grey
Subject 33	Brown
Subject 34	Light Brown/Green
Subject 35	Blue(Grey Spots)

Table 1.2: Visual classification of iris color.

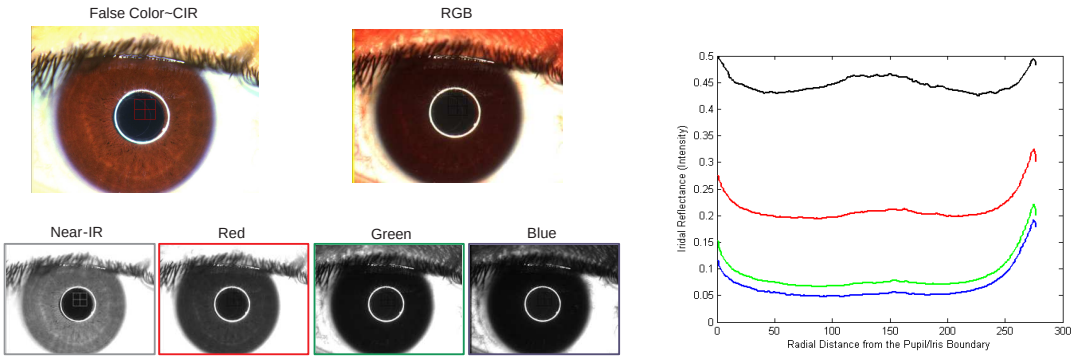

Figure 1.9: Example of a dark brown iris. The iris exhibits high iridal reflectance in the IR channel. The reflectance is observed to decrease significantly with wavelength.

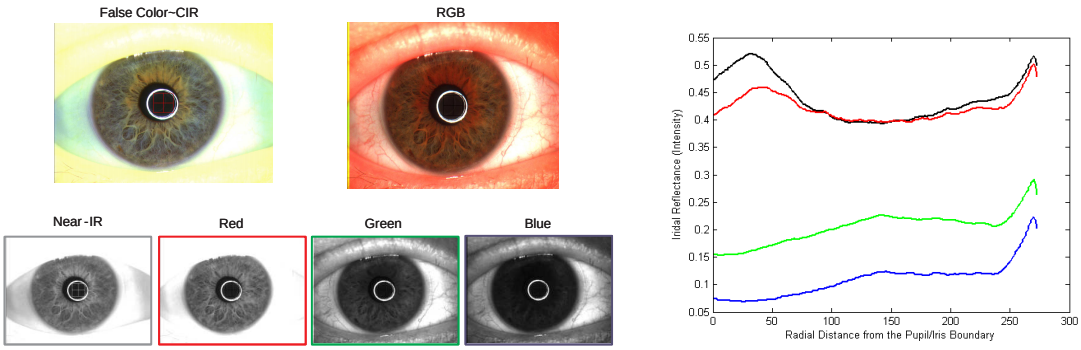

Figure 1.10: Example of a light-brown/green iris. The iris exhibits high iridal reflectance in the IR and Red channels. Reflectance decreases significantly with other wavelengths.

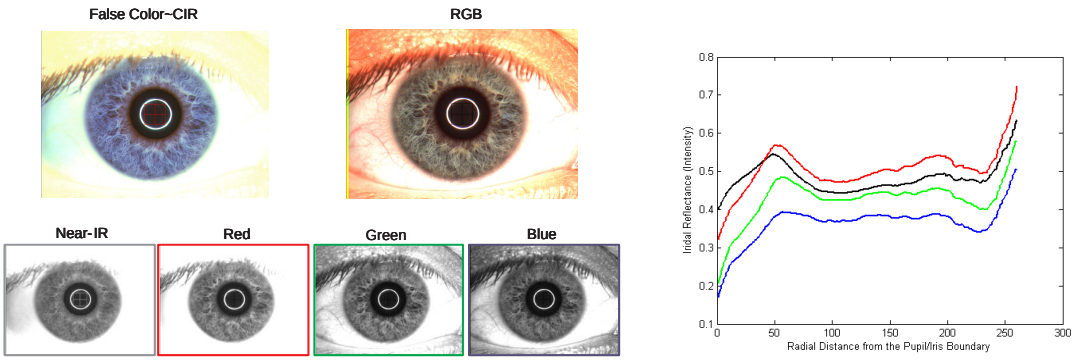

Figure 1.11: Example of a blue iris. The iridal reflection is comparable across all four channels.

1. A novel infrared and multispectral iris segmentation scheme to extract the iris structures from an image of the human eye. All commercial iris systems use only the IR channel to segment the iris. However, by eliciting the information from multiple channels, a more robust segmentation can be performed.

2. A robust encoding scheme utilizing the reflectance of the channels of a multispectral image. Most infrared recognition systems are concerned mainly with the texture of the iris. This texture elastically deforms as the iris constricts and dilates. Also, texture based methods perform poorly when the size of the image is reduced, resulting in less texture. Utilizing the intensities of concentric rings in a multispectral image, a more robust feature set can be extracted.

3. Detecting the presence of various spoof materials by incorporating anti-spoofing techniques based on the multispectral image. With the addition of multiple wavelengths (IR,R,G, and B) novel techniques can be used to determine if the eye sample being presented to the system pertains to a living individual. Spoofs attacks using photographs, video, contacts, and prosthetics are examined and countermeasures to circumvent these attacks are proposed.

The organization of the thesis is as follows. Chapter 2 explains three novel methods to perform iris segmentation. The first scheme uses only the IR component to localize and segment the iris structure. The second scheme uses the RGB vector space to perform segmentation using color. The third scheme utilizes a Bayesian classification scheme in order to do a multispectral segmentation using all four channels of an eye image. Each scheme is used in order to segment the pupillary boundary (between the pupil and iris) and the limbic boundary (between the iris and the sclera). Chapter 3 explores a new technique in which concentric rings of a multispectral iris image are extracted and used as a feature set. This extracted feature set can be used to achieve very high performance, and is robust to changes in the image image size. Chapter 4 reconnoiters techniques to spoof and the application of the multispectral information to detect liveness. Liveness detection is accomplished through the detection of pupil motion, frequency analysis, or reflection comparison of multispectral images. The final chapter 5 summarizes the contribution of this thesis and suggests possible extensions to this work.

Chapter 2

Iris Segmentation

2.1 Motivation

Iris segmentation is the first and perhaps the most important step in the iris recognition process. In the absence of proper segmentation the matching performance will inherently suffer due to inclusion of non-iris details in the encoding and matching process. Since commercial iris systems image predominantly in the near-infrared portion of the electromagnetic spectrum, the IR channel has been the focus of most segmentation algorithms. In this chapter we explore iris image segmentation techniques in the near-infrared channel that are currently used in the literature as well as techniques using dynamic thresholding to efficiently and robustly segment the iris from a single channel monochrome image of an eye. Techniques focused on exploiting multispectral information in eye images are then explored in order to achieve efficient robust iris segmentation across narrowband wavelengths. The two main segmentation steps of iris extraction are the localization of the iris's two main boundaries: the pupil/iris boundary (pupillary boundary) and the iris/sclera boundary (limbic boundary). Each segmentation technique, infrared as well as multispectral, will be described in conjunction with these two boundary detection techniques.

2.2 Iris Preprocessing

In order to efficiently and effectively segment the iris certain noisy structures need to be processed out of the iris. These include the reflections on the moist cornea. The reflections can be classified into two main categories a) *ambient* light reflections from sources such as room

lighting and b) *source* light reflections from the main source LED, bulb or fiber optic cable that illuminates the eye. Precautions are typically taken to remove the ambient light reflections using a filter. However, the source light reflection is difficult to remove from the eye image. Precautions can be taken to try and center the light inside prespecified portions of the iris (such as the pupil) in order to minimize the effect of source reflections. During our data collection, a ring light was used which projected a large reflection on the cornea as can be seen in Figure 2.1.

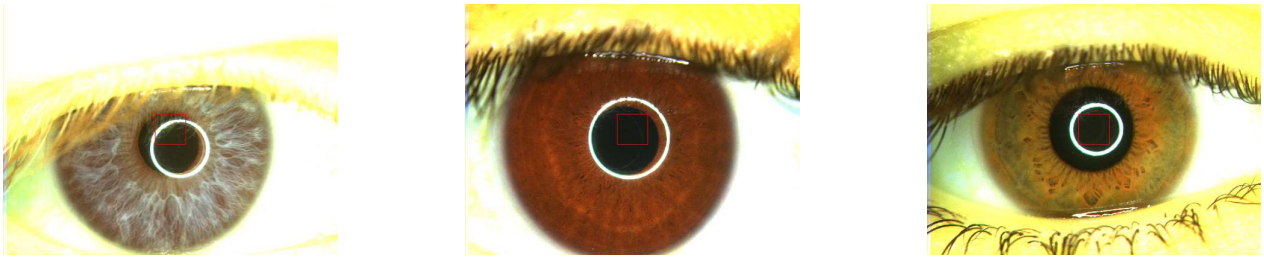

Figure 2.1: Ring light reflections a) overlapping the pupil and the iris b) infringing on the iris c) centered inside the pupil.

To overcome these challenges the ringlight was approximately positioned inside the pupil during the imaging process and the removal of the ambient light was performed by turning off all room lighting. However, to localize the reflections inside the pupil requires a very cooperative subject. Since the eye (in its orbit) and the head (attached to the neck) are both mobile the ring light is very difficult to center inside the pupil. As can be seen in some of the images in Figure 2.1, occasionally, the ring light falls into the pupillary region or the pupil of the iris. In order for accurate pupil segmentation at the pupillary boundary, the ring light needs to be removed. To facilitate this, the pupil and the iris texture are synthesized [34, 35, 36, 37] using Markov Random Fields. Let I be the iris image to be inpainted and p $\in$ I be an unknown pixel in the iris image. In order to synthesize a value to replace p, an approximation to the conditional probability distribution $P(p \mid \omega(p))$ is constructed and sampled,where $\omega(p)$ is a square image patch centered at p. A variation of the nearest neighbor technique is used and the closest match is found according to

$$\omega_{best} = argmin_{\omega} d(\omega(p), \omega) \subset I_{smp}$$

where I_{smp} is a finite sample of an image and $d(\omega(p), \omega)$ is a distance between the two image patches defined by the normalized sum of squared differences metric, d_{SSD}, convolved with a two

dimensional Gaussian kernel, G,

$$d = d_{SSD} * G$$

In order to apply the inpainting scheme, a ringlight mask indicating the areas to be inpainted must first be constructed. Since the ringlight has the highest intensity (in a 8 bit image the intensity maximum is equal to 255), each channel is thresholded with a predefined high intensity value resulting in a binary image as seen in Figure 2.2. In order to construct a single

(a) (b) (c) (d)

Figure 2.2: High intensity binary thresholding of the (a) IR, (b) R, (c) G, and (d) B channel images.

mask image that pertains only to the ring light area across all the channels, each binary image ($IR_{binary}, R_{binary}, G_{binary}, and B_{binary}$) is taken and a logical AND ($\bigcap$) operation is performed to get a composite ring light mask. The AND operation retains of all the high intensity components across the four channels as seen in Figure 2.3.

$$I = IR_{binary} \bigcap R_{binary} \bigcap G_{binary} \bigcap B_{binary}$$

The image is then morphologically closed in order to replace unseparated regions of the ring light and the object with the largest boundary is determined as shown in Figure 2.4. A circle is fit to the selected object in order to determine the center coordinates and radius of the ring light. In order to optimize the inpainting time, a rectangular region of interest (ROI) just outside of the ringlight is extracted in order to sample the ringlight containing portion of the image . A binary (OR) $\bigoplus$, operation is performed inside the ROI exclusively. This effectively detects all the ringlight and crosshairs (used to center the image) present in the image of the eye (Figure 2.5).

$$I = IR_{binary} \bigcup R_{binary} \bigcup G_{binary} \bigcup B_{binary}$$

Once the binary image indicating the ringlight (a mask) is determined, the selected region undergoes texture synthesizing in order to inpaint the ringlight. The light ring is inpainted pixel

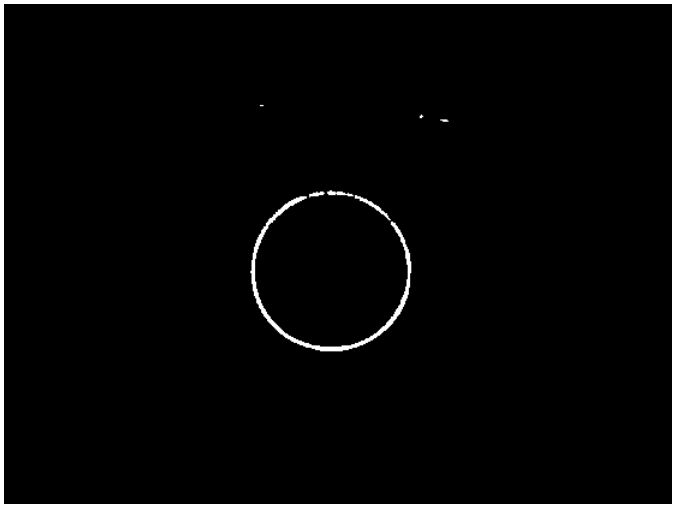

Figure 2.3: Result of the logical AND operation across the four channels.

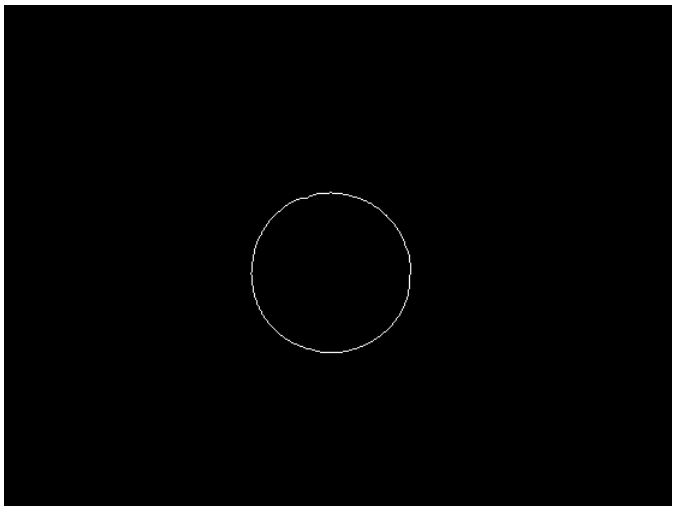

Figure 2.4: Result of the morphological closing and largest object selection.

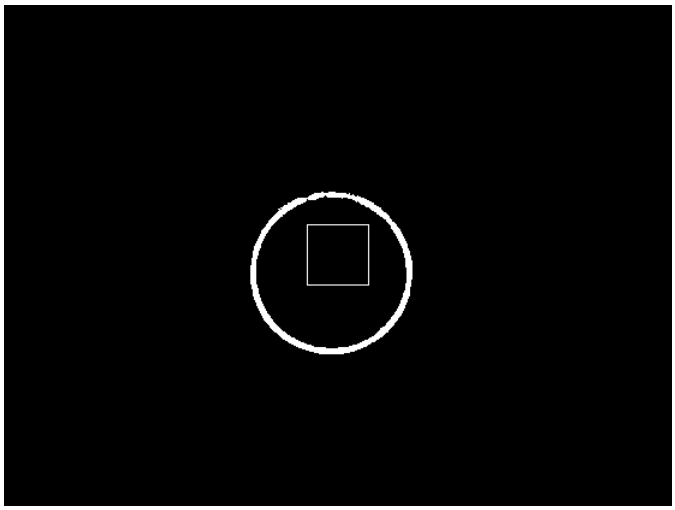

Figure 2.5: Result of the logical OR operation across the four channels in a specified ROI.

by pixel in order to capture the subtle details of the iris structure. The result of the inpainting across the four channels can be seen in Figure 2.6

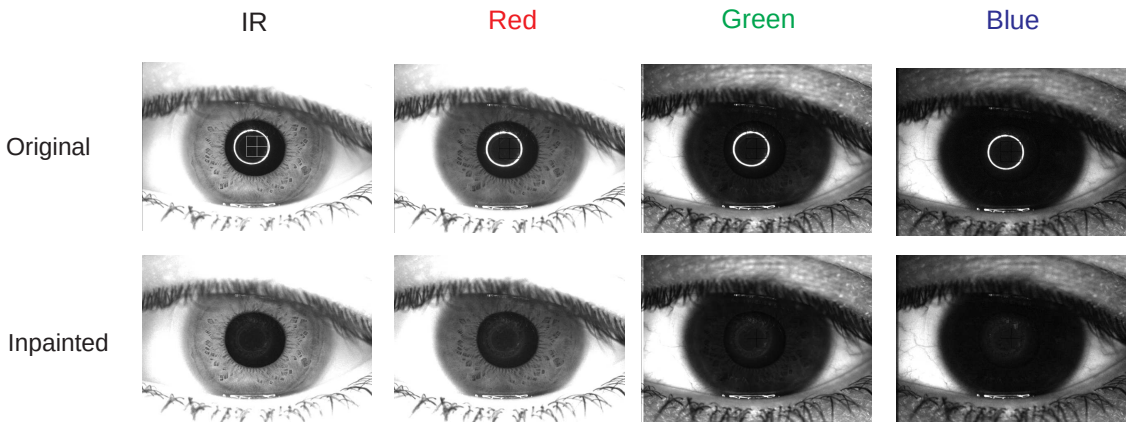

Figure 2.6: Result of the inpainting procedure.

2.3 Infrared Iris Segmentation

All commercial systems use only a single monochrome near-IR channel to image and segment the iris. So a classical baseline segmentation proposed by Daugman using the near-IR channel is

first described. Due to the felicitous of the circular geometry of the pupil and iris, the localization of the pupillary and limbic boundary of the iris in an image $I(x, y)$ can be performed by the use of Integro-differential operators that search over an image domain (x,y) [6]. Daugman's integro-differential operator is defined as

$$max_{(r,x_0,y_0)}|G_\sigma(r) * \frac{\partial}{\partial r} \oint_{r,x_0,y_0} \frac{I(x,y)}{2\pi r} ds| \tag{2.1}$$

where $G_\sigma(r)$ is the Gaussian smoothing function of scale σ and * denotes convolution. (r, x_0, y_0) denotes the radius of the pupil or iris and its corresponding center coordinates that define the path of contour integration. By varying the radius r and center (x_0, y_0) the operator acts as a circular edge detector that searches for a maximum blurred partial derivative of the image at successively finer scales of σ. A binary mask is the result of the circular operator that indicates the iris and non-iris pixels in the image. The Integro-differential operator could be applied to the individual channels (IR, R, G, B) or the channels could be fused into one monochrome image in order to detect a circular ROI. However, since the illumination source is a ringlight it often confounds the circular edge detector when trying to distinguish the boundaries of the iris, specifically in the pupil region. Also, certain channels (G and B) image more of the veins and patterns within the sclera which can also cause segmentation problems when trying to detect the limbic boundary derivative.

In this chapter we explore two techniques for segmenting the iris. First we explore a segmentation using only the IR channel of an iris image that employs a dynamic thresholding scheme that accounts for intensity variations when segmenting the iris. Then we explore a segmentation utilizing multiple channels of a multispectral iris image in order to achieve a more robust segmentation.

Pupillary Boundary Segmentation

To extract the pupil boundary from the IR channel image the minimum intensity of each channel is first estimated. A threshold is then selected at a certain pixel intensity above this minimum in order to segment the dark pupil from the rest of the image. Since the pupil is often the darkest portion of the iris image, it is detected based on the minimum pixel value (min). For example, all pixels with intensities less then a gray level value of a ceratin range min + 0-50 (somewhere between a 0 and 50 intensity level) intensity on a [0 255] intensity scale

can be first detected. Since every image has a different exposure, due to illumination variations associated with eye movement and acquisition parameters, the threshold parameter cannot be determined heuristically. However, there is a difference in the intensity change between the pupil, the eyelashes, and other dark components of the eye image (with the pupil being the lowest intensity). Figure 2.7 displays this separation in the intensities between the pupil and other dark objects (eyelashes) in the image. The minimum pixel value in the original image was

intensity = 16-255 intensity = 16-34 intensity = 40-70

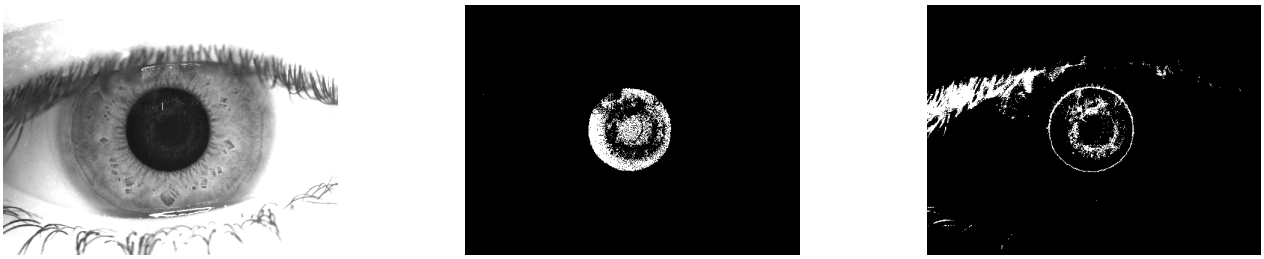

(a) Original Image (b) Pupil Thresholded Image (c) Eyelash thresholded

Figure 2.7: Binary iris images thresholded using a finite range of pixel intensities.

computed and the image was converted to binary by a heuristically determined finite threshold in the intensity ranges of (a) 16-34 and (b) 40-70. Notice that in (c) the pupillary fringe and parts of the pupil that are increased in intensity due to the ring light are being detected as the same intensities as the eyelashes. Since the inter class images in the data set do not have the same intensity, this heuristically determined finite threshold cannot be used for every subject. Thus, the threshold is set iteratively based on an expected number of pixels in the iris, depending on the size of the image and other acquisition parameters. To perform the iterative pupil thresholding (binary [0 1] conversion) the threshold value is first initialized to zero. The threshold is then set by making the pixel values of the iris image less than the minimum (min) plus the dynamic threshold (D_{thresh}) equal to 1 and the pixels greater than or equal minimum (min) plus the dynamic threshold (D_{thresh}) equal to 0 as in

$$I_{thresh}(t) = \begin{cases} 0 & min + D_{thresh}(t-1) > I_{thresh}(t-1); \\ 1 & min + D_{thresh} <= I_{thresh}(t-1); \end{cases} \tag{2.2}$$

where $I_{thresh}(t)$ is the binary image after thresholding and $I_{thresh}(t-1)$ is the binary image in the last iteration. If the sum of the white pixels (value of 1) in the logical $I_{thresh}(t)$ image is less

than the expected number the process is repeated by incrementing the dynamic threshold by an intensity of 5 until the pupil appears as the binary image as in Figure 2.8 where the expected number of pixels determined heuristically is 13000.

After thresholding, spurious features can still occur in the image. If the expected value of iris pixels is not set correctly an over segmented image of the pupil is generated as shown in Figure 2.9. If the iterative thresholding results in an over segmented image the eyelashes may be of the same intensity as the pupil. Also, if the iterative thresholding results in an under segmented binary image the ring light can create open areas in regions of the pupil. To remove these open areas in the pupil a morphological closing operation is performed (Figure 2.10). followed by a filling of all the holes. This creates a solid pupil structure. Since portions of the eyelashes may be present in the binary image, a check for connectivity is performed next. The pupil is observed to be longer than the eyelash structure in the y direction or along each column of the image, whereas the eyelashes are typically longer in the x direction or along each row of the image. So, each column of the binary image is examined to determine the maximum connectivity or diameter of the pupil in the vertical direction d_y:

$$d_y = \sum_{r=1}^{N} P_{connected}(r, c) \tag{2.3}$$

where c and r are rows and columns ,respectively, N is the total number of rows, and $P_{connected}$ is the connected pixel associated with r and c. This value is taken as an approximate diameter of the pupil and the object with this diameter is deemed to be the segmented pupil (Figure 2.11).

Limbic Boundary Segmentation

A localization of the iris in the IR channel is performed to simplify the final segmentation application of detecting the limbic boundary. The localization will effectively remove pixels that are likely to correspond to non-iris pixels, but are only an approximation to the actual iris limbic boundary. The localization is based on the coordinates of the segmented pupil. Two regions of interest (ROIs) are selected either side of the segmented pupil as seen in Figure 2.12. The ROIs are slightly below the center of the pupil and extend radially from the pupil across the iris and into the sclera on both sides of the pupil as can be seen in Figure 2.15.

The block ROIs are then decomposed into a 1-D signal ($\mathbf{X}_{block}$) by taking the mean radially

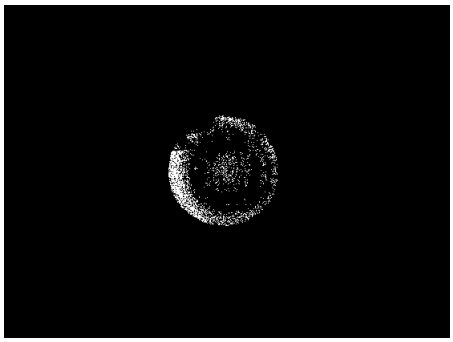

White iris pixels = 2663, $D_{thresh} = 10$.

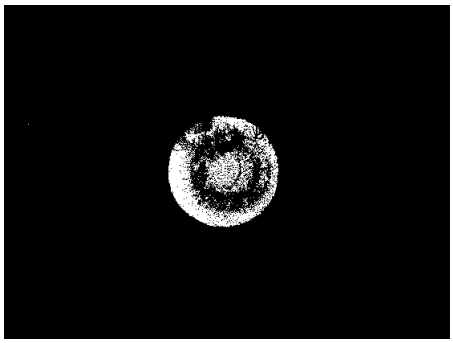

White iris pixels = 7436, $D_{thresh} = 15$.

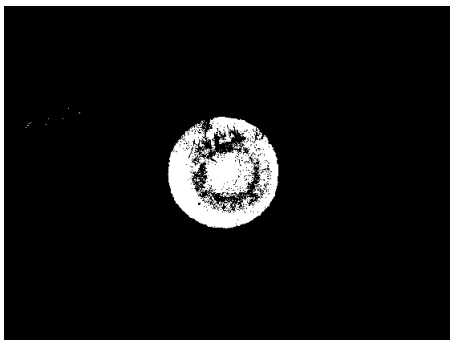

White iris pixels = 11534, $D_{thresh} = 20$.

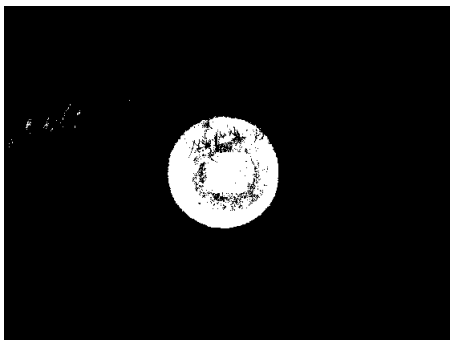

White iris pixels = 13548, $D_{thresh} = 25$.

Figure 2.8: Iterative process of thresholding the IR channels to extract the pupil.

Figure 2.9: Incorrect localization of the pupil due to improper estimation of the pupil pixels.

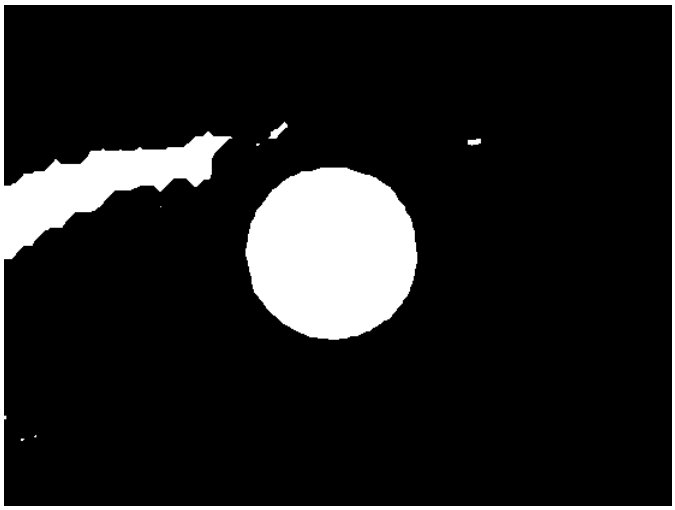

Figure 2.10: Morphological closing of the thresholded image.

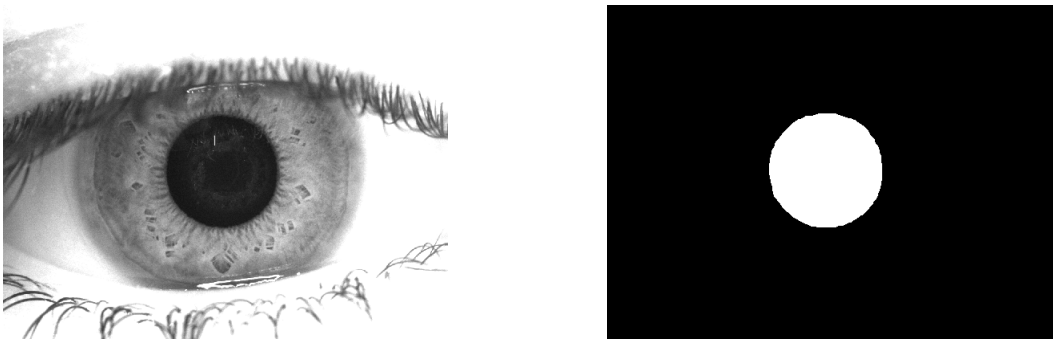

Figure 2.11: Segmented Pupil.

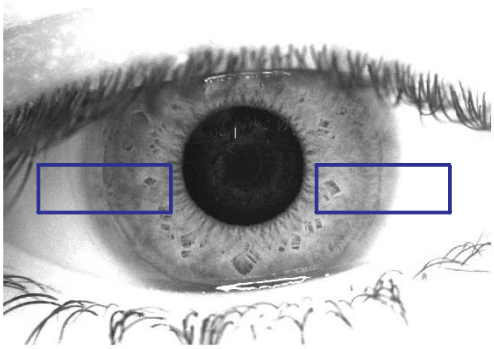

Figure 2.12: Localization of Regions of Interest (ROIs) in the iris.

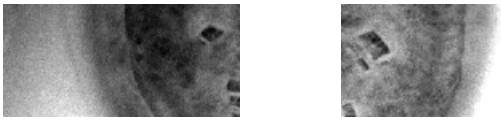

Figure 2.13: The left and right ROIs extracted from the iris image.

across the ROIs columns:

$$\mathbf{X}_{block}(c)\frac{\sum_{r=1}^{N} B_{ROI}(r,c)}{N}$$

where B_{ROI} is the extracted regions, r and c are the rows and columns of the ROI, and N is the number of pixels located in one column or equivalently the total number of rows. The decomposition figure shows the average pixel intensities of the iris and sclera and perhaps some eyelashes. Since the ROIs are arbitrary in size depending on the size of the image they first

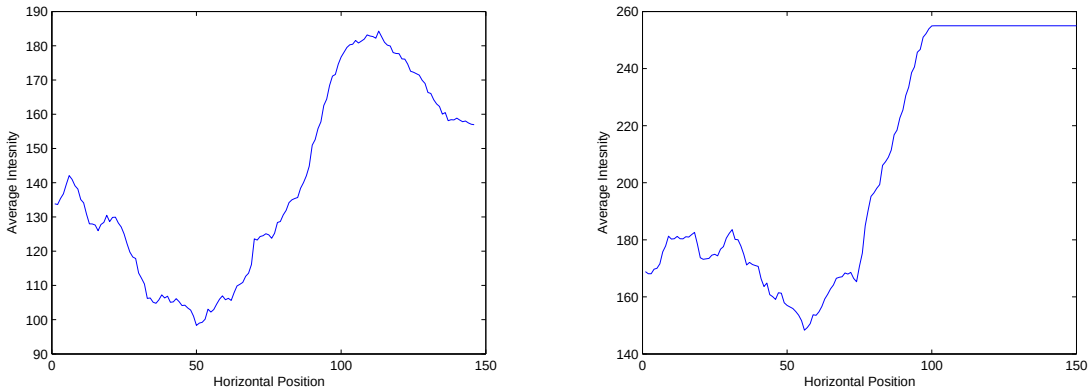

Figure 2.14: 1-D mean intensity decomposition of 2-D ROIs.

must be resized. So, the signal is padded with the last array element on the right side or end of the signal. The partial derivatives in the horizontal image axis direction are found for each

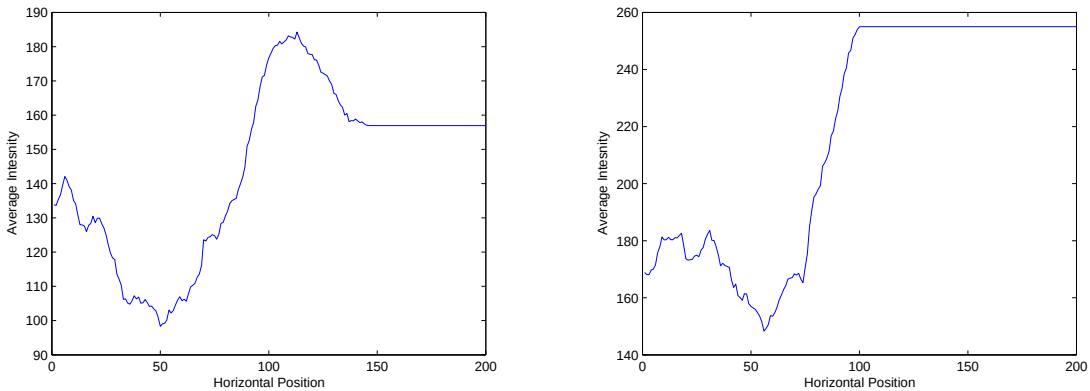

Figure 2.15: 1-D mean intensity decomposition of 2-D ROIs.

respective ROI using the finite differences $\mathbf{X}_{fd}(x_0)$ across the mean of each block.

$$\mathbf{X}_{fd}(x_0) = \mathbf{X}_{block}(x_0 + \Delta x) - \mathbf{X}_{block}(x_0)$$

where x_0 is the current position along the mean block vector and Δx is the sampling position a distance away from x_0. A sampling Δx of a variable rate dependent on the image size was taken to smooth the partial derivative. Figure 2.16 shows the un-sampled partial derivative plot and Figure 2.17 shows the sampled plot for each 1-D signal. The maximum of the finite difference

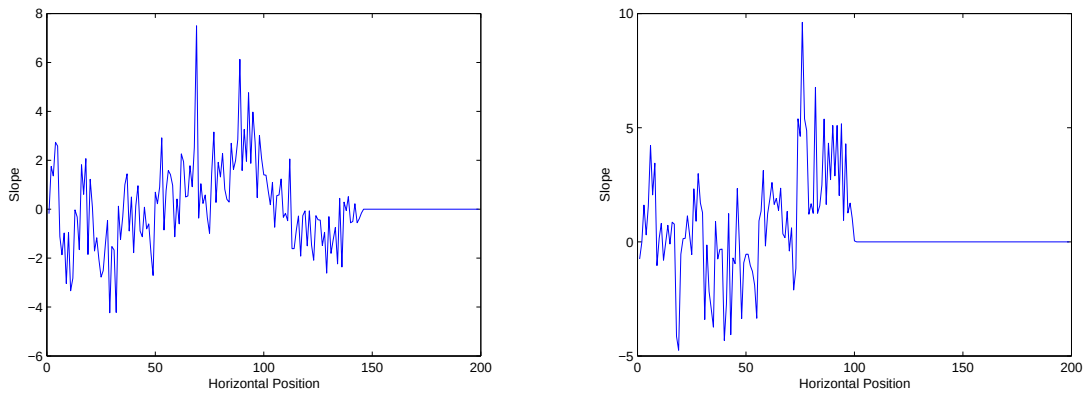

Figure 2.16: Un-sampled partial derivative finite difference plot.

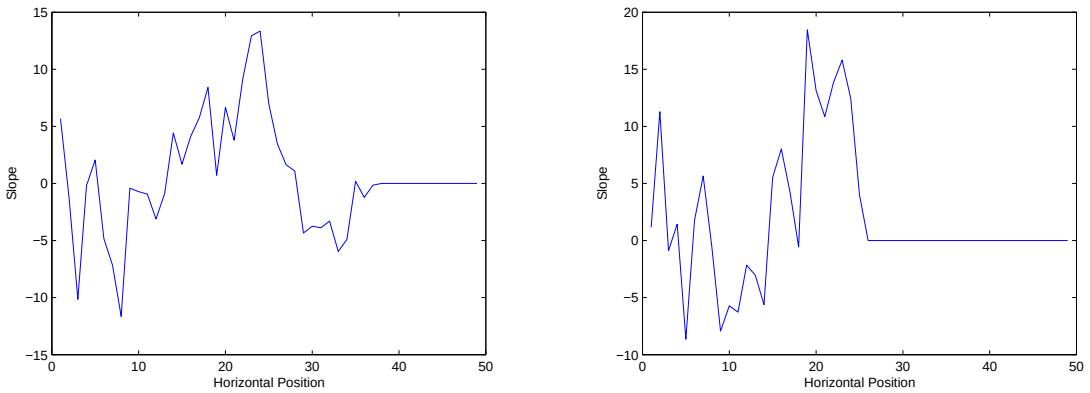

Figure 2.17: Sampled partial derivative finite difference plot.

gives an approximation of the iris's radius on each side of the pupil. This gives an approximate idea of the greatest intensity changes in the image, and helps in the approximation of an iris radius. Since we are only concerned with the limbic boundary between the iris and sclera of the eye (which is a positive derivative across the 1-D signal), the negative portions of the signal can

be removed as shown in Figure 2.19 and equation 3.4.

$$\mathbf{X}_{fd}(x_0) = \begin{cases} 0 & (\mathbf{X}_{block}(x_0 + \Delta x) - \mathbf{X}_{block}(x_0)) < 0; \\ (\mathbf{X}_{block}(x_0 + \Delta x) - \mathbf{X}_{block}(x_0)) & (\mathbf{X}_{block}(x_0 + \Delta x) - \mathbf{X}_{block}(x_0)) > 0; \end{cases} \tag{2.4}$$

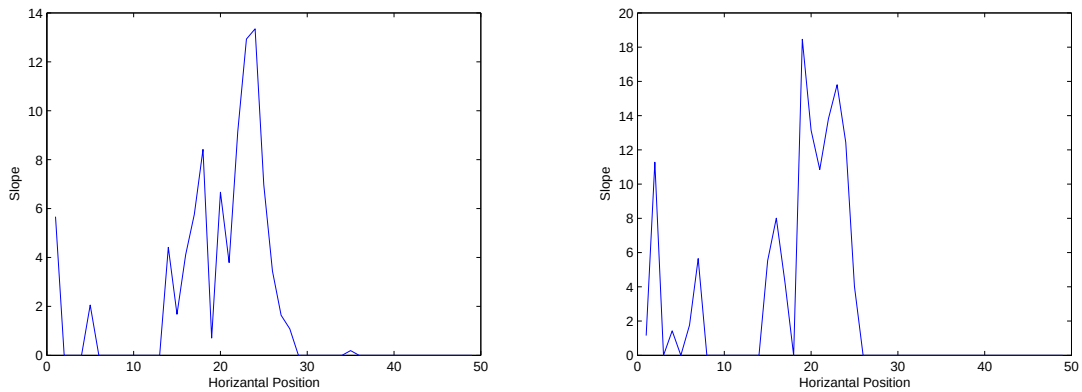

Figure 2.18: Discarding of the negative portions of the derivative.

The signal is then squared in order to enhance the peaks. The final plots of the 1-D signals derived from the ROIs in the image are shown in Figure 2.19. The maximum peak in the signal

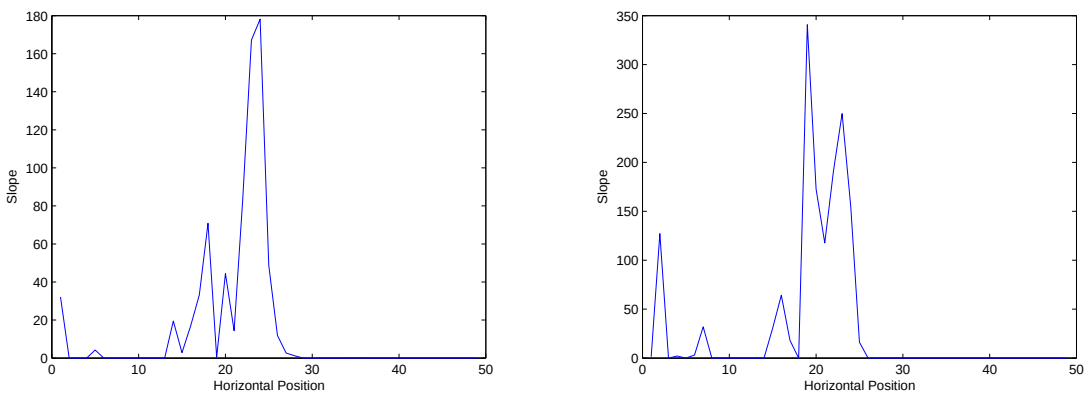

Figure 2.19: Removal of the negative portions of the derivative.

is now detected which corresponds to the limbic boundary. It is detected by simply taking the maximum of the final signal and multiplying it by the rate at which it was downsampled in order to get the column in the ROI image that corresponds to the limbic boundary I_{LB}.

$$I_{LB} = (max(\mathbf{X}_{fd})) * \Delta x$$

This is a very good approximation to the radius of the iris. However, since we have two ROIs we also have two estimates of the radius. Often the pupil is slightly nasal so the iris radius on the side of the nose is usually shorter than the iris radius on the side away from the nose. So, the greater of the two estimated radii is taken as an approximate iris boundary.

A circular ROI based on the localization radius is then extracted in order to separate the iris from the non-iris portions of the image. All the pixels pertaining to non-iris structures are set to white in order to process only the iris structure (Figure 2.20). Patches inside the circular ROI

(a) Circular localization mask (b) Removal of non-iris pixels

Figure 2.20: Removal of the negative portions of the derivative.

that only contain iris texture are defined as in Figure 2.21. These patches are defined based on the localization and pupil segmentation. The patches correspond to the actual iris intensities. The minimum and maximum of the patches are computed and they are used to set minimum and maximum thresholding values, where the iris intensities corresponds to the intensities between the min and max. Since the iris contains dark portions corresponding to the crypts and freckles, which may not fall into the patches, the threshold is slightly negatively weighted by 10 gray levels. This weighting compensates for any pixel intensities that were not in the predefined patches. This constitutes a dynamic threshold in the sense that the threshold is defined dynamically for each individual iris based on an actual patch of iris pixels. This improves the segmentation (Figure 2.22) of the iris in the IR channel. This procedure can be performed across all 4 channels, but problems often arise in the blue channel of a brown iris, due to more subcutaneous veins showing up in the sclera in the image that confounds the segmentation. Therefore, this operation is only performed in the IR channel where no vein patterns are present due to the high reflection from

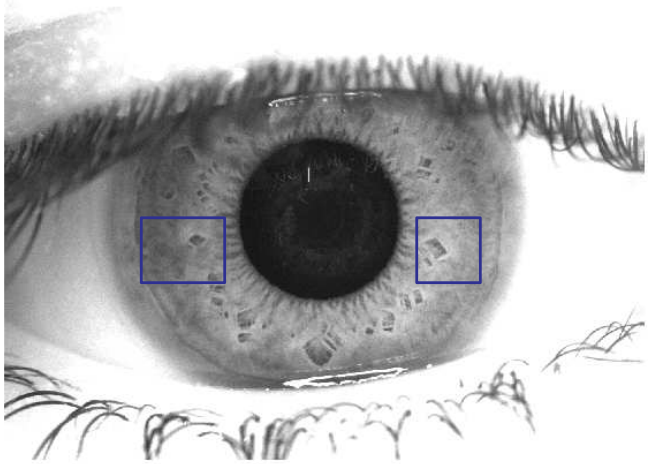

Figure 2.21: Portions of the image selected as a representation of the iris pixel intensities.

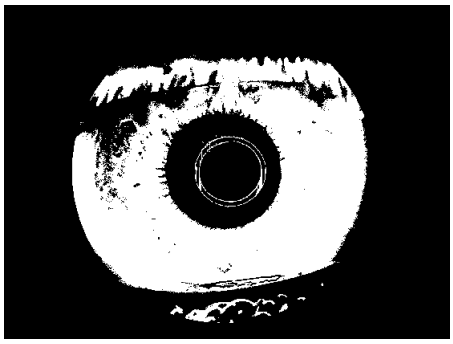

Figure 2.22: Dynamic thresholded image.

the sclera.

The dynamically thresholded image still contains many eyelashes as can be seen in the upper most portion of Figure 2.22. These portions still need to be removed from the image. Therefore, morphological operations are applied to the image in order to remove the remaining eyelash structures. First, a weighted hole filling operation is performed (Figure 2.23). The hole filling is performed to the area (rows and columns) of the image that is below the pupil so that only holes in the iris are filled and the holes associated with eyelashes remain. The hole filling is followed by

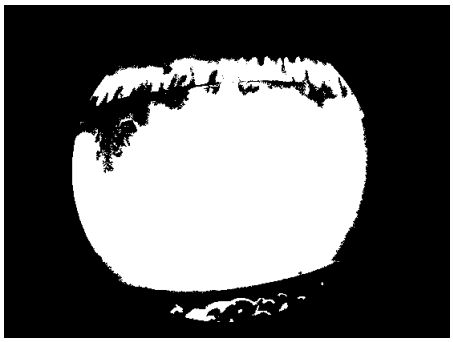

Figure 2.23: Bottom weighted hole filling .

a slight morphological closing operation (Figure 2.24), with a small disk size dependent on the image size, weighted above the pupil and a second filling below the pupil in order to fill in regions that may have been left open around the iris. A morphological opening operation, performed on

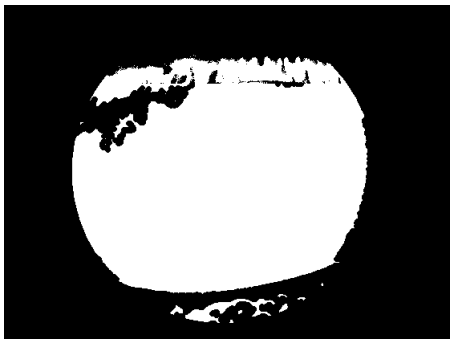

Figure 2.24: Morphological closing and second filling.

the area of the image above the pupil, can then be performed in order to remove much of the

eyelashes. The morphological opening's disk size is much larger than the disk used in the closing, 4 times the disk size of the closing. This removes much of the remaining eyelashes as can be seen in Figure 2.25. Some eyelashes may still be present so another eroding operation weighted

Figure 2.25: Morphological opening of the area above the pupil.

above the pupil is performed to remove them as shown in Figure 2.26. The largest remaining

Figure 2.26: Morphological eroding of the area above the pupil.

object is selected as the final iris structure. The ensuing boundary boundary is used as the limbic boundary of the iris. Figure 2.27 shows the final segmentation result of the dynamically segmented iris in the IR channel overlaid across all channels. This can be used to segment the other coregistered eye image channels as well.

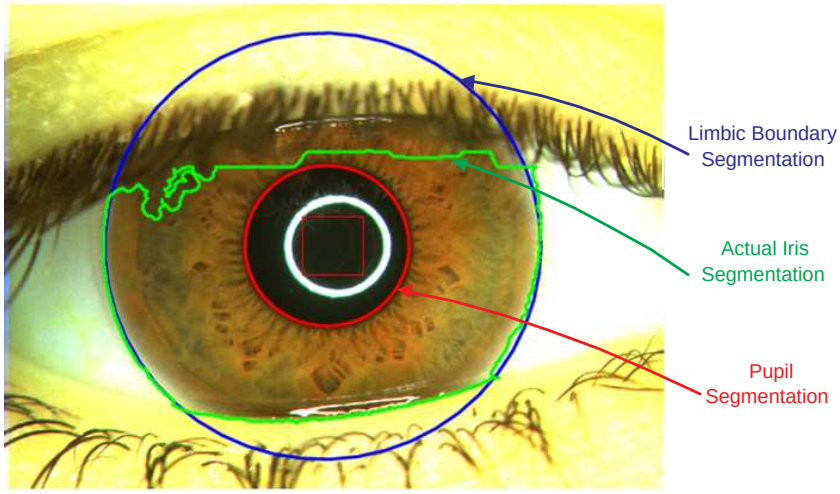

Figure 2.27: Final Segmentation Result.

2.4 Multispectral Iris Segmentation

2.4.1 Color Segmentation

Color region based segmentation techniques utilize the RGB color vectors in order to segment an image. The concept is rather simple. Suppose that you are given a color sample set that represents a color or set of colors in an image. To segment the color from the rest of the image the "average" or "mean" of the previously chosen color set is selected and classified as having a color in that specific range or not in all the RGB pixels. The classification is performed by taking the similarity measure using the Euclidean of the RGB vector. Let $\mathbf{m}$ denote the RGB column vector and $\mathbf{z}$ denote an arbitrary point in the RGB vector space. The Euclidean distance is then calculated as

$$D(\mathbf{z}, \mathbf{m}) = ||\mathbf{z} - \mathbf{m}|| = [(\mathbf{z} - \mathbf{m})^T(\mathbf{z} - \mathbf{m})]^{1/2} = [(z_R - m_R)^2 + (z_G - m_G)^2 + (z_B - m_B)^2]^{1/2}$$

where $\| \bullet \|$ denotes the norm of the argument and R, G, and B, denotes the RGB component vectors. In this work the RGB vector is extended to include the IR channel in the multispectral image. Therefore the image is concatenated, IR channel first, to make the multispectral IR-RGB image. Thus the Euclidean equation becomes

$$D(z, m) = [(z_{IR} - m_{IR})^2 + (z_R - m_R)^2 + (z_G - m_G)^2 + (z_B - m_B)^2]^{1/2}$$

A threshold is taken around the locus of the points corresponding to the test color so that D($\mathbf{z}$,$\mathbf{m}$)≤T is a solid sphere of radius T that isolates the selected color. The points outside the sphere threshold T are coded as black whereas the points inside the sphere are coded as white to produce a binary color segmented image.

The Euclidean distance equation is often generalized to the Mahalanobis distance measure of the form [38]

$$D(\mathbf{z}, \mathbf{m}) = [(\mathbf{z} - \mathbf{m})^T \mathbf{C}^{-1} (\mathbf{z} - \mathbf{m})]^{1/2}$$

In the Mahalanobis distance $\mathbf{C}$ is the the covariance matrix defined by [39]

$$C = COV(\mathbf{x_1}, \mathbf{x_2}) = E[(\mathbf{x_1} - \mathbf{m_1})(\mathbf{x_2} - \mathbf{m_2})]^{1/2}$$

where E is the expected value of random variables x_1 and x_2 and m_1 and m_2 are the means of those random variables respectively.

Unlike the circular threshold of the Euclidean distance in the RGB vector space classification using the Mahalanobis distance, with the locus of points such that D($\mathbf{z}$,$\mathbf{m}$)≤T, describes a 3-D elliptical body with the principal axes oriented in the direction of maximum data spread, thus increasing classification robustness. The Mahalanobis distance can be reduced to the Euclidean distance by replacing the covariance matrix C with the identity matrix. In this work the IR-RGB vector space is classified using the elliptical Mahalanobis distance to segment the iris due to its robust nature.

Pupillary Boundary Segmentation

In order to segment the pupil using the color based Mahalanobis segmentation, the masks of the pupil must be defined. The masks are generated using the thresholding scheme of the IR channel previously described in section Infrared Iris Segmentation. Where the pupil is found through the iterative process, however, it needs to segment a very small portion of iris pixels in order to perform the classification The binary mask and mask overlaid across a CIR (IR, R, G composite image) image can be seen in Figure 2.28. The covariance matrix and mean vectors are then computed from the mask and the Mahalanobis distance is used to classify the pupil according to the mask image. The result of the Mahalanobis classification is a binary image which can be seen in Figure 2.29. Like the IR segmented image in the previous section discontinuities in the image exist therefore it is subjected to the same morphological operators

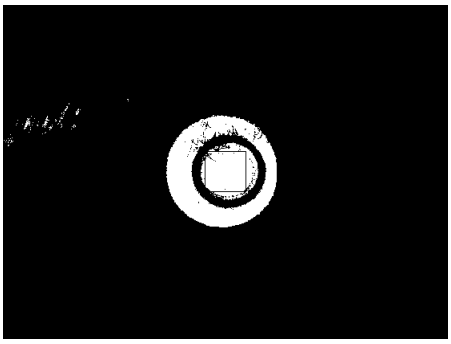

(a) Color segmentation mask

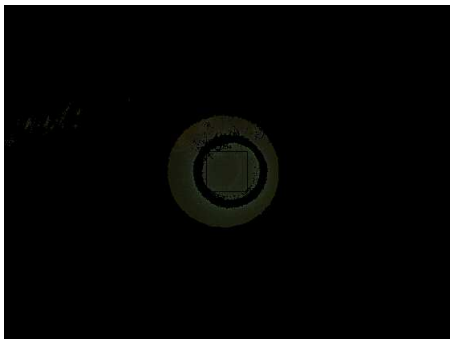

(b) Overlay of mask on a CIR image

Figure 2.28: Pupil masks for color based Mahalanobis pupil segmentation.

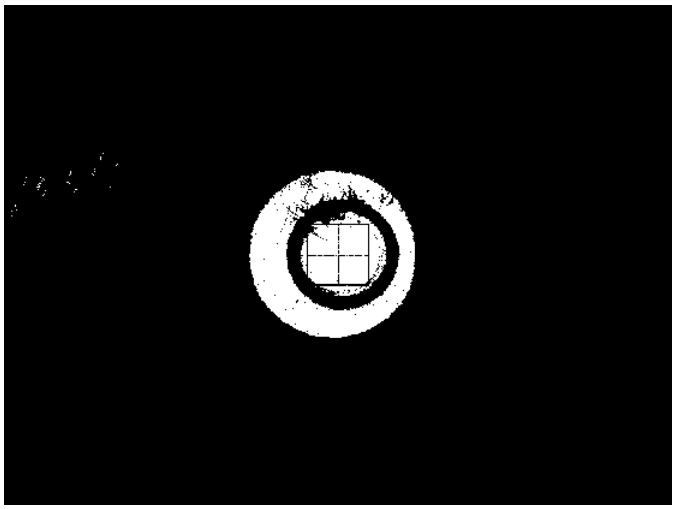

Figure 2.29: Color based Mahalanobis pupil segmentation.

and vertical connectivity selection. The result of the largest object selection after these operations can be seen in Figure 2.30. The boundary of the object is taken as the pupillary boundary of

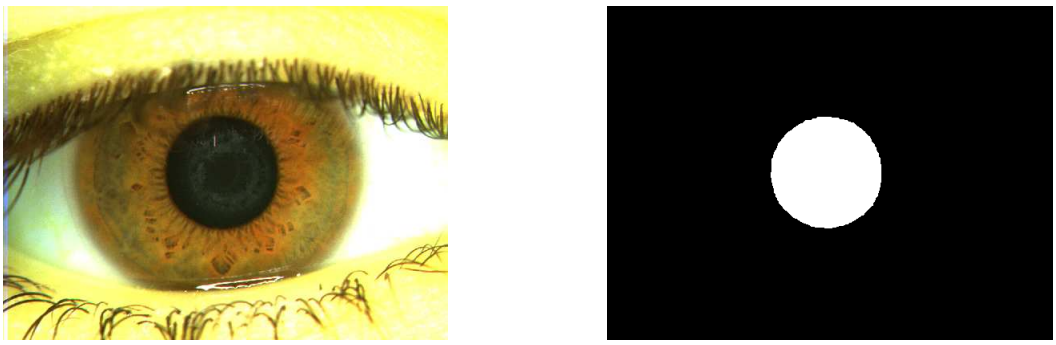

Figure 2.30: Color based Mahalanobis pupil segmentation after morphological processing.

the iris.

Limbic Boundary Segmentation

To segment the iris at the limbic boundary and along the top and bottom eyelashes, the Mahalanobis color-based classification is used. The image is first localized using the IR channel localization technique to find a portion of the image that only corresponds to the iris color pattern. Regions of interest that correspond to only the iris's color pattern are selected as masks for the Mahalanobis classification. The ROIs can be seen in Figure 2.38 as the dark blocks in the iris region. Since the iris pattern is typically radial, from the pupil to the limbic boundary, in nature the intensities contained within the iris patches are a good approximation to the iris color. The masks are used to compute the covariance matrix and mean vectors for the Mahalanobis distance classification. The binary image (Figure 2.32) is the result of the color classification. Due to the fact that some of the crypts have the same dark color associated with the eyelashes, much of the eyelashes are segmented along with the iris. To combat this, various morphological and filtering operations are applied to the image to get the final segmented iris (Figure 2.33 (a)). Figure 2.33 (b) shows the final boundary overlaid on the CIR iris image.

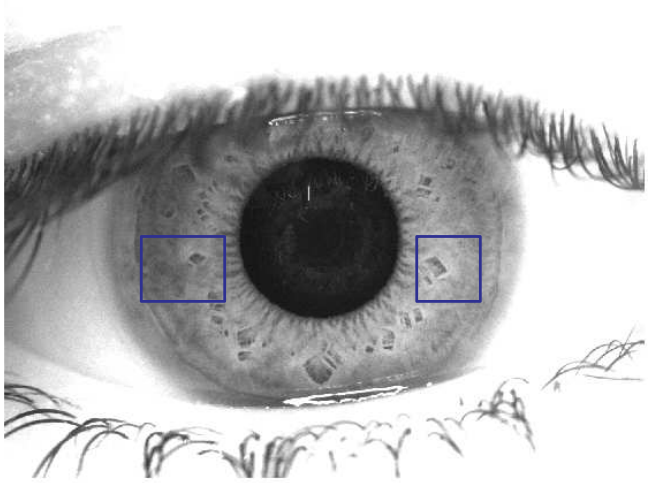

Figure 2.31: Portions of the image selected as a representation of the iris color class.

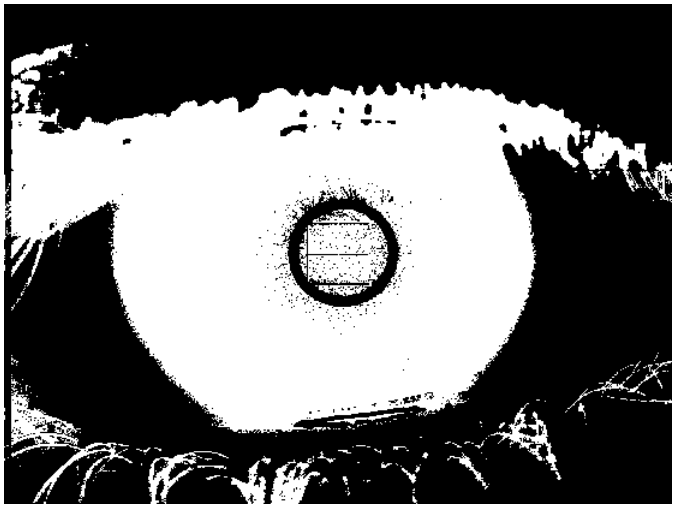

Figure 2.32: The Result of the Mahalanobis color classification of the iris. White pixels correspond to areas of the image that are classified by color as iris and black pixels correspond to areas of the image that are classified as non-iris

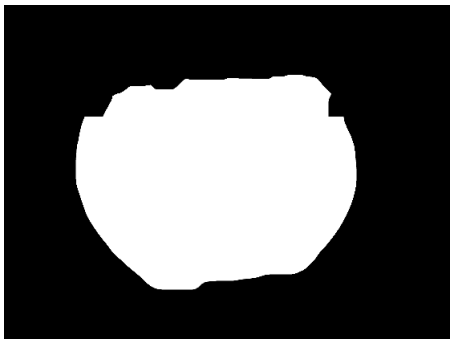

(a) Binary mask indicating the color segmentation

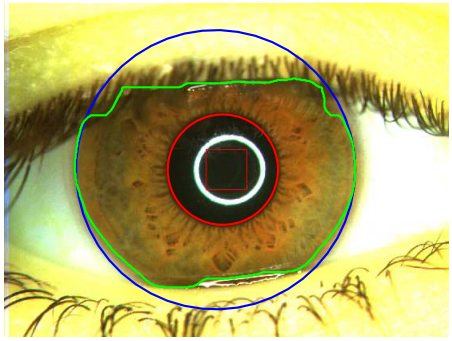

(b) Overlay of the iris boundary on a CIR image

Figure 2.33: Final result of the Mahalanobis color classification segmentation of the iris.

2.4.2 Multispectral Segmentation using Bayes classification

Optimum statistical classifiers have been used to classify multispectral (IR-RGB satellite images [38]) and hyperspectral (sup-pixel classification satellite images [40]) images. The Bayes function for a 0-1 loss function [38] has a decision function of the form

$$d_j(\mathbf{x}) = p(\mathbf{x}/\omega_j)P(\omega_j) \qquad j = 1, 2, ..., W$$

where $p(\mathbf{x}/\omega_j)$ is the probability density function (PDF) of the pattern vectors of class ω_j, and the probability that class ω_j occurs is $P(\omega_j)$. Given an unknown pattern vector (the image mask), decision functions W need to be computed. Then we need to assign the pattern to the class whose decision function yields the largest numerical value based on the computation of a total of W decision functions. $p(\mathbf{x}/\omega_j)$ is assumed to be Gaussian and so is assumed to be

$$p(\mathbf{x}/\omega_j) = \frac{1}{(2\pi)^{n/2}|\mathbf{C}_j|^{1/2}} e^{-\frac{1}{2}[(\mathbf{x}-\mathbf{m}_j)^T\mathbf{C}^{-1}(\mathbf{x}-\mathbf{m}_j)]}$$

where $\mathbf{C}_j$ is the covariance matrix, defined earlier, of the selected pattern population class ω_j and $|\mathbf{C}_j|$ is the determinate of $\mathbf{C}_j$. Likewise $\mathbf{m}_j$ is the mean vector of the pattern population class ω_j.

Since the logarithm is increasing monotonically, the largest $d_j(\mathbf{x})$ chosen is equivalent to choosing the the largest $\ln[d_j(\mathbf{x})]$. So instead of using 2.4.2 as the decision function we can use

$$d_j(\mathbf{x}) = \ln[p(\mathbf{x}/\omega_j)P(\omega_j)] = \ln(p(\mathbf{x}/\omega_j)) + \ln(P(\omega_j))$$

The logarithm is guaranteed to be real due to the fact that $p(\mathbf{x}/\omega_j)$ and $P(\omega_j)$ are always nonnegative. If the Gaussian PDF equation is substituted into (2.4.2) then the equation becomes

$$d_j(\mathbf{x}) = \ln(p(\mathbf{x}/\omega_j)) - \frac{n}{2}\ln(2\pi) - \frac{1}{2}\ln(|\mathbf{C}_j|) - \frac{1}{2}[(\mathbf{x}-\mathbf{m}_j)^T\mathbf{C}^{-1}(\mathbf{x}-\mathbf{m}_j)],$$

where the term $(n/2)\ln(2\pi)$ is the same positive constant for all classes. So it is ignored yielding the classification equation for the decision function as

$$d_j(\mathbf{x}) = \ln(p(\mathbf{x}/\omega_j)) - \frac{1}{2}\ln(|\mathbf{C}_j|) - \frac{1}{2}[(\mathbf{x}-\mathbf{m}_j)^T\mathbf{C}^{-1}(\mathbf{x}-\mathbf{m}_j)] \qquad j = 1, 2, ..., W$$

The term inside the brackets is the Mahalanobis distance as in the color classification. The final derived equation for the Bayes classification of multivariate Gaussian patterns (2.4.2) is used to segment the iris from the rest of the eye.

Pupillary Boundary Segmentation

The Bayes classification is first applied to extract the pupil. So, a region that corresponds to the pupil and a region that corresponds to the rest of the image must be identified in order to deduce the masks for the Bayesian classification. These masks are established using the same dynamic thresholding technique as the IR pupil segmentation (see section Infrared Iris Segmentation). However, the initial thresholding of the mask can be more relaxed when compared to the IR segmentation because only a small portion of the pixels is needed to classify the pupil as seen in Figure 2.34 (a). The binary pupil image is taken as the approximate mask of the pupil and

(a) Binary pupil mask (b) Complement of pupil mask

Figure 2.34: Binary images of the thresholded multispectral channels.

the complement of the image is taken as a non-pupil mask (2.34 (b)). Classification is performed

using the Bayes classifier taking the two masks as the pattern classes to be classified. The result of the Bayes classification for the pupil can be seen in Figure 2.35. After the Bayes classifications

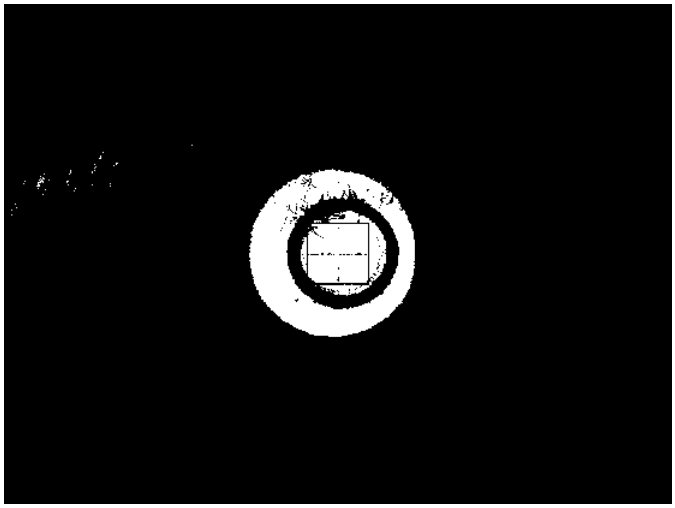

Figure 2.35: Result of the Bayes classification from the two filters.

problems can still occur in the image. The eyelashes are typically the same intensity as the pupil, and the ring light can create open areas in the region of the pupil. To remove these open areas in the pupil a morphological closing operation is performed (Figure 2.36) followed by a filling of all the holes. This creates a solid pupil structure. Occasionally, portions of the eyelashes are still present in the binary image. Thus, a check for connectivity is performed next. The pupil is longer than the eyelash structure in the y direction or along each column of the image, whereas the eyelashes are typically longer in the x direction or along each row of the image. So, each column of the binary image is checked to find the object with the maximum connectivity. This value (i.e. the maximum connections) is taken as an approximate diameter of the pupil and the object with this diameter is the segmented pupil (Figure 2.37).

Limbic Boundary Segmentation

In order to perform the Bayes classification to segment the iris, some preliminary operations must first be conducted. The IR channel was selected to do these operations due to its abilities of imaging better across multiple eye colors, particularity the brown eye. The IR channel is taken

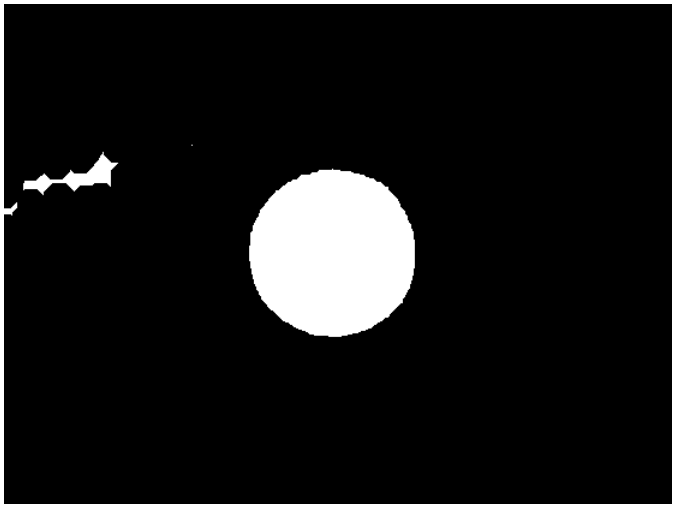

Figure 2.36: Morphological closing of the Bayes classified pupil.

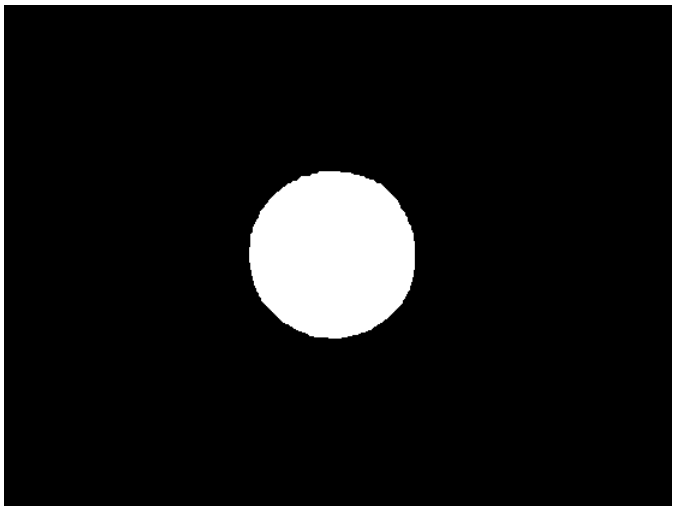

Figure 2.37: Segmented Pupil.

and a localization (see section Infrared Iris Segmentation) is computed in order to simplify the segmentation. The localization gives an approximation to the actual radius of the iris.

After the approximate localization the boundary is used as a starting point for the selection of multispectral portions of the image in order to classify the components of the image using Bayesian classification. First, samples representative of each pattern class need to be defined to obtain the mean vectors and covariance matrix. These samples are obtained from a set of iris images designated as the training set. Examples of iris and non-iris samples are indicated in Figures 2.38 and 2.39.

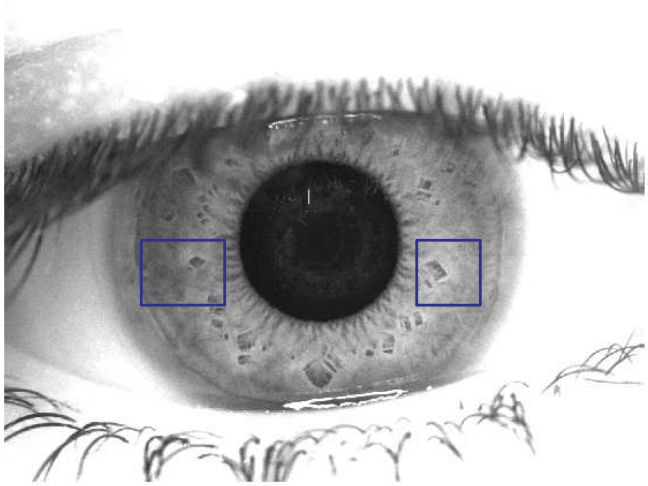

Figure 2.38: Portions of the image selected (black mask) as a representation of the iris pattern class.

All the channels IR, R, G, B are organized into a 3-Dimensional matrix correspondingly concatenated in the 3rd dimension. Since the images are registered spatially this simplifies the concatenation and region selections. Thus, every pixel is a combination of the four channels and can be viewed as a four dimensional pattern vector in the image. These four dimensional vectors are extracted from the iris and non-iris pattern masks, and the covariance matrices and mean vectors are computed for each mask. The Bayes classification is computed using the covariance and mean vectors of the entire image. The classifier can classify according to it input mask. If more than one representative pattern mask was designed for a class 1) corresponds to iris texture 2) corresponds to eyelashes 3)corresponds to eyelids and 4) corresponds to the sclera

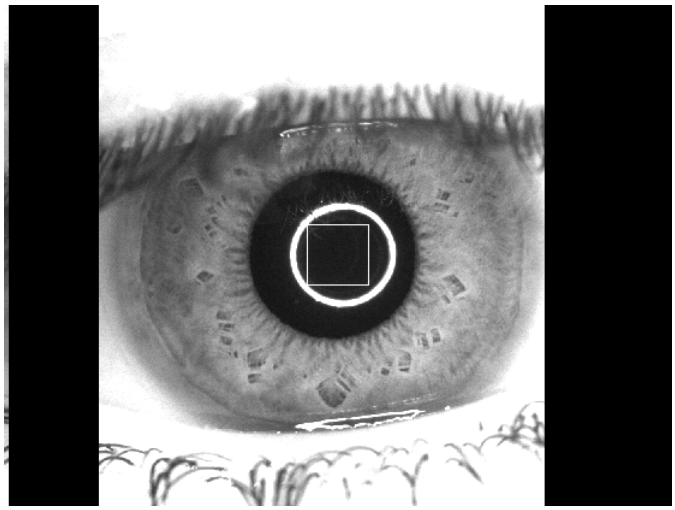

Figure 2.39: Portions of the image selected (Black mask) as a representation of the non-iris pattern class corresponding to the portions of the eye such as the eyelashes, eyelid and sclera.

than the Bays classification would have output a classification for each input. Since it is difficult to preclassify the components of the eye image, only two masks were selected (iris and non-iris classes). Thus a binary image is the result of the classification, as can be seen in Figure 2.40. Notice in the image that due to the fact of structures in the iris such as crypts that the bayes classification picks up certain features, such as the eyelashes that have a similar pattern as the crypts in the iris texture. Thus the Bayes classifier does not result in a good segmentation of the iris, and other image processing techniques must be applied to get a more robust iris segmentation.

Since the classified binary image gives a better boundary gradient, the localization approximation is again used to determine a more precise iris radius. The final output of the 1-D signal for detecting the peaks can be seen in Figure 2.41. The largest radii is selected and circular ROI is taken from the image (Figure 2.42). This effectively separates all iris texture from any non-iris patterns. Since the Bayes classification has separated certain portions of the non-iris pattern as iris pattern, because of the crypts, we now can distinguish it via the circular ROI. Now the classifier can be used again with 3 classes pertaining to 1) the iris pattern (as previously segmented) 2) non-iris pattern that was classified as iris pattern (mainly patterns of the eyelashes) and 3) non-iris pattern that was not classified as iris pattern (patterns of the sclera and eyelids). The

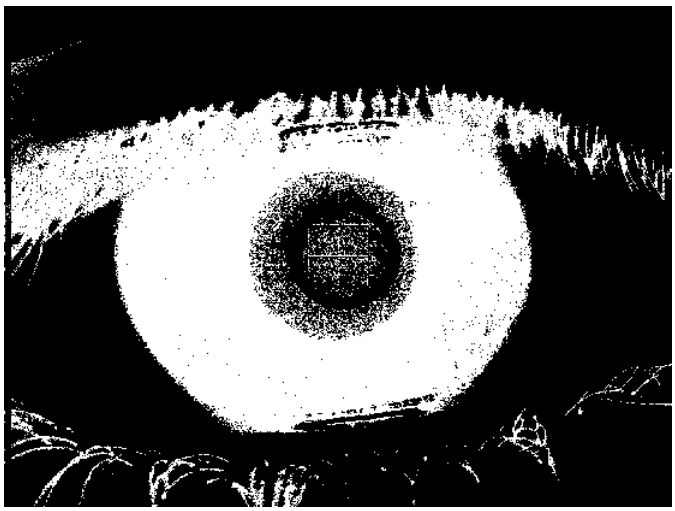

Figure 2.40: Result of Bayesian classification of the non-iris and iris patterns.

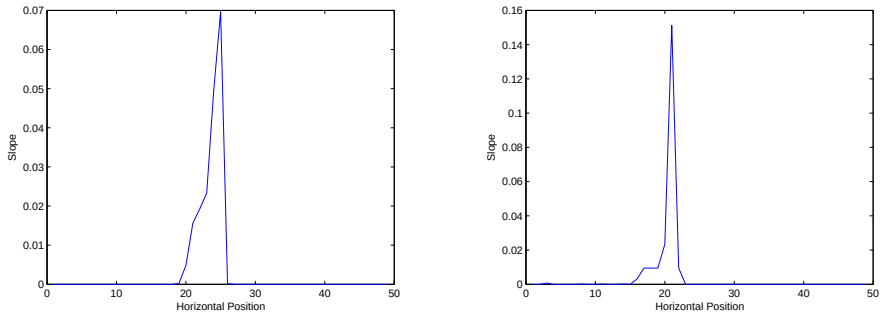

Figure 2.41: Determination of an approximate iris radius via the binary image of the Bayes classification.

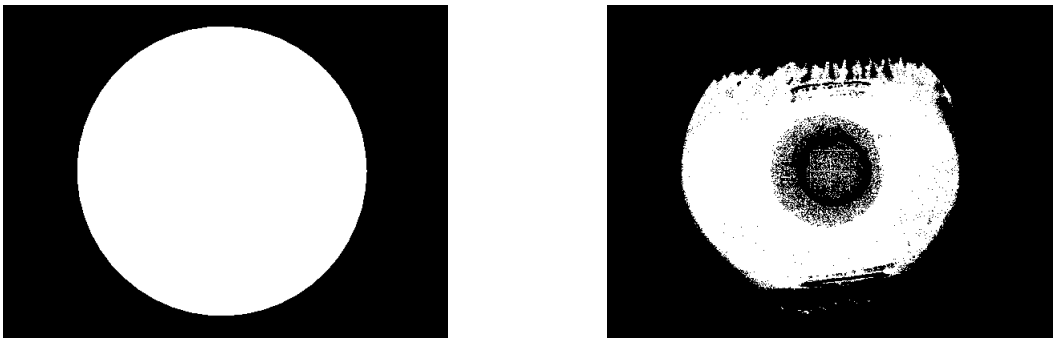

Figure 2.42: Circular ROI detected from the approximate radius, left circular ROI, right region segmentred.

three masks are then used to perform a second Bayes classification. The resulting masks can be seen in Figure 2.43.

(a) Iris mask (b) Eyelash mask (c) Sclera and Eyelid mask

Figure 2.43: Three masks used for the second Bayes classification.

The classification more effectively classifies all iris and non-iris patterns except the regions where the darker parts of the iris corresponds to patterns of the eyelashes, as can be seen by the spurious pixels located in the eyelash regions and the holes in the iris region in Figure 2.44. However, this still yields a better segmentation of the overall iris structure than the previous two pattern classification technique.

While the second Bayes classification aids in the detection of the eyelashes, it does not detect the actual limbic boundary as can be seen in Figure 2.45. Therefore, a combinations of the two classifications will get a better result. So, the portion of the image above the top of the pupil where the eyelashes are present is composed of the binary image of the second classification, whereas, the bottom half of the image below the top of the pupil is composed of the binary

Figure 2.44: Bayes classification of iris pixels with the three masks shown in figure 2.43.

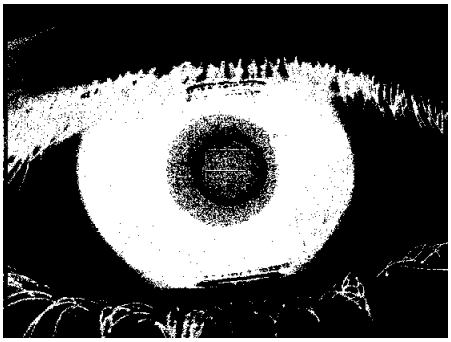

(a) Initial Bayesian Classification

(b) Subsequent Bayesian Classification 2

Figure 2.45: Comparison of the two Bays classifications.

image of the first classification. The split composite image of the two classifications can be seen in Figure 2.46. Using the circular ROI, the majority of the remaining white pixels of non-iris

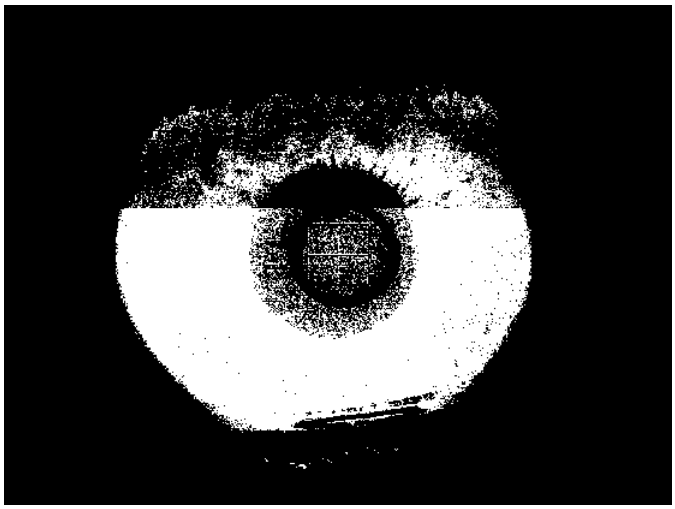

Figure 2.46: Split composite image of the Bayes Classification.

patterns outside the ROI are removed. However, there still are some discontinuities in the iris that need to be processed out. These discontinuities are removed by morphological and filter operations performed to either the area above the pupil or weighted to the area below the pupil as in Figure 2.47. The operations include: 1) a below the pupil weighted hole filling followed by 2) a median filtering, to remove "salt and pepper" like noise from the binary image, 3) a weighted closing operation to enclose the pupil, 4) a second hole filling to fill in the pupil and 5) a median filter to smooth the boundary of the iris binary mask, and 6) a final erosion weighted above the pupil just in case some eyelashes are still present. The final result, after the erosion, is taken as the segmented iris. The border of the segmentation is taken as the limbic boundary of the iris. Figure 2.48 shows the final segmentated result.

2.5 Segmentation Performance Comparison

The segmentation results on 10 different eye images can be seen in Figures 2.49 and 2.50. A visual glance indicates that the Bayesian classification does well in extracting only the iris pattern, while not extracting non-iris structures such eyelashes. While the color segmentation

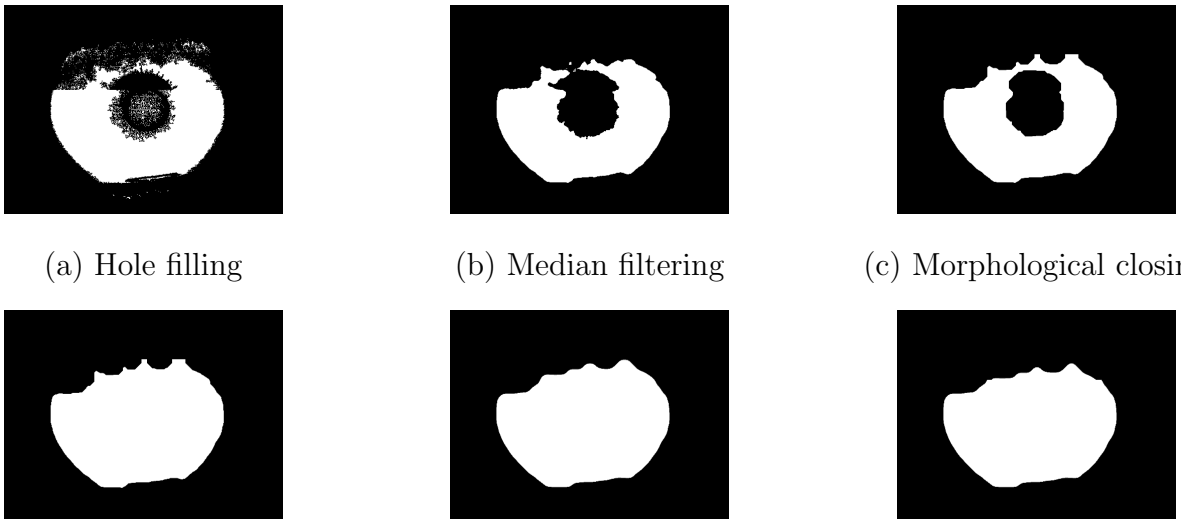

(a) Hole filling (b) Median filtering (c) Morphological closing

(d) Hole Filling (e) Median filtering for Smoothing (f) Morphological erosion

Figure 2.47: Morphological and filtering operations performed in order to enhance the Bayes classification.

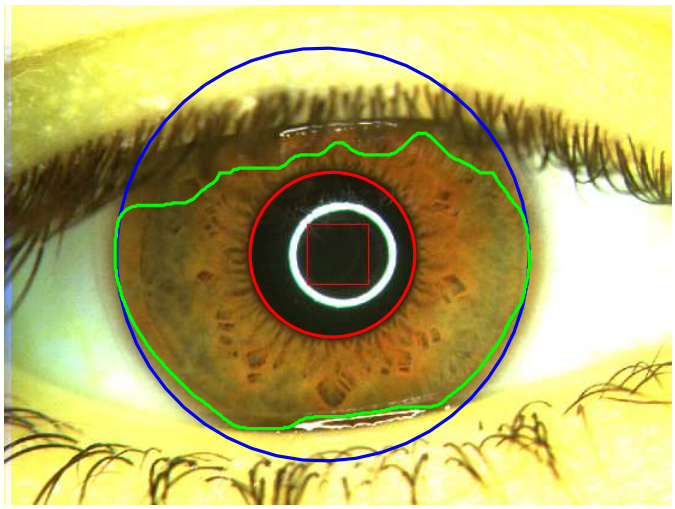

Figure 2.48: Final segmentation of an iris using Bayesian classification of the multispectral image.

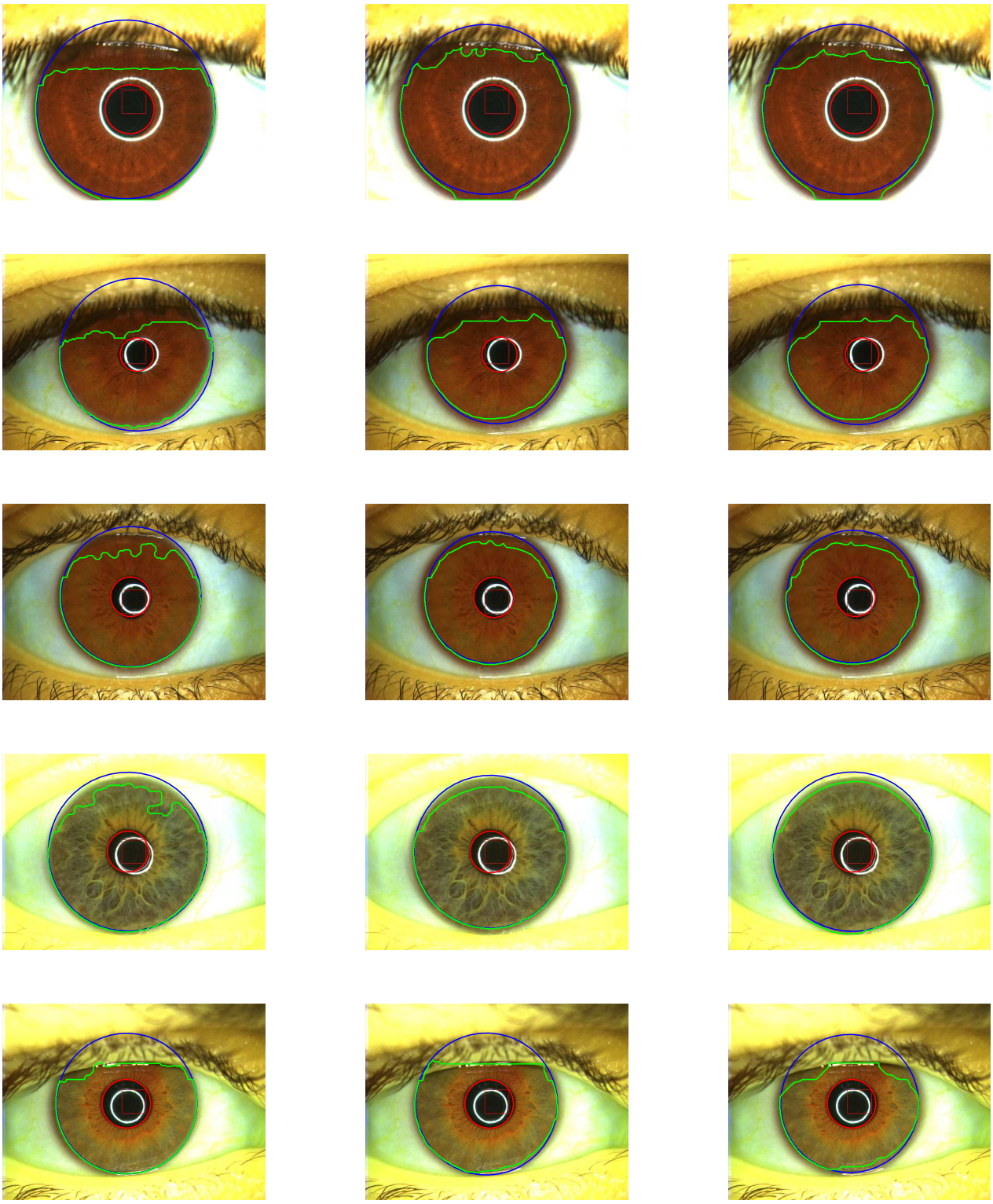

(a) IR segmentation (b) Color segmentation (c) Bayes segmentation

Figure 2.49: Comparison of iris segmentation across various colored eyes.

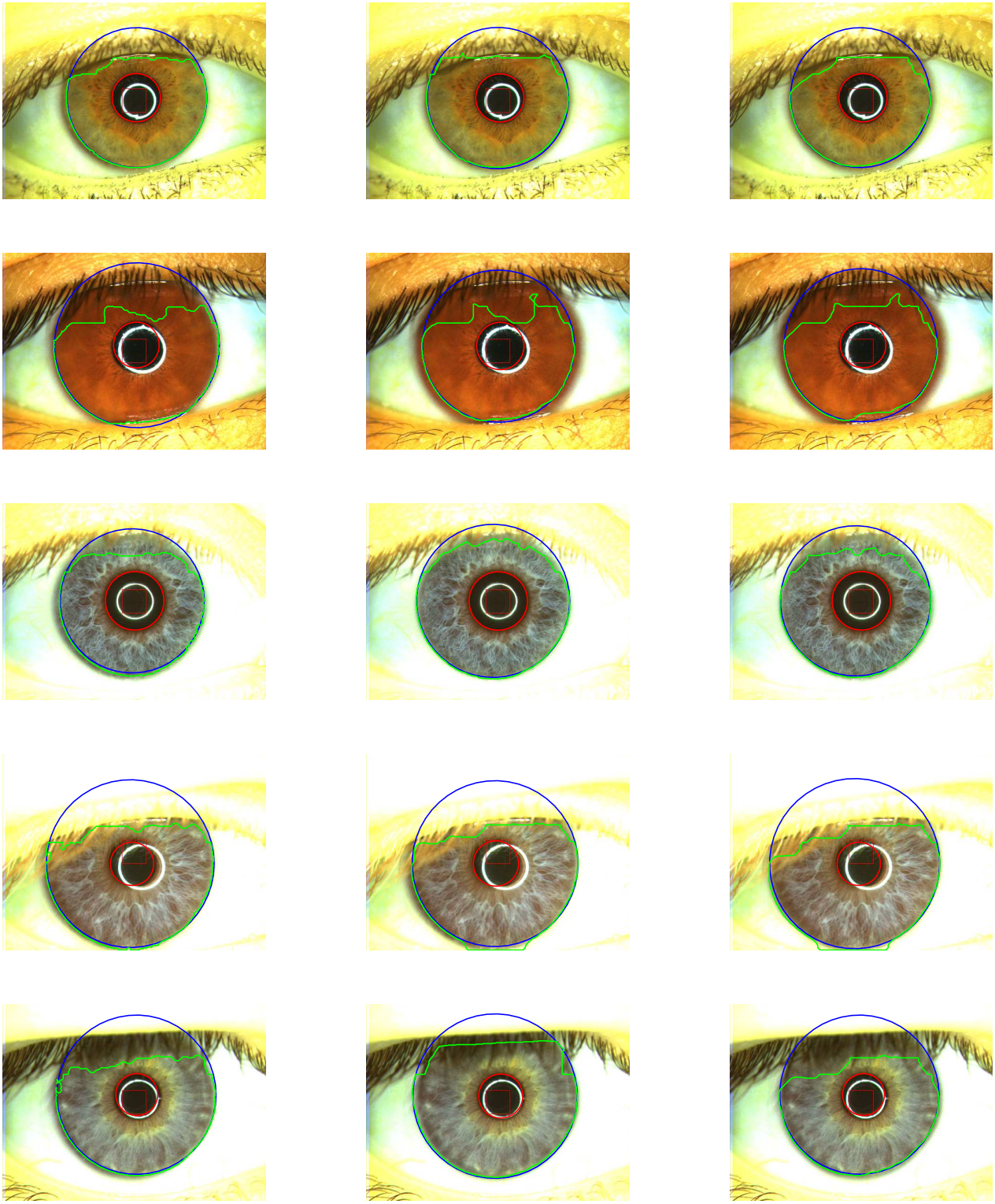

(a) IR segmentation (b) Color segmentation (c) Bayes segmentation

Figure 2.50: Comparison of iris segmentation across various colored eyes.

scheme appears to perform the worst picking up various portions of the eyelashes across the image. Color does not seem to be a factor when segmenting the iris. Each color is segmented appropriately, however, some blurry eyelashes in the image cannot be segmented out, but the Bayesian segmentation still seems to get the best result on the blurry eyelashes as can be seen in Figure 2.50 in the second blue eye image.

The entire data set (35 subjects 70 eyes) was used for segmenting and a texture based matching scheme was used in order to perform verification across the different types of segmentations. Since the same feature extraction and matching scheme was used for each segmentation the performance of the segmentation only is reflected in the ROC curves.

Texture Based Iris matching

In order to match the structure of the segmented iris a classical baseline texture based matching was used. After the iris segmentation is completed a fixed dimensional feature vector needs to be generated in order to match the images. Daugman proposed the rubber sheet model which maps each point in the (x, y) domain to a pair of polar coordinates (r, θ). This requires a circular or elliptical approximation of the iris structure which is taken from the iris limbic bounadray. The unwrapping results in a fixed size unwrapped rectangular iris image [6]. The image is also accompanied by an image mask. The mask is taken as the actual iris boundary as defined by either of the three segmentation schemes (the green and blue lines in the segmentation images in Figures 2.49 and 2.50).

To extract the textural information from the unwrapped rectangular image Gabor filters are used. A 2-D Gabor filter over an image domain (x, y) is given by

$$G(x, y) = e^{-\pi[(x-x_0)^2/\alpha^2+(y-y_0)^2/\beta^2]} e^{-2\pi i[u_0(x-x_0)+\nu_0(y-y_0)]}$$

where (x_0, y_0) specifies the center of the Gaussian filter, α and β are the width and length of the filter, (u_0, ν_0) specify the modulation with frequency $\omega_0 = \sqrt{u_0^2 + \nu_0^2}$ and orientation $\theta = \arctan(\nu_0/u_0)$. Radially, as you move from the pupil to the outer portions of the iris, the texture features of the iris change prominently. Thus, a set of three Gabor filters, orientated the same (0°), but with different scales and frequency are applied to specific regions of the "normalized" iris as shown in Figure 2.51[41]. Complex-valued phase information of the image is the result of the Gabor filters. A quantization of the phase information is done into four

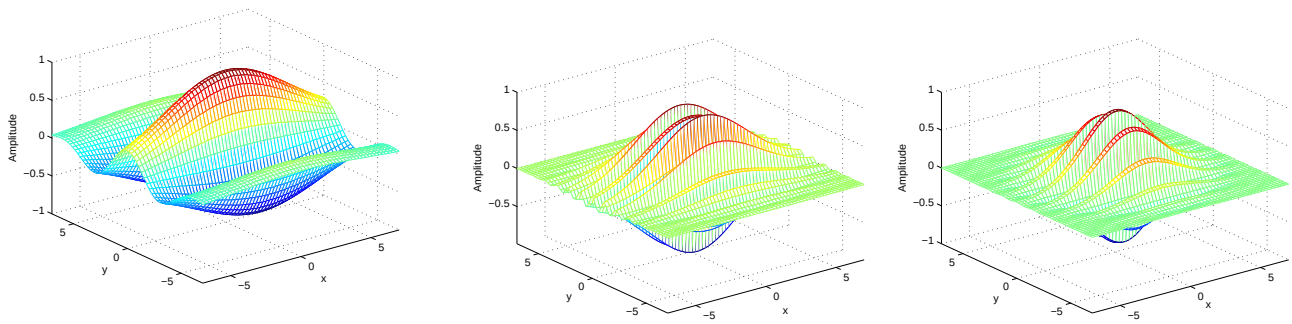

Figure 2.51: Real part of 2-D Gabor wavelet filters.

quadrants in the complex plane resulting in a complex-valued bit whose real and complex parts can be either 0 or 1. An "iriscode", a binary feature vector containing the 0s and 1s, is the final result. The Hamming distance, a measure of the difference in bits, is used to compute the final matching scores to determine how different two template iriscodes are. The Hamming distance is a dissimilarity score and is calculated using the bits corresponding to the iris pixels by utilizing the binary masks generated in the segmentation process. Let I_1 and I_2 be the two iriscodes to be compared, and M_1 and M_2 be their relative masks. The Hamming distance (HD) is calculated as follows:

$$HD = \frac{||(I_1 \bigotimes I_2) \bigcap M_1 \bigcap M_2||}{||M_1 \bigcap M_2||}$$

where the XOR operator, $\bigotimes$, detects the disagreement between the corresponding bits in the iriscodes, the AND operator, $\bigcap$, ensures that the Hamming distance is calculated using only the bits generated from the true iris region and the $||\,.\,||$ operator computes the norm of the bit vector. When comparing the genuine and imposter scores in an ideal population, the Hamming distance between two images of the same iris will be 0 (genuine score) and that between two images of different irises will be (0.5) (impostor score). However, due to occlusions and other factors affecting image quality the typical system will have a threshold between the imposter and genuine distributions as 0.3.

The result of the texture based matching can be seen in the receiver operating characteristic (ROC) curves in Figure 2.52 for both the left and right eye, matched independently, of images that are downsampled by 40%. The downsampling is performed by lowpass filtering and then applying bilinear interpolation to construct a image that has 40% less pixels than the original image. The ROC curves indicated that all three methods can achieve a very high performance.

However, the feature lacking blue channel performs better in the Bayesian segmentation scheme when compared to the IR and color based.

Also, an experiment was preformed to access the possibility of matching iris images across multiple wavelengths [42]. Thus, the following comparisons were performed: IR vs. R, IR vs. G, IR vs. B, R vs. G, R vs. B, and G vs. B (Figure 2.53). The bar graph in Figure 2.54 suggests that the cross matching performance decreases as a function of the differences in wavelength of the participating images. For example, the IR (850nm) and the Blue (475nm) channels are separated by the greatest range across the electromagnetic spectrum. Therefore, the reflective texture response varies the greatest across this range. When matching images in these two ranges, significant variations in texture response results in inferior performance. This can be seen across the other spectral ranges as well. On the other hand, spectral channels whose differences in wavelength are relatively small do not exhibit such a drastic decrease in matching performance. For example, the ROC curve corresponding to G vs. B is observed to be better than that corresponding to IR vs. B. This phenomenon indicates that different wavelengths highlight various textural components of the iris, further underscoring the importance of conducting multispectral iris analysis.

2.6 Summary

A pivotal part of an iris recognition system is the segmentation of the iris from other components of an eye image. Commercial systems operated in the near-IR range due to its unperceived nature to the human eye. This chapter explored segmentation in an individual IR channel as well as across multiple channels (IR, red, green and blue) of a multispectral eye image. Due to the increase of information associated with an increase in the number of channels a multispectral segmentation scheme utilizing a Bayesian classification is shown to have a slightly increased performance. While a scheme based on color alone does not achieve as high of a performance. However, Each segmentation scheme described shows potential to be implemented into a recognition system in order to segment the iris from an image of the eye.

A second experiment to evaluate the performance of multispectral diversity across multiple wavelength channels of an iris was performed. The experiment indicated that cross channel matching performance degrades as the wavelength increases. Since the matching is performed

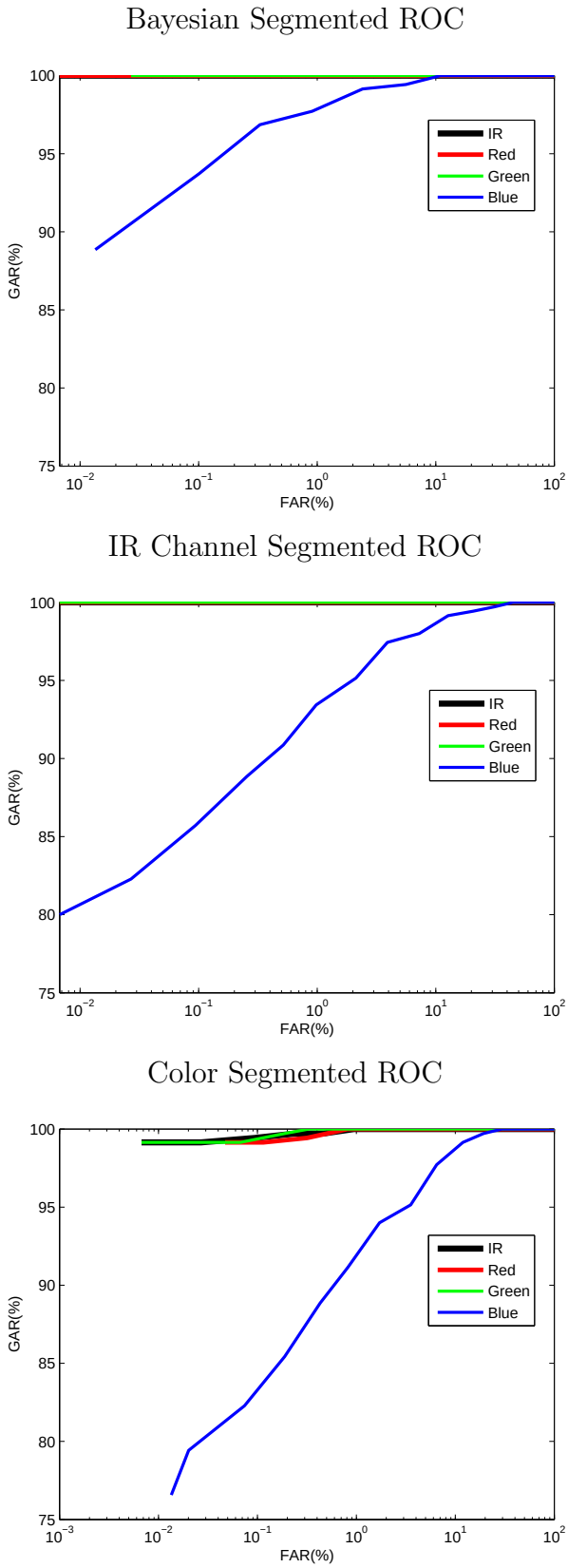

Figure 2.52: Texture Based Segmentation using Bayesian classification, the IR channel, and color segmented images.

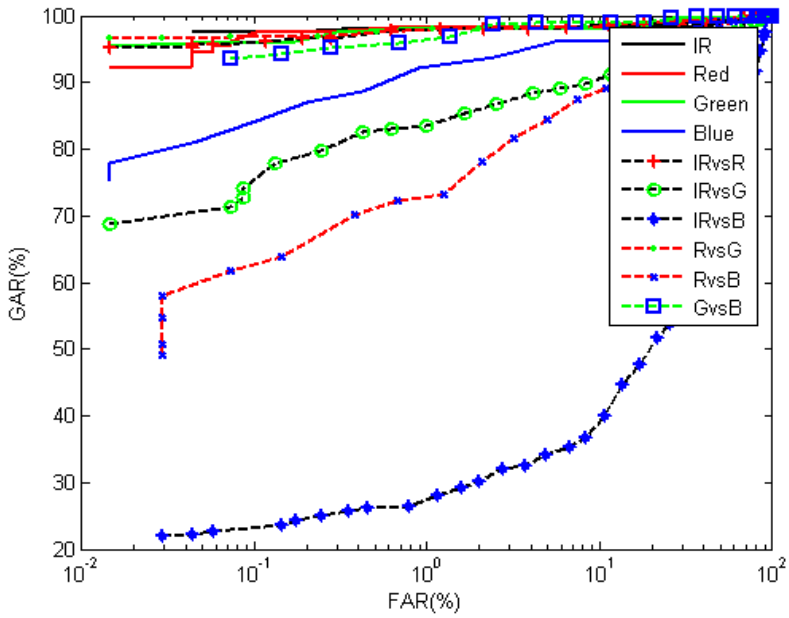

Figure 2.53: ROC curves indicating the cross channel matching performance

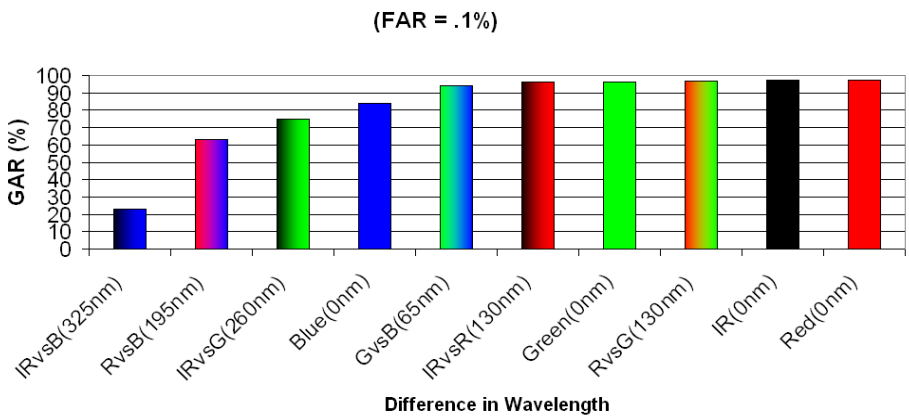

Figure 2.54: Plotting the Genuine Accept Rate (GAR) as a function of difference in wavelengths of participating images.

based on texture, this decrease in performance indicates that some structures in the iris are being represented differently by different wavelengths. Thus a further exploration of this texture deviation needs to be done.

Chapter 3

Multispectral Recognition

This chapter explores alternate techniques, apart from the classical texture based recognition, in order to perform recognition using multispectral information. The feature extraction is performed so that the result is a unique one Dimensional (1-D) signal, derived from concentric iris circles, for each channel. Due to the robustness of the extracted signal, the difference between the channels is used as a feature vector. This results in a 6 dimensional feature vector, one for each combination (IR-R, IR-G, IR-B, R-G, R-B, G-B). The matching of this feature vector is performed using the Euclidean distance and the sum fusion rule. The feature vector achieves a very high matching performance that is comparable to texture based methods (and superior to texture based methods at low resolutions). Also, since the 1-D decomposition is radial in nature it is not affected by motions of the iris or head shifting unlike the textural matching. Therefore, no circular shifting has to be performed to register the feature vectors.

3.1 Feature Extraction

In order to extract features from the iris, the segmented normalized image Figure 3.1) must first be determined. The normalized or unwrapped iris can be seen in Figure 3.2 (See section 2.5). The localized iris corresponds to the area between the blue and red segmentation boundaries in Figure 3.1. The ring light as well as portions of the pupil can be seen in the unwrapped image. Since the ring light is not always contained within the pupil of the unwrapped image it must be removed. Therefore, the ring light is located using a high intensity thresholding and the rows

corresponding to the high intensities are removed.

$$\begin{cases} r = 0 & n_r <= max(n_r) - t; \\ r = 1 & n_r > 0max(n_r) - t; \end{cases} \tag{3.1}$$

where n is the current pixel, t is a specified ringlight threshold and r is the current row. Rows corresponding to the high intensities of the ring light are consequently removed.

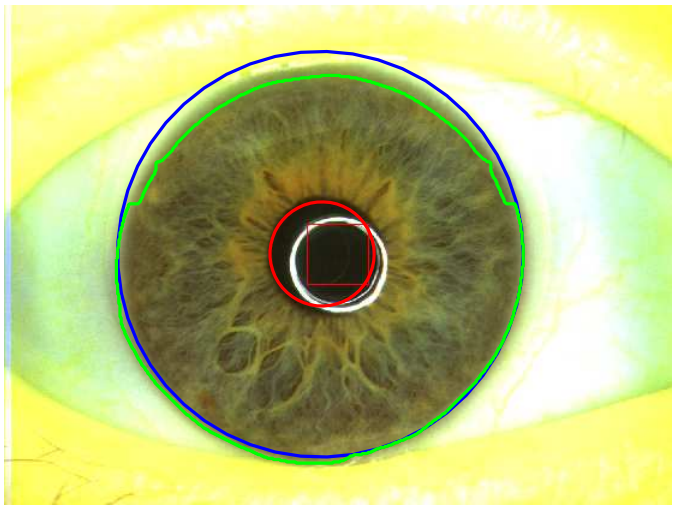

Figure 3.1: Original CIR Segmented image.

(a) CIR image of the normalized iris (b) Normalized mask

Figure 3.2: Normalized iris CIR texture and normalized mask.

The result of the ring light removal process across the four channels is shown in Figure 3.3. Once the ring light is removed, the image is reduced into a 1 dimensional signal. To facilitate this, *apriori* knowledge of the iris structure is needed. Typically, the iris structure, traversing from the pupil to the limbic boundary, is similar in composition. The pupillary section of the iris is thin and discloses the heavily pigmented posterior layer 3.4, and thus a darker intensity. While

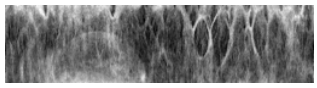

(a) IR channel

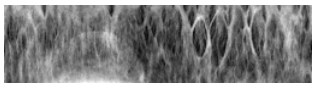

(b) Red channel

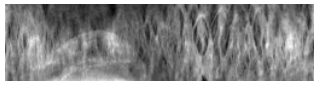

(a) Green channel

(b) Blue channel

Figure 3.3: Normalized iris channels with the ring light removed.

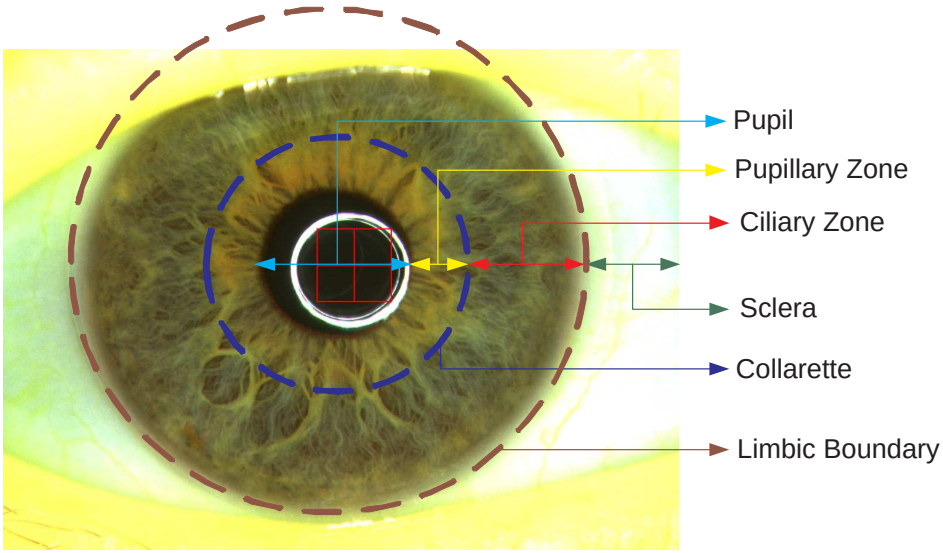

Figure 3.4: Sectional anterior anatomy traversing radially across a green/hazil colored iris.

the ciliary region contains contraction furrows, striations, and less melanin. The collarette is a concentric circle of the iris and is typically the thickest part, containing the same composition. So, concentrically the collarette displays a constant intensity or reflectance. Hence, the pixels in a single channel corresponding to concentric circles have very similar intensities. To prove this the mean and variance of the concentric rings shown in Figure 3.5 are computed. The variance

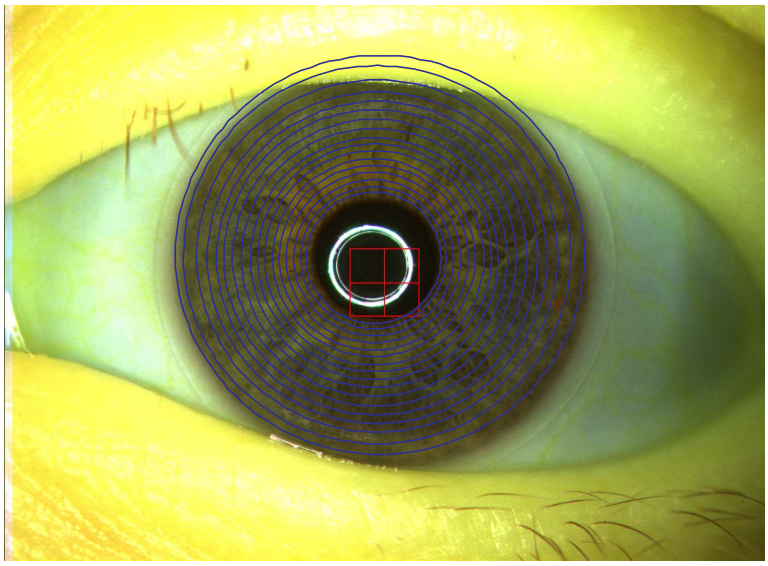

Figure 3.5: Concentric rings of an iris.

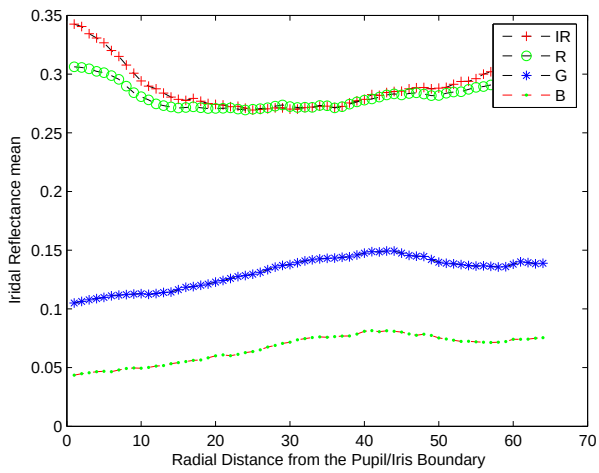

Figure 3.6: Mean of concentric rings of an iris.

(Figure 3.7) of the concentric circle for all channels is less than .016. While the mean (Figure 3.6)

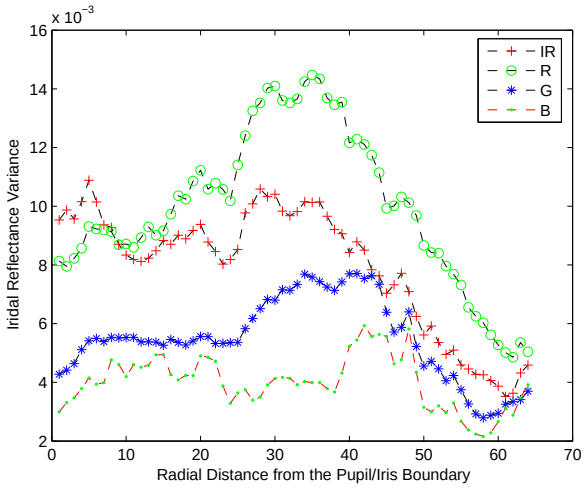

Figure 3.7: Variance of concentric rings of an iris.

of the 4 channels is below .35. The small variance value when compared to the mean indicates that the mean is a good estimate of the concentric circles of the iris.

In the unwrapped images (Figure 3.3) the concentric circles correspond to the rows of the iris. The unwrapped image in each channel is taken and the average of the pixel intensities along the rows(r) is computed in order to generate a 1-D signal, S.

$$S(i) = \frac{1}{N_{c(i)}} \sum_{j=1} I[r_i, c_j]$$

where S(i) is the average intensity in row i, $N_{c(i)}$ is the number of columns in row r_i, and $I[r_i, c_j]$ is the pixel intensities in row 'r' and column 'c'. Figure 3.8 shows the one dimensional reduction using the mean along the concentric circles of an unwrapped image. Since the 1-D representation is radial in nature it is unaffected by motions of the iris or head shifting unlike the textural 2-D matching. Therefore, no circular shifting has to be performed to analyze the feature vectors. Due to its radial extraction, it is pre-aligned according to the particular row. Also, note that the mean pixel intensity across the 4 channels are very diverse (for the green colored eye 3.1) when there is a very large difference in the wavelengths, e.g., in Figure 3.8 the IR and the R patterns are more similar in linear description than the IR and B channels, and the G and B channels are also similar. However, some eyes exhibit the same type of linear pattern across the four channels as in the blue iris in Figure 3.9 (four channels plotted in the same graph per eye image). The intensity can be directly used as a feature vector. However, the reflection will vary greatly with changes in lighting conditions. Figure 3.10 shows the radial intensity of a green/hazel iris across multiple

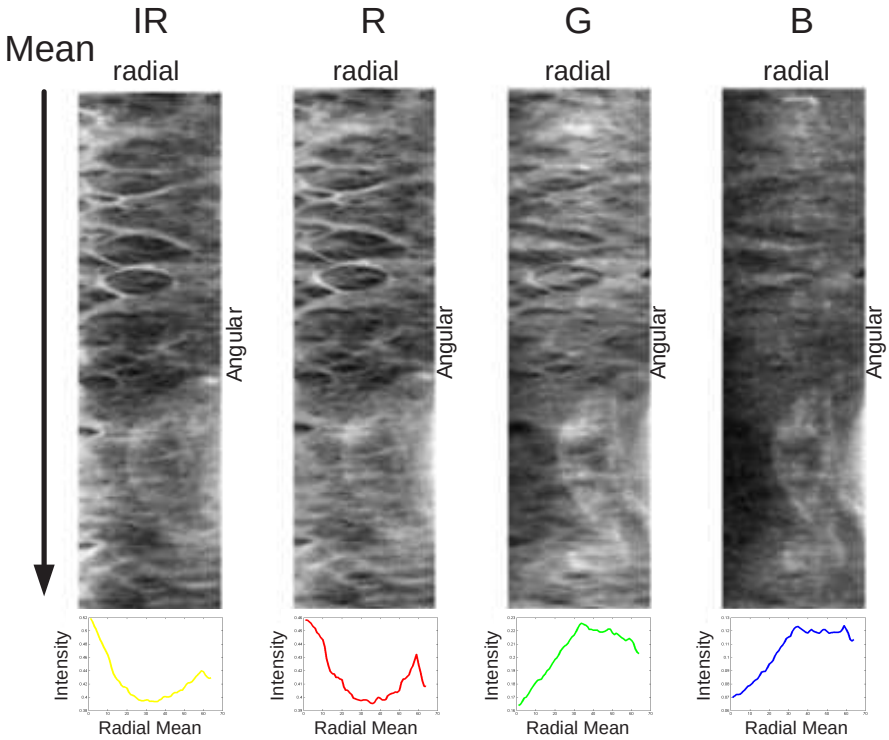

Figure 3.8: Unwrapped iris decomposition.

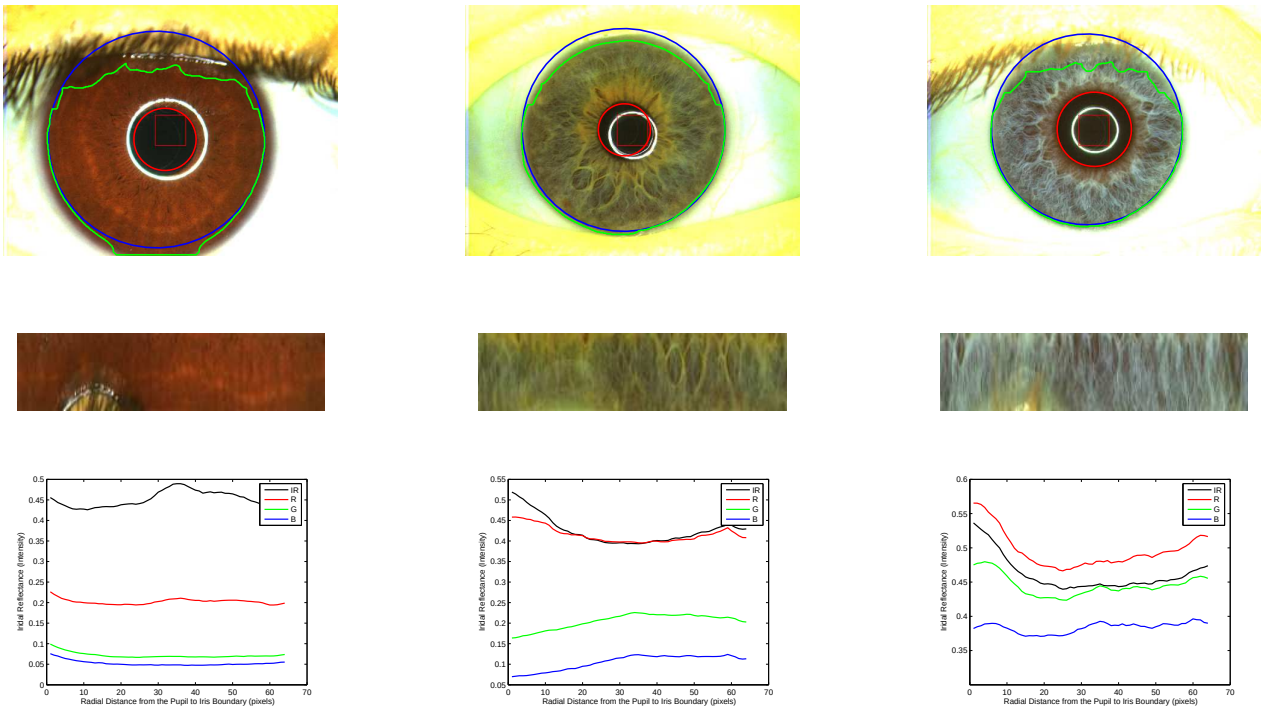

(a) Brown Eye (b) Greenish Hazel Eye (b) Blue Eye

Figure 3.9: Radial mean intensity plots across multiple channels of an iris image.

uniform illumination intensities, i.e., the iris was captured with the ringlight being supplied different power ratings or the ringlight was at the same intensity but at a different distance away from the iris. In Figure 3.10 the intensity of the illumination source was scaled from a current of 800mA down to a current of 700mA in steps of 100mA. From the figure it can be seen that the

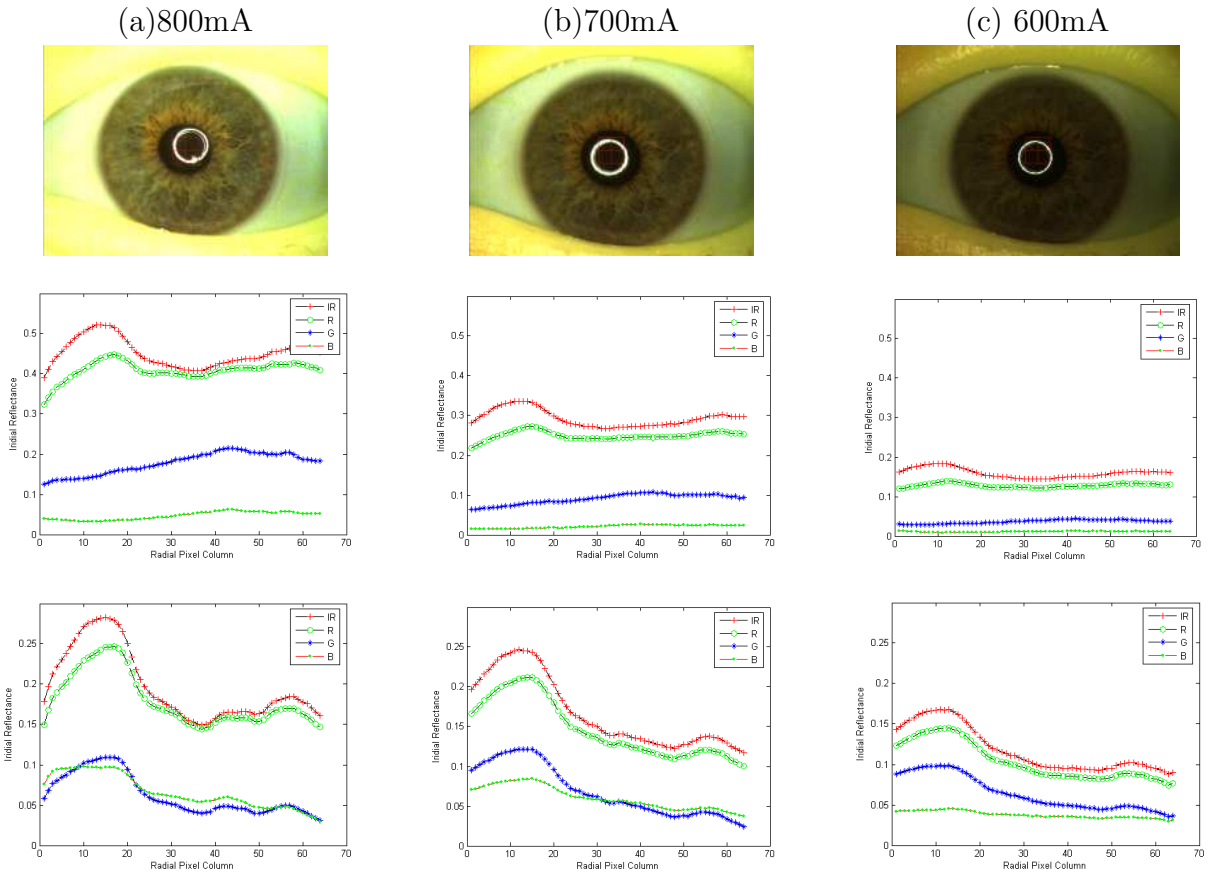

Figure 3.10: (row 1) Original iris image (row 2) radial mean intensity plots across multiple illumination intensities, and (row 3) La*b* adaptive histogram equalization .

radial intensities are sensitive to intensity changes. This results in inferior matching performance. However, pre-processing steps can be taken to normalize the image across varying illumination patterns. As an example the reflectance plot of a La*b* adaptive histogram equalization over the unwrapped iris block is shown in Figure 3.10 third row. The adaptive histogram equalization was performed in the CIE L*a*b* color space to enhance the structural components across the various spectral channels of the iris. In the L*a*b* space, the intensity values are represented by the L* parameter, the colors between green and magenta are represented by the a* parameter and the colors between blue and yellow by the b* parameter. Thus, histogram equalization can be performed on the L* component without affecting the original color of the image. This color

space is used to moderate the intensity values without perturbing the color components. The effect of this transformation, and the subsequent equalization, is the retention of the original color information, with certain iris components being emphasized in the individual spectral channels. In order to facilitate transformation from the original color space to L*a*b*, the following two mappings were examined: (a) the IR-R-G (false color or CIR) information was converted to the L*a*b* space; and (b) the R-G-B information was converted to the L*a*b* space. In both these cases, after histogram equalization, the information was converted back to the CIR/RGB space (Figure 3.11). Once converted back, the 1-D reflectance (Figure 3.10,

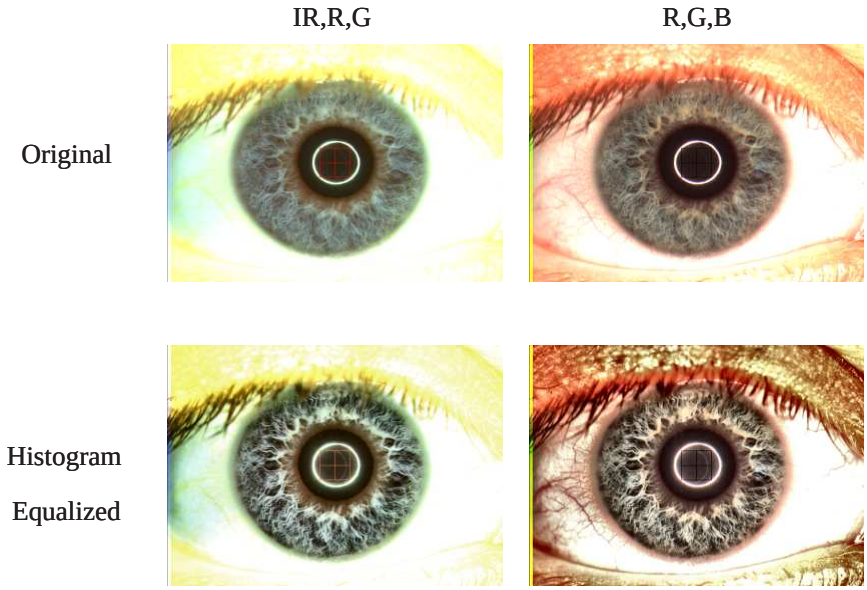

Figure 3.11: The CIR (IR-R-G) and RGB color images before (top) and after (bottom) L*a*b* color space image adaptive histogram equalization.

third row) has a more uniform shape with the curvature information being constant across the channels. Thus, through the La*b* equalization one-dimensional feature becomes more robust to intensity variations. However, the data set used had a constant illumination across all subjects, so no normalization was required.

Since a typical close range iris system has little illumination variations, the 1-D intensities suffer only slight perturbations. As the illumination and intensities vary over time due to slight eye movements or light fluctuations, the 1-D signal can fluctuate. However, the fluctuations are somewhat similar across the four channels. So, in order to extract a robust feature set, the distances between the radial patterns are taken as the feature vector. The distance between

the channels are more stable than the reflectance values alone. All possible combinations of the distances between the channels (viz., IR-R, IR-G, IR-B, R-G, R-B and G-B) are used to create a 6-dimensional feature vector. Figure 3.12 shows an example of three sample reflectance difference plots over time range of 100 frames captured at 7.5 frames per second.

3.2 Matching

Matching of the radial feature vectors is performed using the Euclidean distance. Each difference signal is represented as a feature vector in the the form $S = (s_1, s_2, ..., s_n)$. Two feature $S1 = (s1_1, s1_2, ..., s1_n)$ and $S2 = (s2_1, s2_2, ..., s2_n)$ vectors are compared using the Euclidean distance (D),

$$D = \sqrt{\sum_{i=1}^{n} (s1_i - s2_i)} \tag{3.2}$$

where s1 and s2 are the two different difference signals and n is the number of rows in the unwrapped iris image. The distance score gives a good indication if the 6-D feature corresponds to the same iris.

The data-set contains 35 subjects with 5 samples per subject. Each signal is matched by computing the Euclidean distance of all the signal channel combinations. Since radially, the left and the right iris are similar in color and, therefore, similar in reflection, the left and right eye of each subject is observed to be very similar unlike in a texture based system. The receiver operating characteristic (ROC) in Figure 3.16 shows the matching performance when each subject's left eye is matched with the right. The fused result of all the channels (using the sum score fusion described below) result gives a 45% genuine accept rate (GAR) at a false accept rate (FAR) of .1%. This high value indicates that their is some similarity in the features. To further detect similarity a correlation of the genuine scores is computed between left and the right eye 3.1. The correlations indicates that the genuine scores are slightly correlated and the imposter scores are highly correlated. Thus, the 1-D intensity feature vectors cannot be matched independently.

To evaluate the irides at different resolutions the images were downsampled in size to scales of 60, 40, 25, 20, 10, and 5 percent of the original size resulting in image sizes of 624x835, 520x696, 260x348, 208x278, 104x139 and 52x69, respectively. Figure 3.15 shows the matching result of the downsampled images for both the left and right eyes.

Each feature vector alone does not achieve very high recognition performance. However, the

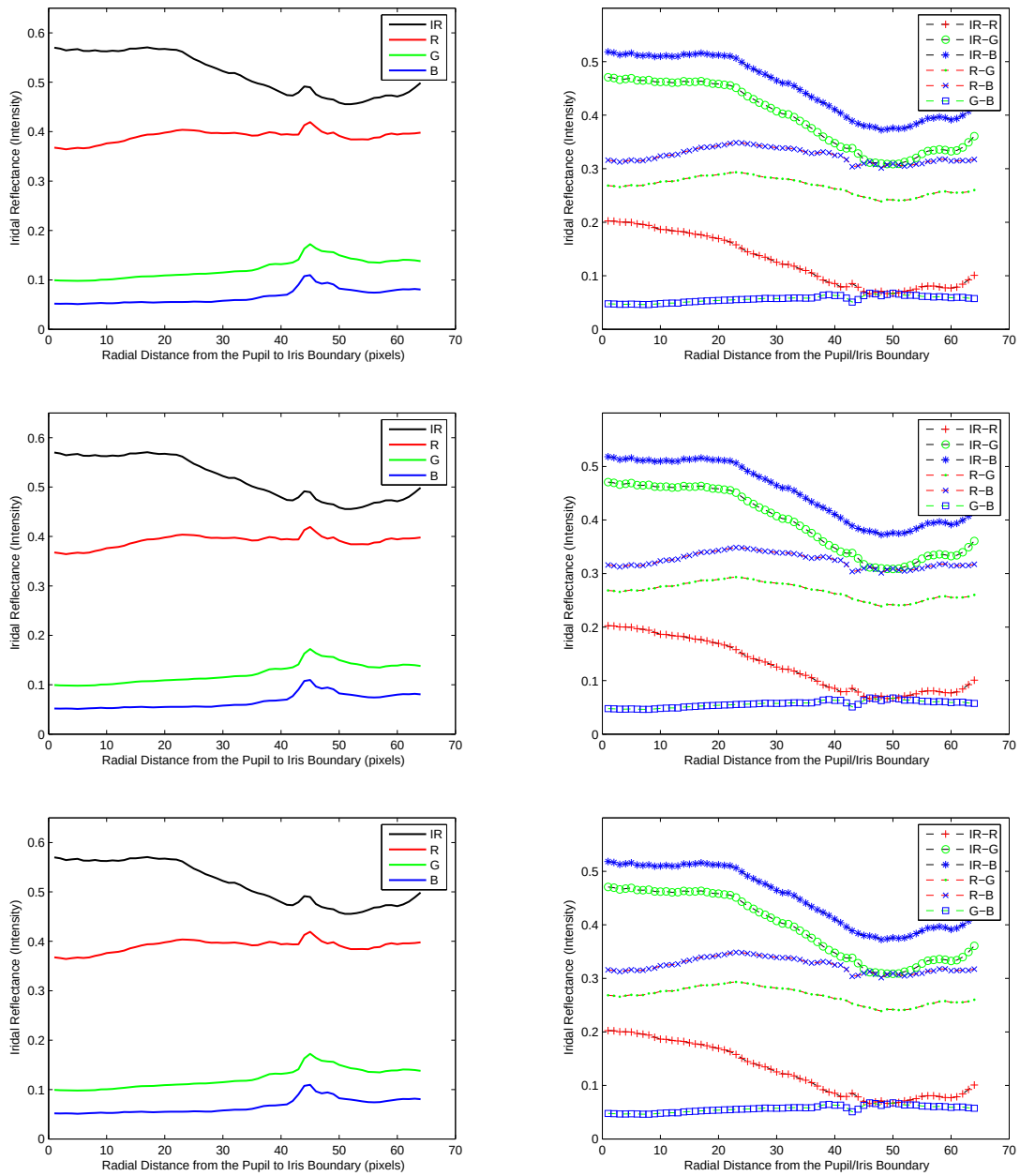

Figure 3.12: 6-D feature vector (column 2) created from all the combinations of the difference of the radial reflectance (column 1) across time.

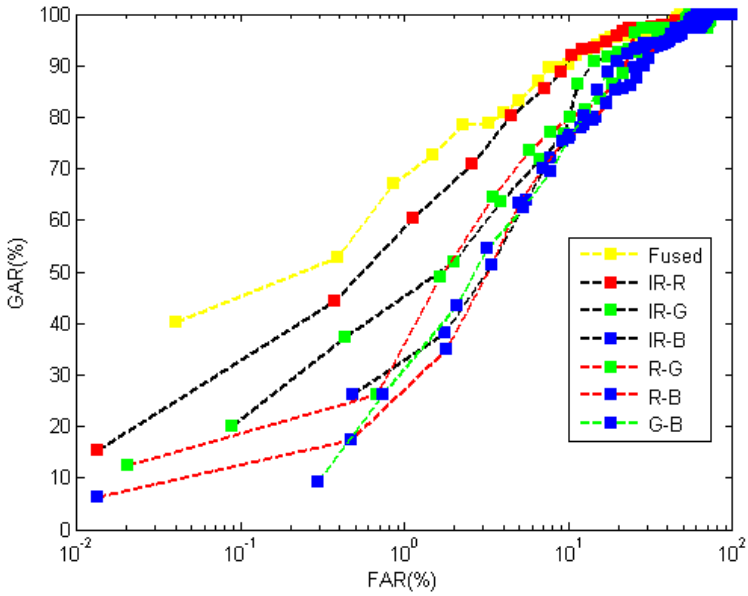

Figure 3.13: Subject's left eye matched with their right eye.

Left Vs. Right	Genuine Correlation	Imposter Correlation
Fused	.11	.89
IR-R	.22	.95
IR-G	.12	.90
IR-B	.10	.86
R-G	.18	.87
R-B	.12	.84
G-B	.35	.83

Table 3.1: Genuine and imposters scores correlations between the left and right iris of the 1-D intensity based matching.

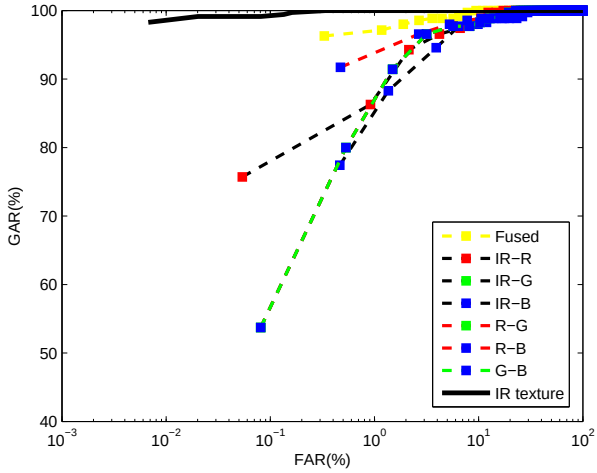

60% downsampled right eye ROC

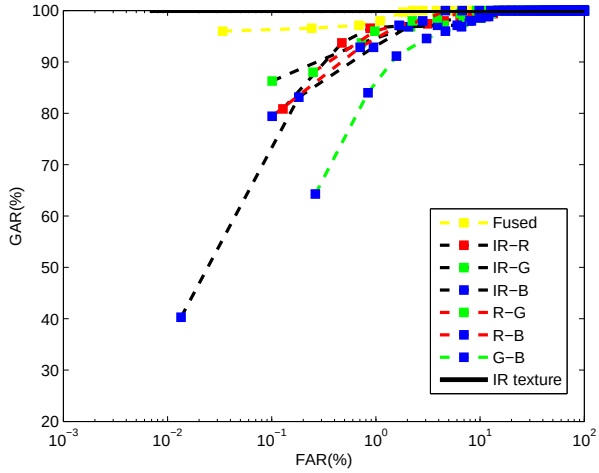

60% downsampled left eye ROC

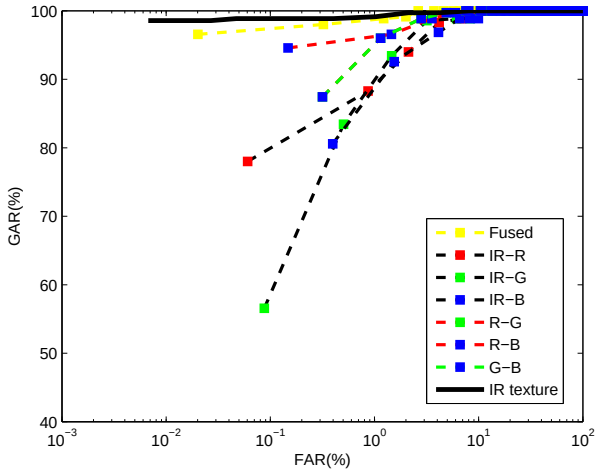

40% downsampled right eye ROC

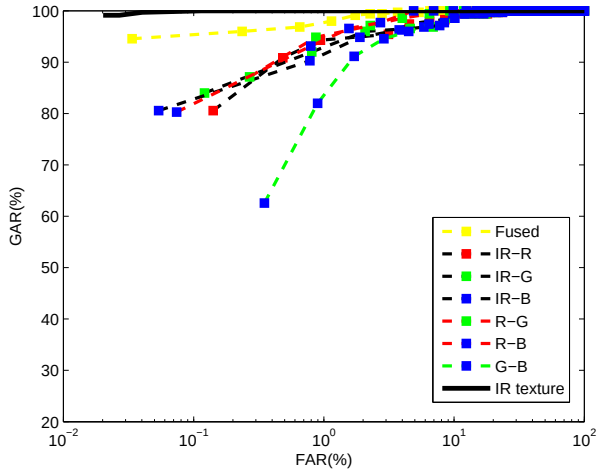

40% downsampled left eye ROC

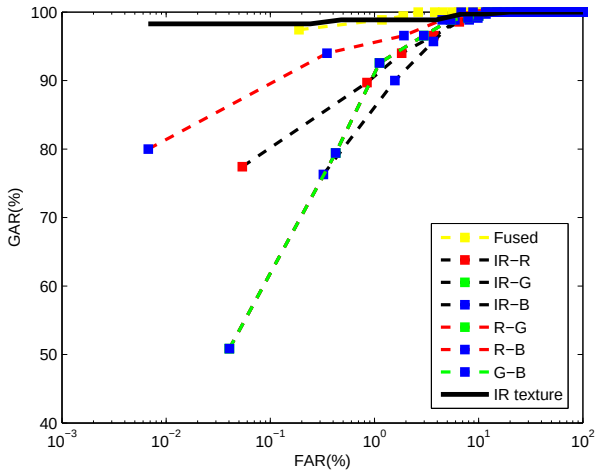

25% downsampled right eye ROC

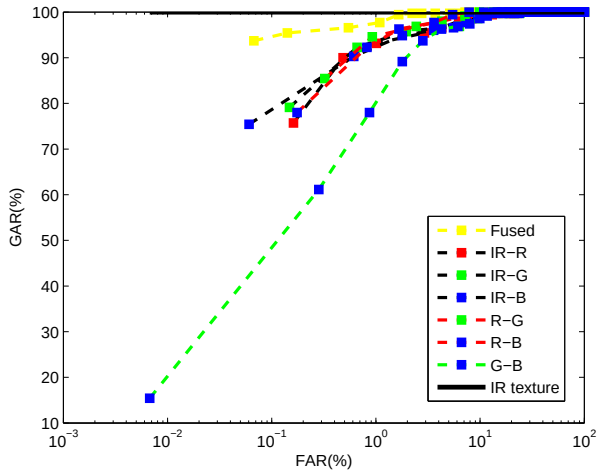

25% downsampled left eye ROC

Figure 3.14: ROC curves of downsampled iris images.

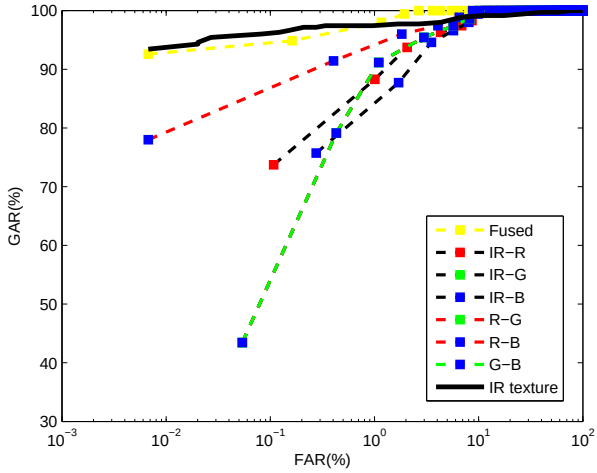

20% downsampled right eye ROC

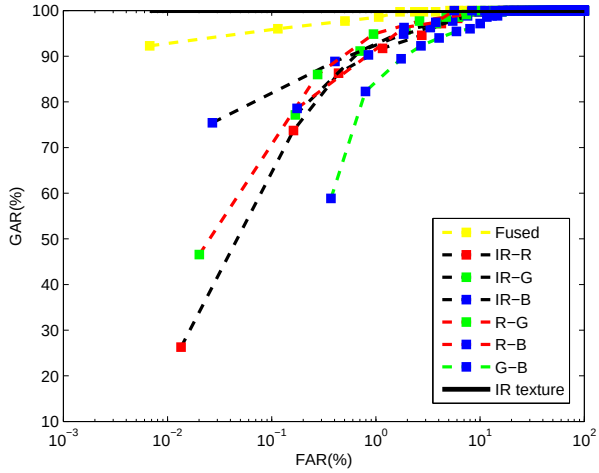

20% downsampled left eye ROC

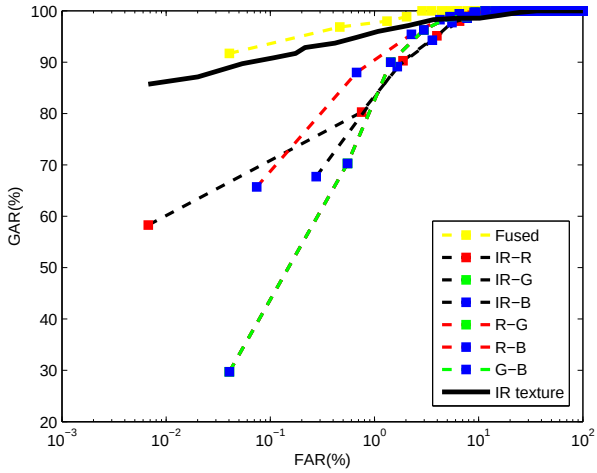

10% downsampled right eye ROC

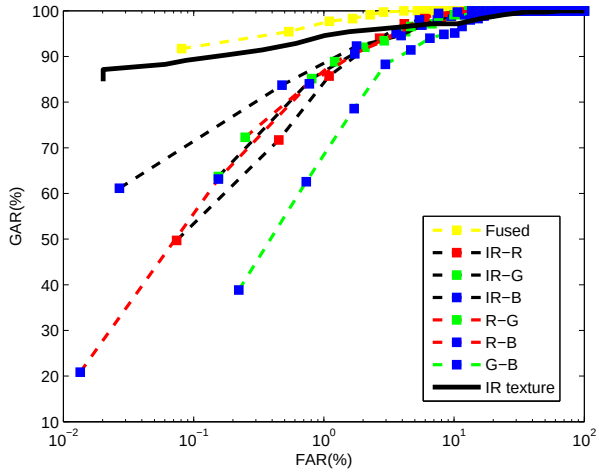

10% downsampled left eye ROC

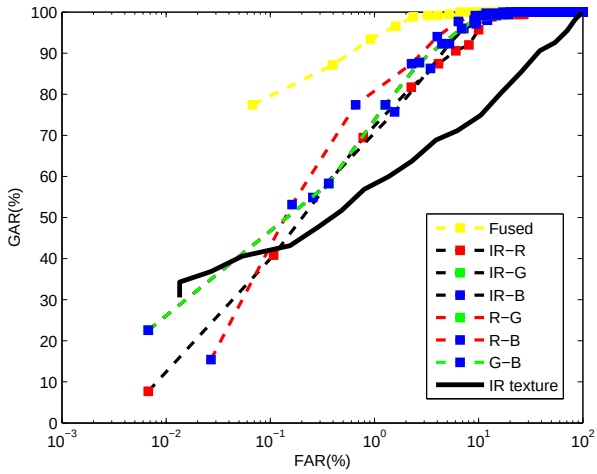

5% downsampled right eye ROC

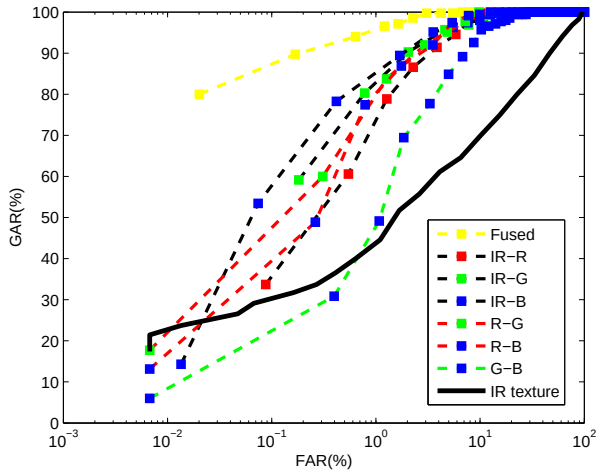

5% downsampled left eye ROC

Figure 3.15: ROC curves of downsampled iris images.

Image Sampling	Image Size	1-D EER	1-D d-prime	T EER	T d-prime
60%	624x835	1.09	2.84	0	7.27
40%	416x556	1.14	2.84	.11	7.18
25%	260x278	1.6	2.83	0	6.86
20%	208x278	1.06	2.83	0	6.86
10%	104x139	1.66	2.83	4.3	3.14
5%	52x69	2.26	2.83	22.69	1.22

Table 3.2: Feature matching comparisons: 1-D intensity (1-D) Vs. Texture (T).

result of fusing the scores of each feature vector using the sum rule gives an average score based on the 6-D feature vector that results in a very high performance. This improved performance comes from the fact that the sum rule is more effective than the product rule when the input tends to be noisy [43]. Thus the rule helps to account for slight variations in intensities that are associated with noise. The sum rule for the genuine and imposter scores is simply the average of the six match scores, i.e.,

$$Score = \frac{(D_{IR-R}) + (D_{IR-G}) + (D_{IR-B}) + (D_{R-G}) + (D_{R-B}) + (D_{G-B})}{6} \tag{3.3}$$

where D is the Euclidean distance of each feature vector. This fused score is taken as the eventual output score of the multispectral recognition system.

A comparison between the left eye matching comparing the performance of the 1D intensity based scheme against the texture based approach can be seen in Table 3.2 and Figure . The equal error rate (EER) and d-prime values are used to compare the two curves. The EER specifies the intersection of the False Accept rate and false reject rate (FAR=FRR), that gives an overall performance of the matching. Whereas the d-prime value gives an indication of how well the non-match score probability density and the match score probability density are separated based on the mean and variance (μ_m, σ_m) of the match scores of genuine users and the mean and the variance of the non-match (imposters) scores (μ_n, σ_n) [44] as in

$$d' = \frac{\mu_m - \mu_n}{\sqrt{(\sigma_m + \sigma_n)}} \tag{3.4}$$

To further evaluate the 1-D intensity based matching scheme against the texture based scheme a correlation of the scores is computed in order to determine score similarity. Table 3.3 displays the genuine and imposter score correlation between the fused 1-D intensity based matching and the texture based matching. The genuine score correlation computation results in a high

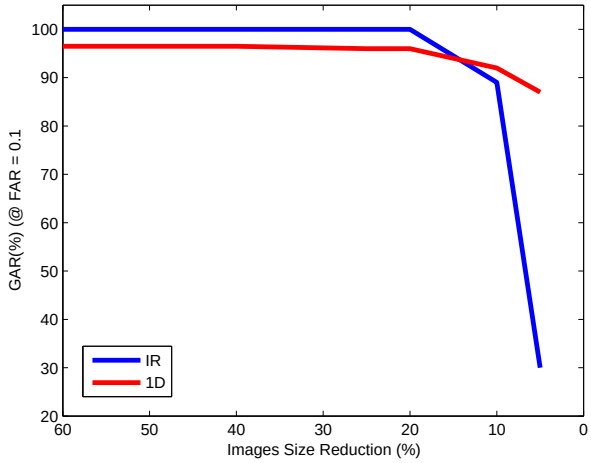

Figure 3.16: The IR and 1-D schemes genuine accept rate (GAR) versus image sizes at a false accept rate (FAR) of 0.1.

1-D Vs. Texture	Genuine Correlation	Imposter Correlation
Fused-IR	.47	-.01
Fused-R	.50	.0009
Fused-G	.45	-.0009
Fused-B	.31	.0960

Table 3.3: Genuine and imposters scores correlations between the 1-D intensity based and texture based matchings.

correlation score. This indicates that genuine score results are comparable to the texture based results. While the imposter score correlation results in almost no correlation. The zero correlation of the imposter scores indicates that the spread and distributions of the imposter scores are not similar whatsoever.

3.3 Summary

A scheme was proposed that fuses multispectral information based on the intensity of the radial concentric circles in the segmented iris. The scheme summarizes the intensity information in concentric circles - by using the mean intensity of each radial circle - thereby reducing it to a 1 dimensional feature vector. The difference between two such vectors corresponding to a pair of spectral channels is used as a feature vector. Thus, each iris image was represented by a collection of such vectors pertaining to multiple channel pairs (i.e., IR-R, IR-G, IR-B, R-G, R-B, G-B). The

fusion technique relies on the match scores generated as a result of comparing the corresponding feature vectors between two images of the iris. Since the left and the right eye exhibit similar chromaticity, they appeared to be correlated based on the proposed representation scheme. The matching performance using the 1D intensity based feature sets was observed to be comparable to that of a texture-based techniques using Gabor filters. However, the matching performance of the texture-based method degraded rapidly as the size of the eye image was reduced unlike the 1D intensity based method. Thus, an integration of the intensity-based and texture-based scheme can lead to a very robust matching scheme. The intensity scheme is susceptible to fluctuations in illumination. So, a normalization in the L*a*b* color space was used to enhance and normalize the iris structure. Alternate color spaces could have been used to perform this normalization that might facilitate the normalization and enhancement process.

Chapter 4

Anti-spoofing Techniques

Various types of attacks can be used to fool or spoof an iris recognition systems. Technologies are emerging that can better replicate the intricate chaotic pattern of the iris. Thus, counter measures are needed to circumvent these possible attacks. Liveness detection, the act of determining vitality, has become the focus of detecting these biometric spoofs. It is apparent that for different attacks, different countermeasures need to be taken [45]. These counter measures to detect liveness traditionally in biometrics can come in the form of hardware (different sensors) and software [46]. This chapter explores software based techniques that can be used to exploit information from channels of a multispectral image in order to detect spoof attacks using pictures, video, printed contacts and prosthetic eyes .

4.1 Spoofing Attacks

4.1.1 Picture

Perhaps the easiest and most effective spoof is the reproduction of the iris via the digital photograph [47]. A digital still image of an iris is taken and reproduced by printing an image on a material. Most photographs are replicated by printing only in the visible RGB wavelengths using ink compounds to form the image on a white paper background. The inks can come in a variety of types (black, process black, UV, etc.) as well as the paper (matt, glossy, etc.). Once printed, the static image is then presented to the iris capture device. Certain ink compounds can be used to replicate the reflection from the color wavelengths of the iris' structure.

Using a high resolution 700dpi color printer and a multispectral camera, a green colored iris

was reproduced as in Figure 4.1 using colored ink.

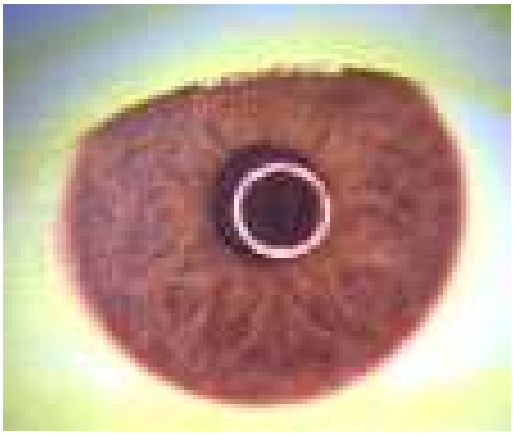

Figure 4.1: Iris spoof image with initial settings of a live eye

Figure 4.2: Iris spoof image with illumination set to the iris image

Using the imaging conditions for a live iris, a digital still image of a green iris is captured, Figure (4.1). Also, a worst case scenario in which the camera is set to detect the image of the iris is captured as in Figure (4.2). Each image is scaled to the appropriate iris size when printed. The images are then presented to the iris system. The images are matched against the original digital images in order to establish possible verification. Due to the resolution restraints of the printer and the high resolution of the camera channels the image pixels are easily seen in the image. Therefore, a matching of the image was not possible with current resolution printers. However, as printers become higher resolution it is very feasible to spoof an iris system using a photograph. Thus, there is still a need for a liveness detection measure to circumvent photograph spoofs.

The easiest and most effective form of liveness detection for the printed photograph is pupil motion detection. Since the pupil of the photograph is static a time series capture indicates that there is no movement. A real iris can potentially have a profound dilation and constriction. Figure 4.3 shows the extremes of the dilation and constriction effects by shining visible light on the eye (constriction) and using a drug to trigger the eye muscles (dilation). Also, in a live iris

Figure 4.3: Iris spoof image with illumination set to the iris image

the pupil is always oscillating (known as hippus) at .5 hertz or every half a second, dependent on the individual. Thus if the pupil is located and tracked over time it is a good indication of liveness. Figure 4.4 shows a video sequence of an iris sampled every 10 frames from a 100 frame sequence (7.5fps). The plot in Figure 4.5 is the radius being tracked across a total of 100 frames of the video sequence. Hippus can be seen in the radius tracking plot by the oscillation of the radius line as time progresses. Also, notice that as the subject blinks the radius of the pupil goes to zero indicating that the pupil is no longer present as the eyelid closes. The blinking can be used in conjunction with the pupil tracking to detect liveness. While the eyelid is closed the light receptors in the eye are not receiving a signal of light being present. Thus, when the eye opens it is slightly dilated as can be seen by the radius peak after the eyelid closing in Figure 4.6. This seems also to be dependent on the length of time that the eye is closed, a very fast blink doesn't alow the receptors to respond and the eye does not dilate. This can be seen in the double blink in Figure 4.6. Once the eye is opened and receptors receive a signal of light being present, the pupil then constricts (shown by the dip after the dilation peak). After the dip the pupil settles back to its original stable ambient light condition.

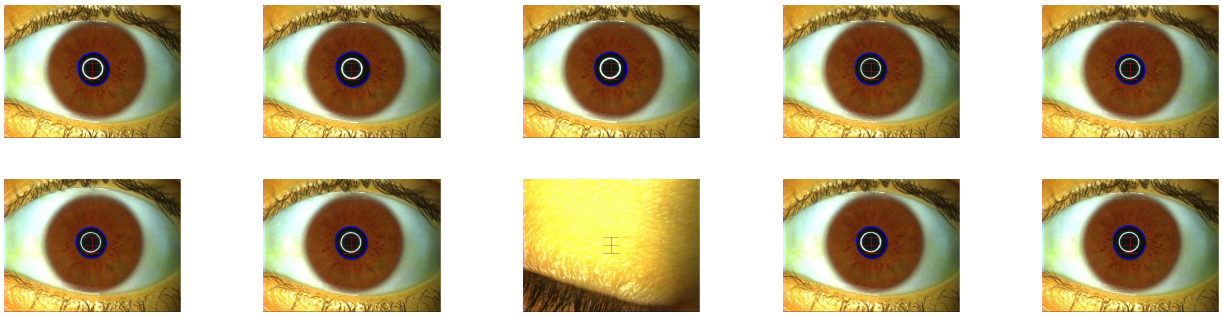

Figure 4.4: Video pupil tracking sequence sampled every 10 frames

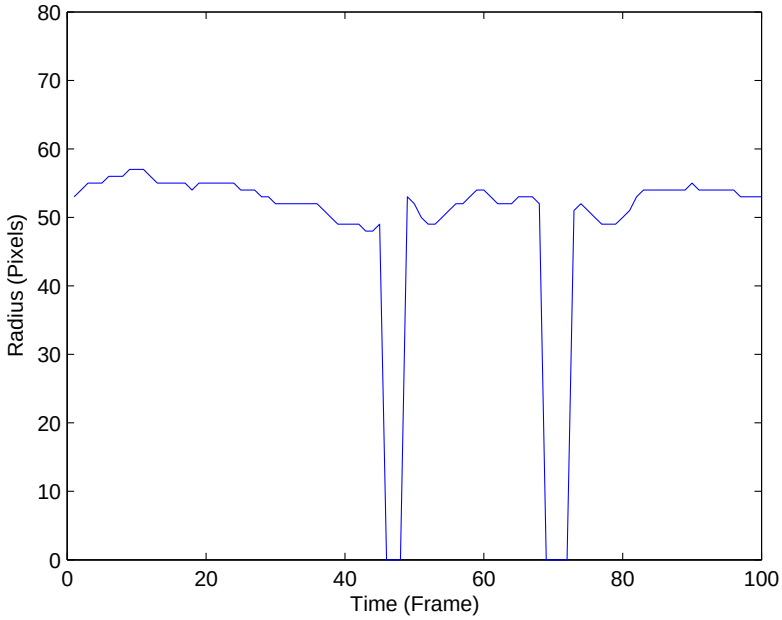

Figure 4.5: Radius tracking across 100 frames

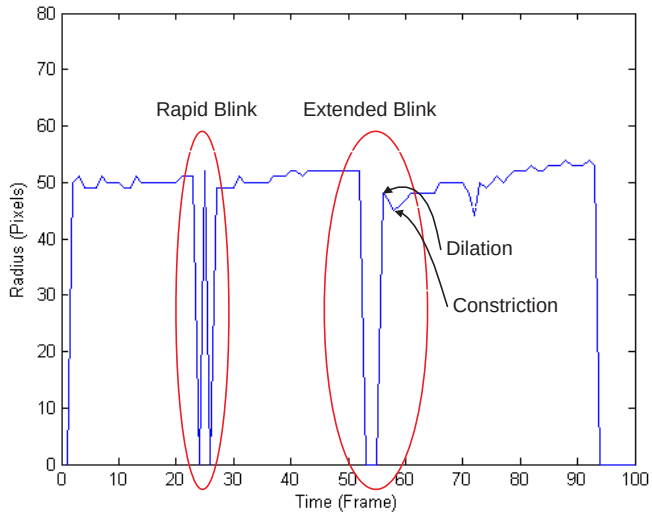

Figure 4.6: Radius tracking across 100 frames with a double blink

4.1.2 Video Replay

The video replay attack is executed by capturing a digital video sequence of an user's iris. The video is then replayed to the digital iris capture device in order to recreate the actual physiological mechanisms (dilation, constriction, hippus) of the iris. The video can be presented on any device, (LCD, CRT, Gas-plasma, LED, etc) which replicates the color and intensity of the actual iris.

Using a RGB video sequence of a green iris acquired with a multispectral camera an attack is performed on the iris system. Each video is replayed to an iris camera using an LCD screen and a CRT monitor. The images are selected from the video sequence and matched against the original captured video images in order to establish possible verification.

LCD and CRT screens operate only in the visible spectrum, matched to the human eye, with little or no IR radiation as can be seen in Figure 4.7. Thus, currently available screens are not perceived by current iris recognition systems that detected only IR light. However, a screen could be constructed to only emit an IR video stream or emit an IR video stream along with the other visible range wavelengths. So, the detection of the spoof still needs to theorized.

A screen is composed of pixels that typical alternate red, green, and blue pixels. An image displayed on the screen is a composite image formed by varying these RGB pixels intensities. Thus, in multiple wavelengths these pixel separations can be detected as in the channel images

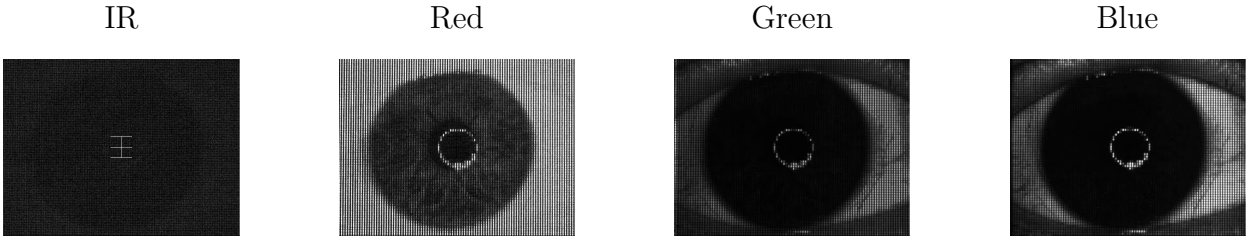

Figure 4.7: Iris spoof video channel images

(R,G,B) in Figure 4.7. Using the 2D Fourier power spectrum the periodic nature of the image can be detected. Figure 4.8 shows the power spectrum of the 4 channels and the subsequent decomposition of the channels by taken the mean of each column. This results in an image with 5 detectable peaks that can be used as a liveness detection measure. When compared to the

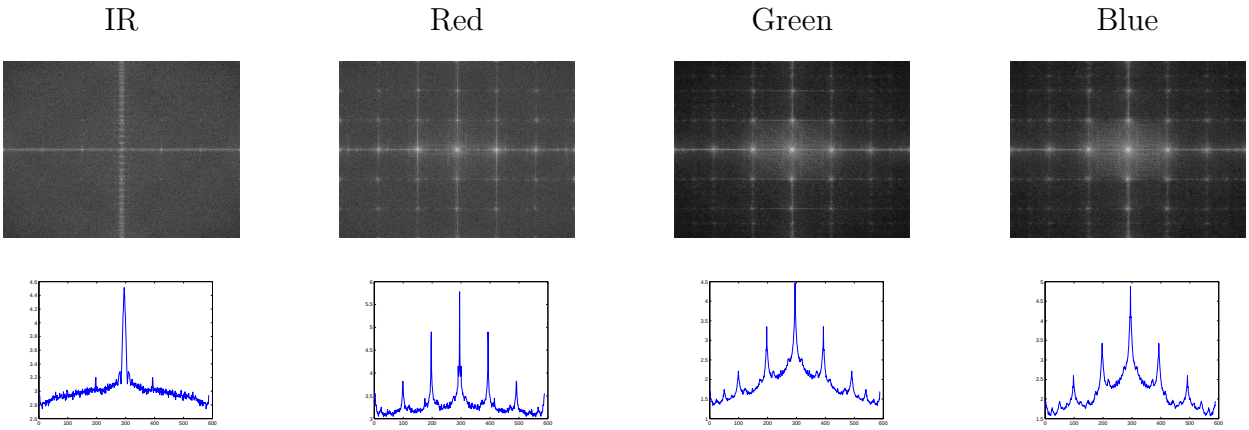

Figure 4.8: 2D Fourier Power Spectrum of an iris video and its decomposed signal

power spectrum of a real iris, as in Figure 4.9, the periodic peaks are not detected.

4.1.3 Printed Contact Lens

The hardest spoof to detect by a iris recognition system that has a guard (an actual person) standing watch is a printed contact lens. Unless very close to the face of the subject the printed contact is undetectable. The concept behind the printed contact is that digital image of an enrolled user is captured and printed or painted onto a colored lens surface that is placed in front of the eye concealing most of the iris pattern and/or changing the color of the wearer's eye. Most over the counter printed contacts function to change the appearance of the wearers

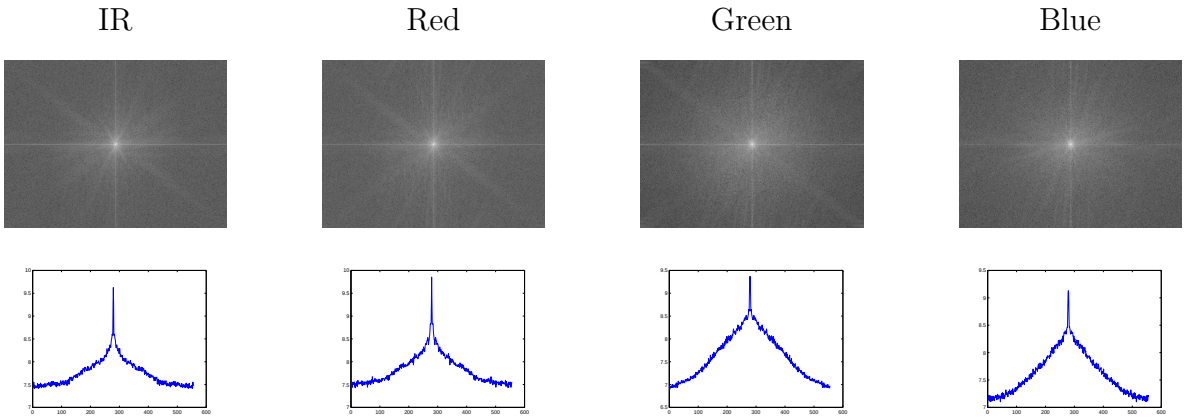

Figure 4.9: 2D Fourier Power Spectrum of a real iris and its decomposed signal

eyes. Clear contacts come in two main types: soft contacts and rigid gas permeable. Soft contact lenses are made from oxygen permeable, water-loving plastics that actually become pliable during manufacturing. Soft contact lenses contain between 30 and 80 per-cent water, depending on the type of lens. Rigid gas permeable (RGP) lenses combine some of the properties of both hard and soft lenses. Made of special firmer plastics, which are permeable to oxygen, these lenses are very durable and usually have a longer life span than soft lenses. Colored contact lens come in a variety of categories and types. The main types consist of opaque, enhancement tints, visibility tints, light filtering tints,and Theatrical. Opaque lenses can dramatically change the natural color of your eyes regardless of how dark your eyes color is. It has a solid colored 'ring' that covers the iris while leaving a clear hole in the center to let the light passes through. The majority of colored contact lenses are opaque lenses. Enhancement tints lenses are translucent and are used to enhance your natural eye color (therefore, it also known as enhancer tints). If your natural eye color is dark color, enhancement tints lenses will be hard to make the color change visible. Therefore, enhancement tints lenses are recommended for light colored eyes only. Visibility tints do not change the eye color at all. It is slighted tinted for handling purpose so that you can remove and insert the lenses better. Also, it helps to find your contact lenses more easily if they are dropped or misplaced. Light filtering tints are the latest development in colored contact lenses. It is designed to be used in sports and outdoor recreation. Light filtering tints can enhance certain colors while muting other colors. As a result, it is easier to target the balls that stands out against the background. For example, tennis players wearing light yellow or gold tint colored contact lenses would track the ball more easily by brightening the background. Theatrical

contact lenses are a type of cosmetic contact lens that are used primarily in the entertainment industry to make the eye appear unusual or unnatural in appearance. These contacts completely alter the appearance of the iris. They can also be specially painted with a replicated iris pattern in order to conceal iris problems and disease.

The highest risk attack would come from an exact reproduction of the enrolled users iris pattern printed on the opaque lens in the theatrical sense, covering the entire spoofer's iris pattern. The detection of contacts is the focus of many liveness detection applications. Daugman proposed using the 2-D fourier spectrum to detect the frequency nature of the uniform printed contact[45]. While this works for the detection of enhancement contacts printed uniformly by machines it does not account for hand painted iris structure or a machine that could replicate a iris onto a contact from a digital photograph. Even after detecting the printed contact the detection could be used to exclude a potential target from a watch list by altering the users iris structure, rending the iris system ineffective.

A green iris was reproduced by a theatrical painted opaque contact lens.

4.1.4 Artificial Eye

An ocular prosthetic or artificial eye replaces a missing natural eye following an enucleation or evisceration. The ocular prosthetic typically takes the shape of a convex shell. The prosthetic fits over an orbital implant and under the eyelids. Most ocular prosthetics today are made of plastic through a process known as *casting* [48]. The actual iris of the artificial eye is known as a button and is cut from a thin cylindrical clear plastic rod on a lathe. The iris and pupil is then hand painted on the back (flat side) of the button and then seen through the opposite clear dome end of the button that mimics the cornea of the eye. A white plastic shell is then molded to the outside of the button in order to replicate the sclera, and vein structures are painted onto the white plastic. This shell fits the actual eye prosthetic that is molded to fit the inside of the eye socket.

Three different handpainted iris's where acquired through doctor Walter Tillman of West Virginia University's Eye Institute. The irises did not match any iris current enrolled in the dataset, therefore, a comparison could not be made. But a check for liveness can still be performed. Since the prosthetic is static being composed of dense plastic, a check for pupillary motion can be performed. Also, when Imaging the eye the shape of the iris button causes the reflections to

be vastly different from a natural iris. However, now subjects in that data set matched eye, so the reflection could not be validated, but a test for pupil motion can be performed and Figure 4.10 pupil radius tracking indicates that the radius does not change.

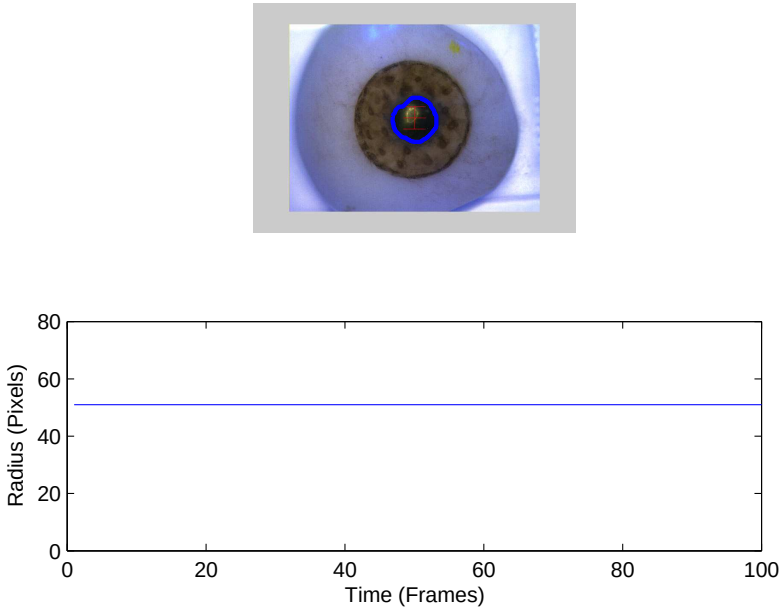

Figure 4.10: Pupil tracking of a prosthetic eye.

4.2 Summary

Attacks on a multispectral iris recognition systems were executed in order to spoof the system using a printed photograph, a video replay, a printed contact, and an prosthetic eye. Each techniques was imaged with a multispectral camera and spoof detection techniques were evaluated. Due to the high resolution of the camera and the low resolution of the printed, painted, replayed or fabricated artifact, it is difficult to match the spoofs against a living iris. However, with enhanced fabrication technologies, spoofing the iris will ultimately become more feasible. Thus, techniques to detect the spoofs are inevitable. Most of the spoofs attacks can be detected by a check for pupillary motion. By tracking the pupil over time, a spoof image, prosthetic and perhaps even a opaque contact can be detected. Also, the multispectral intensity of the iris can be used as measure to detect a real iris from a spoof.

Chapter 5

Summary and Future work

In this thesis, techniques to enhance the performance of iris recognition through the use of multispectral information was assessed. By eliciting information from multiple wavelengths channels, schemes for iris segmentation, feature extraction, and spoof detection were performed.

At the time of writing this thesis, no commercial iris recognition system acquires multispectral images of the eye. Due to this limitation, a multispectral acquisition setup was first designed in order to collect eye images from a few subjects. The data set comprised of 70 eyes pertaining to 35 subjects, with 5 image samples per eye. While this data set gives a good indication of performance the experiments designed in this thesis should be reproduced on data sets of much larger size to obtain a precise understanding of the performance. Also, in the IR channel the camera only analyzes a small portion of the near-infrared spectrum. A further exploration of hyperspectral imaging only in the IR region beyond 800nm should be assessed in order to explore the nature of iris structures that are revealed at various invisible IR wavelengths. A primitive setup to collect such type of data has been constructed as seen in Figure 5.1. The setup incorporates a radial series of light emitting diodes (LEDs) focused on the eye. The LEDs are placed in such a manner so that four corresponding LEDs contain the same wavelength. Thus, six different wavelengths are incorporated (5.1) with the peak intensities of IR wavelengths ranging from 700nm to 940nm (peak intensities 700nm, 760nm, 810nm, 850nm, 890nm, 940nm). Also, a cold mirror is employed as seen in Figure 5.2. The cold mirror serves a two fold purpose. 1) The reflection of the eye in the mirror can be used to align the eye with the camera for robust acquisition and 2)the mirror acts as a filter removing all ambient room light below 700nm as seen in the transmittance curve in Figure 5.2.

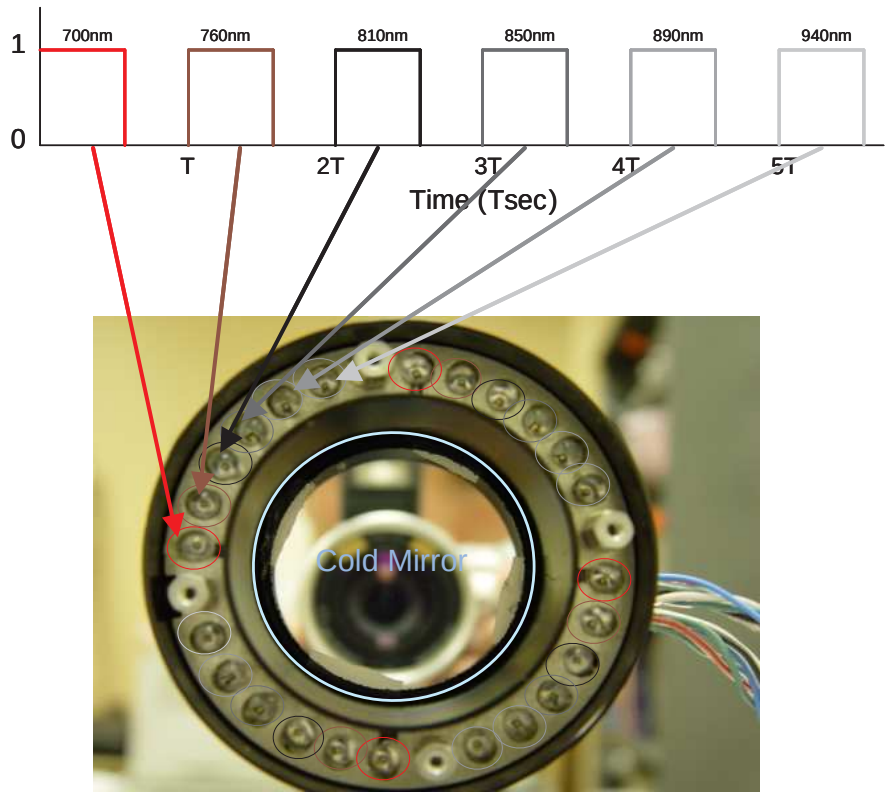

Figure 5.1: Setup to collect a sequence of iris images in the near infrared region (700-900nm) of the electromagnetic spectrum.

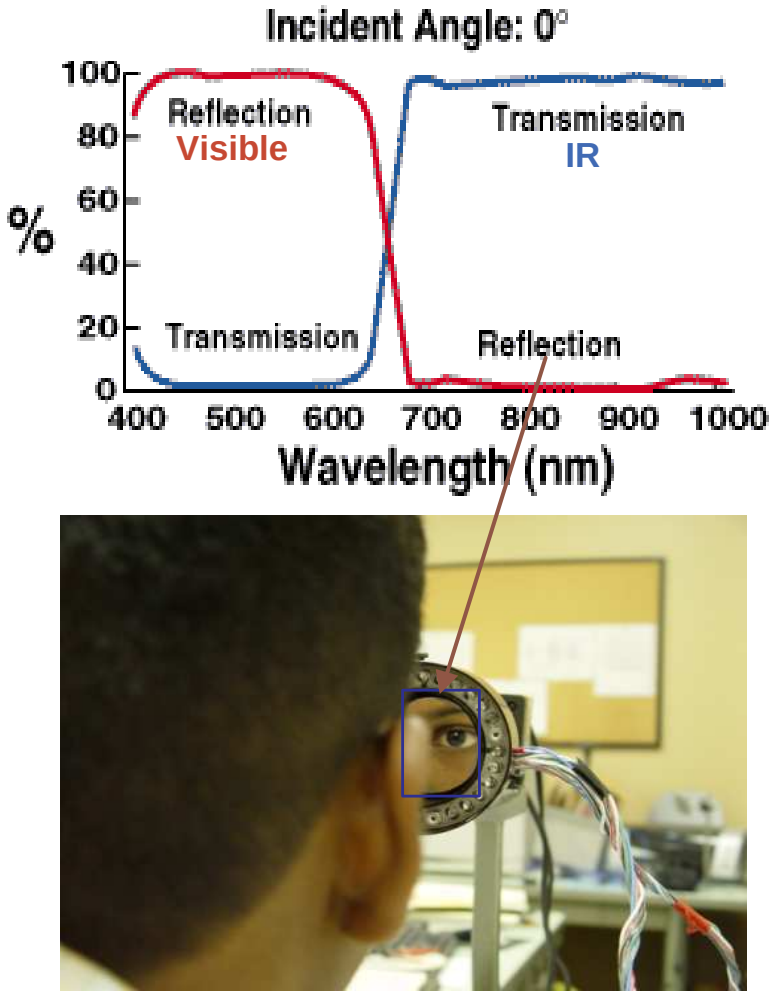

Figure 5.2: Eye focusing using a cold mirror filter.

The process of iris segmentation is a crucial part of an iris recognition system. Through the use of multiple channels (IR, R, G, and B) a classification scheme employing Bayesian probabilities was used to sperate the iris from other features of an iris image. The scheme is shown to have a very high performance. The Bayesian classification is shown to outperform both the segmentation based on only the IR channel and the color vector space-based segmentation of the multispectral image. Other multispectral schemes could be evaluated to enhance segmentation performance. A scheme employing color *texture*-based segmentation may be employed across the channels of a multispectral image.

An analysis of iris matching across multiple channels using a texture-based scheme shows that performance decreases as a function of the difference in wavelength between two images. This indicates that the nature of iris texture exposed varies with a change in the channel wavelength. Thus, certain iris features are accentuated in different wavelengths of light. A further exploration of techniques to combine these features could be performed in order to improve the performance of iris recognition systems. These texture variations could lead to user specific wavelengths based on the color of the eye.

The matching scheme of an iris recognition system ultimately determines recognition performance. In this thesis, a scheme was used that fuses multispectral information based on the intensity of the radial concentric circles of an iris. The proposed scheme first generates a 1 dimensional vector from these 2 dimensional concentric circles. The difference between two such vectors corresponding to a pair of channels was used as a feature vector. Thus, each iris image was represented by a collection of such vectors pertaining to multiple channel pairs (i.e., IR-R, IR-G, IR-B, R-G, R-B, G-B). The fusion technique relies on the match scores generated as a result of comparing the corresponding feature vectors between two images of the iris. Since the left and the right eye exhibit similar chromaticity, they appeared to be correlated based on the proposed representation scheme. The matching performance using the 1D intensity based feature sets was observed to be comparable to that of a texture-based techniques using Gabor filters. However, the matching performance of the texture-based method degraded rapidly as the size of the eye image was reduced unlike the 1D intensity based method. Thus, an integration of the intensity-based and texture-based scheme can lead to a very robust matching scheme. The intensity scheme is susceptible to fluctuations in illumination. So, a normalization in the L*a*b* color space was used to enhance and normalize the iris structure. Alternate color spaces

could have been used to perform this normalization that might facilitate the normalization and enhancement process.

The 1-D matching scheme is robust to image size, so it may be applicable to images of the face that are captured using a multispectral camera. Typically the iris extracted from images of a face have very low resolution and, therefore, very little texture. The multispectral intensity-based scheme could potentially be applied to these images to assess the matching performance. Other appearance based methods could also be explored to help improve the performance of multispectral iris recognition. Using the intensity based reflection technique the color of the eye can also be determined by setting specific thresholds which could aid in developing indexing schemes.

Like all biometric systems iris recognition systems are susceptible to attacks. In this thesis, attacks on a multispectral iris recognition system were effected in order to design appropriate countermeasures. The attacks involved spoofing the iris using a printed photograph, a video replay, a printed contact lens, and a prosthetic eye. Each spoof artifact was imaged with the multispectral camera and the spoof detection techniques were evaluated. The high resolution image acquired using the multispectral set-up made it difficult to match the low-resolution spoofs with a real iris. However, with enhanced fabrication technologies, spoofing the iris will ultimately become more feasible. Thus, techniques to detect the spoofs are inevitable. Most of the spoofs attacks can be detected by a check for pupillary motion. By tracking the pupil over time a spoof image, prosthetic and, perhaps, even a opaque contact can be detected. Also, the multispectral intensity of the iris can be used as a measure to distinguish a real iris from a spoof. Other measures of multispectral information such as texture variations across channels could be used to perform spoof detection.

Thus, there is plenty of potential in using multispectral information for iris recognition. In this thesis, we have demonstrated a few of these advantages. It is only a matter of time before the use of multispectral information in biometrics will become common-place.

References

[1] S. Nanavati, M. Thieme, and R. Nanavati, *Biometrics: Identity Verification in a Networked World*. New York, NY: John Wiley and Sons, Inc., 2002.

[2] J. Ashbourn, *Biometrics: Advanced Identity Verification*. Great Britian: Springer-Verlag London Limited, 2002.

[3] A. Jain, R. Bolle, and S. Pankanti, *Biometrics: Personal Identification in a Networked Society*. Kluwer Academic Publishers, 1999.

[4] D. Maltoni, D. Maio, A. K. Jain, and S. Prabhakar, *Handbook of fingerprint recognition*, 1st ed. New York, Berlin Heidelberg: Springer-Verlag, 2003.

[5] L. Flom and A. Safir, "Iris recognition system," U.S. Patent 4 641 349, February 03, 1987.

[6] J. Daugman, "High confidence visual recognition of persons by a test of statistical independence," *IEEE Transactions on Pattern Analysis and Machine Intelligence*, vol. 15, no. 11, pp. 1148–1161, 1993.

[7] J. G. Daugman, "Demodulation by complex-valued wavelets for stochastic pattern recognition," *International Journal of Wavelets, Multi-resolution and Information Processing*, vol. 1, no. 1, pp. 1–17, January 2003.

[8] R. P. Wildes, "Iris recognition: An emerging biometric technology," in *Proceedings of the IEEE*, vol. 85, no. 9, September 1997, pp. 1348–1363.

[9] W. Boles and B. Boashash, "A human identification technique using images of the iris and wavelet transform," *IEEE Transactions on Signal Processing*, vol. 46, no. 4, pp. 1185–1188, April 1998.

[10] L. Ma, Y. Wang, and T. Tan, "Iris recognition using circular symmetric filters," in *Proceedings of* 16th *International Conference on Pattern Recognition (ICPR)*, vol. 2, Quebec City, Canada, August 2002, pp. 805–808.

[11] S. Lim, K. Lee, O. Byeon, and T. Kim, "Efficient iris recognition through improvement of feature vector and classifier," *Journal of Electronics and Telecommunication Research Institute*, vol. 33, no. 2, pp. 61–70, June 2001.

[12] K. Bae, S. Noh, and J. Kim, "Iris feature extraction using independent component analysis," in *Proceedings* 4th *International Conference on Audio and Video Based Biometric Person Authentication (AVBPA)*, Guildford, UK, 2003, pp. 838–844.

[13] L. Ma, T. Tan, and Y. Wang, "Efficient iris recognition by characterizing key local variations," *IEEE Transactions on Image Processing*, vol. 13, no. 6, pp. 739–750, June 2004.

[14] J. Huang, L. Ma, Y. Wang, and T. Tan, "Iris model based on local orientation description," in *Proceedings of Asian Conference on Computer Vision*, Korea, April 2004, pp. 954–959.

[15] J. Huang, Y. Wang, T. Tan, and J. Cui, "A new iris segmentation method for recognition," in *Proceedings of the 17th International Conference on Pattern Recognition (ICPR)*, vol. 3, Cambridge, England, UK, August 2004, pp. 23–26.

[16] X. Yuan and P. Shi, "Iris feature extraction using 2D phase congruency," in *Third International Conference on Information Technology and Applications (ICITA)*, vol. 33, Sydney, Australia, July 2005, pp. 437–441.

[17] V. Dorairaj, N. A. Schmid, and G. Fahmy, "Performance evaluation of iris based recognition system implementing PCA and ICA encoding techniques," in *Proceedings of SPIE Conference on Biometric Technology for Human Identification III*, Orlando, FL, April 2005.

[18] J. Thornton, M. Savvides, and B. Vijaya Kumar, "Robust iris recognition using advanced correlation techniques," in *Second International Conference on Image Analysis and Recognition (ICIAR)*, vol. 3656. Toronto, Canada: Springer Berlin / Heidelberg, September 2005, pp. 1098–1105.

[19] A. Abhyankar and S. Schuckers, "Active shape models for effective iris segmentation," in *Proceedings of SPIE Conference on Biometric Technology for Human Identification III*, Orlando, FL, April 2006, p. 62020H.

[20] D. Socolinsky and L. Wolff, "A new visualization paradigm for multispectral imagery and data fusion." *IEEE Computer Society Conference on Computer Vision and Pattern Recognition (CVPR '99)*, vol. 1, pp. 319–324, 1999.

[21] R. Snell and M. Lemp, *Clinical Anatomy of the Eye.* Blackwell Science, 1998.

[22] S. Fan, C. Dyer, and L. Hubbard, "Quantification and correction of iris color," Technical Report 1495, 2003.

[23] P. Imesch, I. Wallow, and D. Albert, "The color of the human eye: A review of morphologic correlates and of some condition that affect iridial pigmentation," *Survey of Opthalmology*, vol. 41, no. 2, pp. S117–S123, February 1997.

[24] A. Wielgus and T. Sama, "Melanin in human irides of different color and age of donors." *Pigment Cell Res*, vol. 18, no. 6, pp. 454–464, Dec. 2005.

[25] ——, "Photogeneration of superoxide anion by iris of the human eye under in vitro conditions." *Current Topics in Biophysics*, vol. 26, no. 1, pp. 163–174, 2002.

[26] J. Daugman, "Biometric personal identification system based on iris analysis," U.S. Patent 5 291 560, March 01, 1994.

[27] R. B. Smith, "Introduciton to hyperspectral imaging," 2006.

[28] Z. Pan, G. Healey, M. Prasad, and B. Tromberg, "Face recognition in hyperspectral images," *IEEE Transactions on Pattern Analysis and Machine Intelligence*, vol. 25, no. 12, 2003.

[29] B. Abidi, S. Huq, and M. Abidi, "Fusion of visual, thermal, and range as a solution to illumination and pose restrictions in face recognition." *IEEE Carnahan Conf. Security Technology*, pp. 325–330, October 2004.

[30] R. Rowe, K. Nixon, and S. Corcoran, "Multispectral fingerprint biometrics," *Proceedings of the IEEE Workshop on Information Assurance and Security*, 2005.

[31] M. S. Ennis, R. K. Rowe, S. P. Corcoran, and K. A. Nixon, "Multispectral sensing for highperformance fingerprint biometric imaging," White papper. [Online]. Available: http://phoenix.inf.upol.cz/iris/

[32] R. K. Rowe and K. A. Nixon, "Fingerprint enhancement using a multispectral sensor," in *Proceedings of SPIE Biometric Technology for Human Identification II*, March 2005, pp. 81–93.

[33] T. Sakamoto, C. Nakanishi, and T. Hase, "Software pixel interpolation for digital still cameras suitable for a 32-bit mcu." *IEEE Transactions on Consumer Electronics*, vol. 44, no. 4, pp. 1342–1352, Nov. 1998.

[34] A. A. Efros and T. K. Leung, "Texture synthesis by non-parametric sampling," *IEEE International Conference on Computer Vision*, September 1999.

[35] A. Criminisi, P. Perez, and K. Toyama, "Region filling and object removal by exemplar-based image inpainting," *IEEE Transactions on Image Processing*, vol. 13, no. 9, pp. 1200–1212, September 2004.

[36] R. Chellappa and R. Kashyap, "Texture synthesis using 2-d noncausal autoregressive models," *IEEE Transactions on acoustics, speech, and signal porcessing*, vol. 33.

[37] W. T. Freeman, "Image quiliting for texture synthesis," in *Proceedings of SIGGRAPH, In Computer Graphics*, 2001.

[38] S. E. Rafael Gonzalez, Richard Woods, *Digital Image Processing.* Upper Saddle River, New Jersey: Pearson Prentice Hall, 2004.

[39] L.-G. Alberto, *Probability and Random Processes for Electrical Engineering.* Reading, Massachusetts: Addison-Wesely Publishing Company, Inc, 1994.

[40] C.-I. Chang, *Hyperspectral Imaging: Techniques for Spectral Detection and Classification.* New York, N.Y.: Kluwer Academic, Plenum Publishers, 2003.

[41] S. Shah, "Novel techniques for iris segmentation and synthesis," MSE Dissertation, West Virginia University, 2006.

[42] C. Boyce, A. Ross, M. Monaco, L. Hornak, and X. Li, "Multispectral iris analysis: A preliminary study," in *Proceedings of IEEE Computer Society Workshop on Biometrics*, June 2006.

[43] A. Ross, K. Nandakumar, and A. Jain, *Handbook of Multibiometrics (International Series on Biometrics).* Secaucus, NJ, USA: Springer-Verlag New York, Inc., 2006.

[44] P. R. S. Bolle, Connel, *Guide to Biometrics.* Spring St., New York: Springer Science, Buisness Media, 2003.

[45] J. Daugman, "Iris recognition and anit-spoofing countermeasures," 7th International Biometrics Conference, 2004.

[46] S. Parthasaradhi, R. Derkshani, L. Hornak, and S. Schuckers, "Time-series detection of persperation as a liveness test in fingerprint devices," *IEEE Transactions on Systems, Man, and Cybernetics*, vol. 35, pp. 335–341, August 2005.

[47] L. Thalheim, J. Krissler, and P.-M. Ziegler, "Body test: Biometric access devices and programs put to test," Ct́ Magazine, 2002.

[48] W. Tillman, *An Eye for An Eye.* USA, 1987.